Fabiana Cairone

Models and Systems for the control of two-phase processes in microfluidics

Doctor of Philosophy in Ingegneria dei Sistemi, Energetica, Informatica e delle Telecomunicazioni

UNIVERSITÀ DEGLI STUDI DI CATANIA

October 2018

UNIVERSITÀ
degli STUDI
di CATANIA

Dipartimento di Ingegneria Elettrica Elettronica e Informatica

---

Doctor of Philosophy in Ingegneria dei Sistemi, Energetica, Informatica e delle Telecomunicazioni

Models and Systems for the control of two-phase processes in microfluidics

Candidato:
Fabiana Cairone

Relatore:
Chiar.ma Prof. Ing. Maide Bucolo

October 2018

Contents

Abstract

The strong point of the microfluidics is the ability to miniaturize and integrate one or several laboratory functions on the same device, to have a portable and user-friendly instrument. Most applications require accurate measures and control within the microfluidic channels. In this thesis, the optical techniques were adopted to monitor, sensing and control the processes, leading to the research area of optofluidics that are based on the integration of fluidics and optics. To reduce the cost to develop these devices, the 3D Printing technology based on the Poly(dimethyl-siloxane) (PDMS) is proposed. All these aspects were addressed considering the two-phase flow (named slug) generated by the interaction of two immiscible fluids, a very common condition in bio-chemical applications. The methodological aspects were discussed in the first part of the thesis, starting from the extraction of parameters for the flow characterization, to their use for the flows real-time modelling and control schemes development; the second part investigates aspects faced for the realization of micro-optical flow detector by using the 3D Printing technology.

Introduction

Microfluidics is a novel and promising scientific field research whose progresses are aimed to the development of the Lab-On-Chip (LOC) systems. The strong point is the ability to miniaturize and integrate one or several laboratory functions on the same device, which thus becomes a portable and user-friendly instrument. The progresses made in the recent years have led to the realization and diversification of devices for chemical and biological analysis and biomedical applications [1, 2]. The advantage that could arise from the introduction on the market of disposable low cost diagnosis tools, as the Point-of-care (PoC) devices, can be evinced by their demanding and increasing request in medical and pharmaceutical sectors [3–5].

At the moment, the results presented in literature are strictly related to specific experimental conditions, so far from a well-established framework that can drive to the flow control [6]. Recently, some case studies have been presented in literature using a System-on-a-Chip (SoC) approach that embeds model predictive control strategies [7–9]. The SoC offers an high control level and modularity but its functionalities are strongly dependent from the integrated control logic and the knowledge of process model [10]. The need of a process model represents an important bottleneck for a widespread diffusion of its use in PoC applications.

Most of these applications require accurate measures and control within the microfluidic channels [11]. The optical techniques were adopted to monitor, sensing and control the processes [1, 12], leading to the research area of the optofluidics that are based on the integration of optics and fluidics [13].

The traditional methods to investigate the flows are based on the acquisition by using a fast CCD camera or a micro-PIV system [14]. Both instrumentation are noninvasive and allow to have detailed and accurate information about the mi-

crofluidic process, but with the drawbacks related to the cost [15].
To reduce the cost to develop the device and, at the same time, to have the optics and fluidics parts integrate in the same device, the 3D printing technology based on the Poly(dimethyl-siloxane) (PDMS) is proposed.
All these aspects have been addressed considering a two-phase flow (named slug flow) generated by the interaction of two immiscible fluids in a micro-channel, a very common condition in many bio-chemical applications. This thesis consists in two parts:

- Part I is divided in four chapters and deals with the methodologically aspects in the real-time modelling and the control of the slug flows;
- The Part II is divided in two chapters and presents the aspects faced for the realization of a micro-optical flow detector by using the 3D printing technology, as proposed low cost solution.

Part I

SLUG FLOWS IN MICROFLUIDICS

Introduction

The two-phase flow identification and control is one of the main open issue in the construction of highly complex microsystems, where fluids can circulate in a controlled manner performing a large number of tasks in a maze of micro-channels. Moreover, it is important that it can be easily adaptable in different operative conditions and able to guarantee the process reproducibility and reliability [16].
Interfaces between the two fluids adopt elaborate forms, and the classification of regimes (identified as bubble, slug or plug, annular, churn and wispy annular) can sometimes lead to inextricable phase diagrams, where many regimes are mixed up [17].
The two-phase slug flow considered was generated by the mixing of two upstreams (gas - liquid). When at the same time two streams of fluid are co-injected in a curved micro-channel, stretching and folding of segmented fluid are possible. These nonlinear features recognized in two-phase flows are highlighted in the phenomena named as chaotic advection that was introduced as responsible for the fast mixing time of multiple reagents inside isolated plugs (slugs) in winding micro-channels [18–20]. The combined effect of the curved geometry and the channel width in the range [100 $\mu m - 1$ mm], referred as meso-scale in Ribatski et al. [21], leads from one side to the increase of the process complexity and the difficult on the processes control, and to the other side in the speeding up the flow and mixing up the different phases.
In the chapter one the research of a trade-off between these conditions drove the systematic experimental study on the slug flow patterns generation, in terms of length and frequency of the slugs, in a straight and serpentine micro-channels. The attention was focused on three issues: how the curves in the geometry affect the slug flow displacement, the role played by the input flow rates in the slug flow

characterization and how the flow changes in different channel positions.
Three methods are widely used in channel with width in the order of cm for the characterization of length and frequency of the bubbles: the slugs frequency prediction methods with correlation [22], mechanistic model [23] and the probabilistic approach [24]. The measures necessary for the application of these methods require detection systems that can be considered invasive and complex for micro-channels and reducing the possibility of their use in this context.
Starting from the first works of Triplett et al. [25,26], a wide literature is available dealing with the two-phase processes in micro-channels with width in the range $[1-6]$ mm, as it can be evidenced in the review of Serizawa et al. [6]. Despite of that the biphasic flows in microsystem with a channel width less than 1 mm is still not well documented. The studies presented in literature mainly focus on two-phase flow characterization for specific application as the design heat exchanger [21], the microevaporator [27] and the micro-reactor [28], but far from a well-established framework that could drive to the flow identification and control in a general condition. In the major examples presented in literature the study of segmented flows through signal analysis is performed by the pressure transduction: flow regime [29,30], pressure or velocity fluctuations [31–33], residence time distribution and slug displacement [34]. In comparison to that, the optic transduction [35] does not interfere with the process and offers significant advantages considering the small channel width: an easy adaptation for the simultaneous acquisition in different test positions [36] and the easy integration of optical sensors with the microfluidic chips [37,38].
The most common way to optically monitor the process and collect information for the flow regime classification is by a continuous 2-D monitoring using fast CCD camera or μPIV system [14]. In both case, it is possible to obtain a detailed and precise information but with the drawbacks related to a costly and bulky equipment. The monitoring setups proposed in the development of this work were simplified to reduce the cost of the equipment to be used and make easier the optical components miniaturization. The optical information was post-processed for the flow classification and characterization both in time and in frequency domains. In chapters two and three, the experimental results presented in chapter one for the flows characterization have been used for the development of data-driven mod-

els suitable for real-time tracking of the flow. From a theoretical point of view, the computational modelling of fluidic processes is based on the Navier-Stokes equation (NS). If the Reynolds number (Re) is smaller than one, it is possible a model simplification assuming the linearization of the process based on the hypothesis that the slugs have a constant velocity and no dynamical interaction among each others. On the other hand, having more interacting fluids and $Re > 10$, no simplification is possible and the mathematical computational efforts increase.
Generally, the models of multi-phase microfluidics systems are obtained by Computational Fluid Dynamics (CFD) [39]. Even so, the complexity of CFD, due to the high computation level and the not accessible analytical solution, can not make them suitable for on-chip applications.
To have useful information about the investigated processes and to predict the model that represents the process itself, the data-driven approach can be applied. These techniques use a collection of data to identify complex systems, which cannot be easily understood, analyzed and modelled [40]. The approach proposed is based on data-driven models for the identification of microfluidic processes easy adaptable for an on-line process control.
In particular, two methods are proposed: the first is based on nonlinear systems synchronization theory [41] and the second method is based on the class of Non-Linear Autoregressive with eXogen input (NARX) models [42] implemented by both the neural networks (NN) [43] and the wavelet networks (WN) [44] nonlinear mapping.
An example of unidirectional synchronization used for the time series identification is in Fortuna et al. [45] in which the experimental time series is assumed as a generic state variable of an unknown system and this information used to drive a second system with a known model and undefined parameters. On this purpose as known system was considered the Chua's oscillator [46] due to dynamics diversification at the parameters change and, an iterative procedure based on Genetic Algorithm (GA) was used [47] to achieve the synchronization of the two systems by the parameters tuning. The models led to the successful identification of the slugs tracking and to quantify the slug's velocity being correlated with the mean of the slug inter-distance.
Finally, the chapter four copies with the problem of the real-time control of the

slug flow. Based on the control system theory definition, the microfluidic two-phase processes can be considered in the class of the two inputs and single output nonlinear dynamical systems [15, 48]. The control action on the microfluidic process can be obtained passively or actively. A passive control can be implemented to generate a specific flow pattern, exploiting the geometrical properties of the micro-channel and the physical properties of the fluids involved in the process, such as the hydrophobicity or the surface tension between the fluids and the walls of the channels. This approach does not require additional energy sources and does not increase the complexity and the cost of the external equipment. On the other hand, the active control allows to have a desired flow pattern manipulating, in a precise and quick way, small amounts of fluids flowing in the micro-channel. Examples of active control are based on mechanical pumping [49, 50], pneumatic pressure [51] or magnetic field [52]. The active control is more robust than the passive and provides a high level of flexibility in the control of droplet size and frequency. Both the passive and active techniques often are developed based on a specific process issue and embedded on-chip, so they are not easily extended in a different context and needs. The proposed solution overcomes these drawbacks, it is on the class of active control but, instead of using an electro-mechanical control system takes the advantage of the optical monitoring and the on-line signal processing to develop a general purpose data-driven approach to control the droplet flow in the micro-channel. Starting from the optical process monitoring and the analysis procedure for the flow characterization, a control parameter was identified and the open loop and closed loop control system implemented.

Chapter 1

Slug flows in micro-channels

1.1 Theoretical background

Two-phase flows are distributed into several distinct flow patterns depending on the liquid and gas flow rates and fluid and channel properties. Five main flow regimes were observed in the partially wetting square micro-channels: bubbly, wedging, slug, annular and dry flows. Specifically, in the slug flows on which we focus the attention, the bubbles have approximately the same diameter of the tube and their size is far longer than the channel height. The length of the bubbles can vary considerably. The nose of the bubble has a characteristic hemispherical cap and the gas in the bubbles is separated from the tube wall by a thin film of liquid. The liquid flow is contained mostly in the liquid slugs which separate successive gas bubbles [53].

In general, the two-phase processes are modelled by a nonlinear system of partial differential equations combining: the Navier-Stokes (NS) equation, describing the transport of momentum, the continuity equation and an inter facial tracking method [54].

The system of equations governing the process of two incompressible and immiscible phases in terms of the velocity (v) follows:

$$\nabla \cdot v = 0 \tag{1.1}$$

$$\rho(\frac{\partial v}{\partial t} + v \cdot \nabla v) = -\nabla P + \rho g + \nabla \mu(\nabla v + (\nabla v)^T) + G\nabla\phi \tag{1.2}$$

$$\frac{\partial \phi}{\partial t} + v \cdot \nabla \phi = \chi \varepsilon^2 \nabla^2 G \tag{1.3}$$

$$G = \frac{3\varepsilon\sigma}{2\sqrt{2}}(-\nabla^2\phi + \frac{\phi(\phi^2 - 1)}{\varepsilon^2}) \tag{1.4}$$

The reported system consists of the continuity equation (eq. 1.1), the NS equation (eq. 1.2) and the Cahn-Hilliard equation (eq. 1.3) to model the interface dynamics by the phase field variable (ϕ). The chemical potential G expresses the rate of change of free energy (eq. 1.4). The forces on the right-hand side of NS equation are due to the pressure tensor (∇P), the gravity (g) and the surface tension ($G\nabla\phi$). ε is the capillary width controlling the thickness of the diffusive interface, χ is the mobility tuning parameter, and σ is the surface tension coefficient between the two phases.

The fluid interface corresponds to the region where the phase field variable ϕ is in the range $]-1, +1[$ and takes the values of ± 1 in the two bulk phases ($\phi = -1$ for the carrier fluid and $\phi = 1$ for the dispersed phase). The density (ρ) and viscosity (μ) depend on the phase field as in the following equations:

$$\rho = \frac{1-\phi}{2}\rho_1 + \frac{1+\phi}{2}\rho_2 \tag{1.5}$$

$$\mu = \frac{1-\phi}{2}\mu_1 + \frac{1+\phi}{2}\mu_2 \tag{1.6}$$

In the multi-phase flow the evolution of the phase field variable governed by the Cahn-Hilliard equation involves a 4th-order derivative with respect to ϕ, this makes its treatment more complex than the NS equation in the single phase flow which involve only 2nd-order derivatives.

Considering the role of the input flows in the droplet formation and the flow patterns regime, four dimensionless numbers, reported in equations 1.7-1.10, have been widely investigated in microfluidics [55]: the Reynolds number (Re), the Capillary number (Ca), the Dean number (De) and the Air Fraction (AF).

$$Re = \frac{<\rho><v>D}{<\mu>} \tag{1.7}$$

$$Ca = \frac{<\mu><v>}{\sigma} \tag{1.8}$$

$$De = Re\sqrt{\frac{D}{2R_c}} \tag{1.9}$$

$$AF = \frac{V_{air}}{V_{air} + V_{water}} \tag{1.10}$$

Dealing with two-phase flow, the $< v >$, $< \mu >$ and $< \rho >$ are, respectively, the average velocity related to the two input flow rates and the mean of the fluid densities and viscosities. D is the characteristic dimension of the channel, R_c is the radius of curvature of the path channel and σ is the surface tension coefficient between the two phases. The V_{air} and V_{water} are the volumetric input flow rates of the two fluids.

The Reynolds number (Re), expressed by the ratio between the inertial and the viscous terms in the NS equation, is an indicator of flow nonlinearity. At the transition between laminar and turbulent flow it is of the order 10^3, while for $Re \ll 1$ the flow is dominated by the viscous stress, and the pressure gradient and the inertial effect are negligible. The Capillary Number (Ca) captures the relative importance of viscous force to surface tension. This is a key aspect in two-phase flows for the droplet formation, since they are largely dominated by the interfacial effects. A value of $Ca \ll 10^{-2}$ leads to the droplet formation.

1.2 Experimental setup

The global system used is schematized in Figure 1.1. It allows to generate the microfluidic process and to acquire the light intensity variations by means of a photodiode based circuit and a standard CCD camera, simultaneously. For the generation of microfluidic processes is extremely important the actuation system used to pump the flow and, the geometry and material of chip. These two choices determine a varity of process dynamics that can be generate.

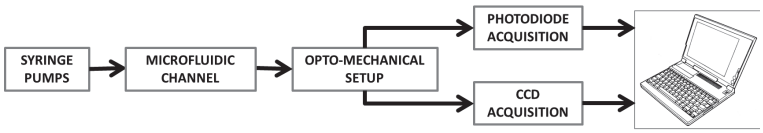

Fig. 1.1. Schematic of global platform setup.

Many applications in the field of flow chemistry, micro-reaction equipment and microfluidics depend on pulsation-free performance in the creation of fluid streams. This is because small flow rates in the nanoliter range require precision and smooth operation. The syringe pumps are widely used in microfluidic laboratories and they are based on a mechanical system actuated by an electric motor that push the syringe at the selected rate. In this way it is possible to rely on highly accurate mechanical components, enabling continuous processes, improving product quality, production flexibility and cost-effectiveness. In the experimental setup, two syringe pumps (Cetoni, NeMESYS) are used to inject fluids in the microfluidic chip through appropriate tubes. Thanks to the neMESYS UserInterface software, users can control these devices in order to change the flow rates. The microfluidic chip (SMS0104, ThinXXS) selected to performing the experiments, is made in COC (Cyclo-Olefin Copolymer) which combines good optical properties with biocompatibility and good chemical resistance to most acids and bases. It offers different geometries and dimensions, as it is possible to see in Figure 1.2 and in Table 1.1. Each micro-channel in the chip presents a squared section.
The opto-mechanical setup (Thorlabs OTKB) provides two different ways to acquire information about the microfluidic process: photodiodes and CCD camera. Photodiode is a semiconductor device that converts light into current. They are made by a part to sense the luminous intensity. To acquire and analyze these signals, capture card is directly interfaced to the PC via acquisition board (PCI 6024-E, National Instrument).

Tab. 1.1. Dimensions of the microchannels

Channel	**Length(mm)**	**Width/Depth(μm)**	**Internal Vol.(μl)**
1	21	100	0.2
2	121	640	49.6
3	66	320	6.8
4	50	320	5.1
5	16	320	1.6

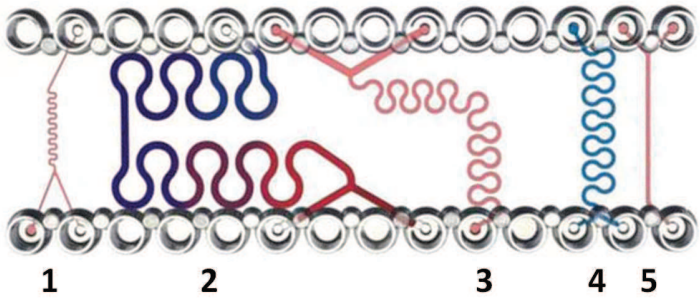

Fig. 1.2. Microfluidic chip with different geometries and dimensions.

The user interface of the card is BNC 2110 with I/O analogic and digital and its maximum sampling rate is 200kS/s. The CCD image detector (DCU224, Thorlabs) allows capturing the image from light beams and to reproduce it on the computer screen through a dedicated software.
Three functional modules constitute the global platform setup:

- A light source focusing module composed by the white light source, the dichroic mirror and the condenser lens;
- A detection and actuation optic module constituted by the objective lens and the mirror;
- A sample stage and holder module made up by a sample stage which provides 3-axis (X, Y and Z) translation of the microfluidic chip.

In the first module, the light source is focused and applied at the sample (for example the microfluidic chip). The emitted light is split through a dichroic mirror (FM01, Thorlabs) that reflects 980 nm laser beam (trapping source) in one side

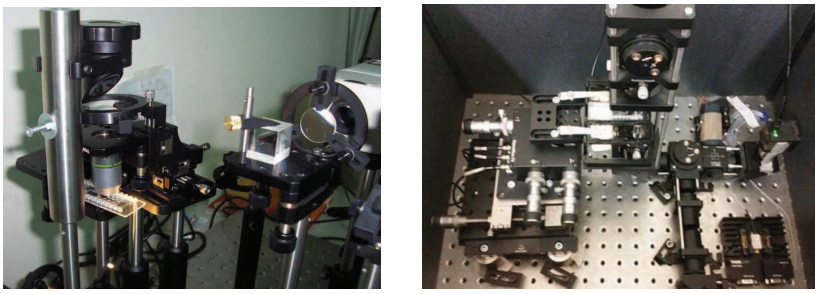

(a) (b)

Fig. 1.3. Pictures of the optical (a) $setup-1$ used in the experimental $set-1/3$; (b) $setup-2$ used in the experimental $set-2$.

in the vertical axis and in the other side toward a black plastic end cap. Then it arrives at the condenser lens that condensates toward the objective lens in order to illuminate the sample in case of detection, while it is used to collimate the beam after the optical trap in case of actuation.

Detection and actuation optic module contains an objective lens and XY translating lens mount (HPT1, Thorlabs), that allows to move the objective towards the sample, in such a way the working distances were respected.

The chip management module consists of a microscope slide holder mounted to a 3-axis (X, Y, and Z) translation stage (MAX301, Thorlabs) that is mounted on a 1-axis long travel translation stage (LNR50D, Thorlabs) and to a translating breadboard (TBB0606, Thorlabs).

Two optical setups were realized, labelled as $setup-1$ and $setup-2$. Both allow a simultaneous acquisition of light intensity variations, by means of a photodiode based circuit and a standard CCD (used with frame rate of 15 FPS). The $setup-2$ is an evolution of the $setup-1$. In Figure 1.3 (a) and (b) two pictures show, respectively, the optical $setup-1$ and the $setup-2$. The equipment used in the two setups are detailed as follows: the halogen lamp (KL1500LCD, Olympus) used to backlit the process was substituted by an emitter Ultra Bright White LED (LEDWE-10, Thorlabs); the objective with $20X$ magnification was replaced with one of $10X$; the pair of photodiodes (SLD-70BG2, Silonex) was changed with (SM05PD7A, Thorlabs) and the data acquisition board in $setup-1$ was PCI-6024E (National Instrument, used with a sample rate of 1 kHz) and in $setup-2$ was PCI 6024-E (National Instrument, used with a sample rate of 4 kHz). The CCD active

area is 17 mm^2 while each photodiode active area is equal to 1 mm^2 in the $setup-1$ and 6 mm^2 in the $setup-2$. The signals used for the flow investigation are those acquired from the photodiode, giving an average information in their active area. A detailed description of the opto-mechanical system realized in the $setup-1$ is in Bucolo et al. [56], while for the $setup-2$ a modified version of the design presented in Appleyard et al. [57] was considered to have the contemporary signals and images acquisition. The signals were affected by frequency noise components related to the power supply and the illumination. A filtering procedure, that preserves the process dynamics, was implemented using a Butterworth low pass filter ($f_{cut} = 100\ Hz$ and order $N = 5$), and two notch filters respectively at the frequencies $f_{cut} = \{50; 100\} Hz$ with a quality factor $Q = 3$.

1.3 Experimental campaigns

The continuous slug flows were generated by pumping de-ionized water and air at the Y-junction of micro-channels. Three experimental sets were considered, named $\{set-1,\ set-2,\ set-3\}$. The two syringe pumps were connected to the channel inlets and constant flow rates were imposed. The three geometries considered are shown, in details, in Figure 1.4: a straight channel with width $w = 320\ \mu m$ and length $l = 16\ mm$ (labelled as $G1$), a serpentine with width $w = 320\ \mu m$ and length $l = 50\ mm$ (labelled as $G2$) and, a second serpentine with width $w = 640\ \mu m$ and length $l = 121\ mm$ (labelled as $G3$). The curvature radius is, for the serpentine geometries, 1.28 mm. Introducing for $\{G2;\ G3\}$ two analogous straight channels $\{G20,\ G30\}$ with the same width and height, it was possible to deduce the hydraulic resistances $\{Rh1;\ Rh2,\ Rh3\}$ [55]. The $Rh2$ is the greatest, three times bigger than that of $Rh1$ and two times bigger than that of $Rh3$.

In the experimental $set-1$, to evaluate the effect in the slug displacement induced by the curves, the process was monitored in an position located at a distance from the Y-junction of about $4mm$ in $G1$ (see Figure 1.4(a)) and, after 9 bends in $G2$ (see Figure 1.4(b)). In the experimental $set-2$, the process was monitored in a position located at a distance of about 60 mm from the Y-junction, at the center of the straight part, tagged as point B in $G3$, to investigate on the flow pattern

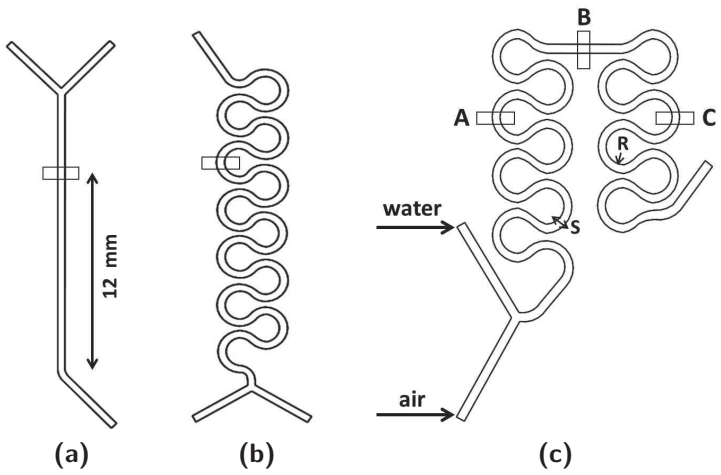

Fig. 1.4. The micro-channel geometries considered. (a) The straight channel ($G1$); (b) The serpentine ($G2$) with width $w = 320\ \mu m$ and length $l = 50\ mm$; (c) The serpentine ($G3$) with $w = 640\ \mu m$ and length $l = 121\ mm$.

after the slugs have experienced the mixing meander (see Figure 1.4(c)).
Additionally, in the experimental $set - 3$ the behaviour in the three positions in $G3$ tagged as {A, B, C} was considered to highlight the changes in the slug flow in relation to the closeness to the chip inlets and outlet (see Figure 1.4(c)).
The $setup - 2$ was used for the acquisition in the experimental $sets - 1/3$ and the $setup - 1$ for the experimental $set - 2$. Different apparatus were necessary for an optimization of setup performance considering smaller channels, as in experimental $set - 1$ and longer recording as in the experimental $sets - 1/3$.
The experimental $set - 1$ consists of 6 experiments. The attention was focused on the effects on the slug displacement due to the winding geometry. The two micro-channel geometries $\{G1;\ G2\}$ were considered, and the two inputs flow rates were set equal ($f = V_{air} = V_{water}$) varying in a set $\{0.1,\ 0.3,\ 0.5\}\ ml/min$. Those values are lower respect to the one in the other experimental sets being the channel width smaller. This experimental set is marked in the input flow rates space reconstruction of Figure 1.5 with circles. The flow information was recorded in the area shown in Figure 1.4 (a) and (b) and each experiment recording lastes 240 s.
In the experimental $set - 2$, the micro-channel considered was $G3$ and a total of four experimental campaigns were designed. By these campaigns the role played

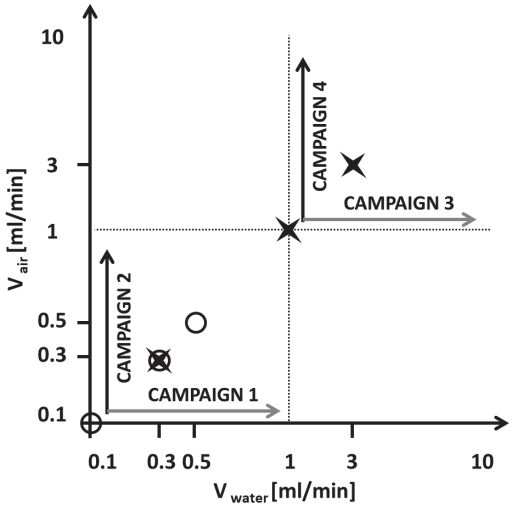

Fig. 1.5. The reconstruction of the input flow rates space (V_{air}, V_{water}).

by the two inputs flow rates in the slug pattern generation in a serpentine microchannel was investigated. Each campaign consists of 12 experiments in which one flow rate ($V_{air},\ V_{water}$) was fixed and respectively the others was varied. In the $campaigns - 1/2$ the input flow rates were maintained below 1 ml/min ($f \leq 1\ ml/min$), while they were one order of magnitude bigger ($f \geq 1\ ml/min$) in the $campaigns - 3/4$. The input flow rates space reconstruction is represented in Figure 1.5. In Table 1.2, the flow rate per campaign and the relative Air Fraction (AF) are reported, and in Table 1.3 the ranges of the most significant dimensionless parameters in the process under investigation, as the Reynolds number (Re), the Capillary number (Ca) and the Dean number (De).

The Reynolds number values underline an increase of complexity in the flow for varying the input flow rates and, dealing with multiphase flows, it was computed using the average of the densities and input flow rates of the two fluids. For the $campaigns - 1/2$ we are in a low Re number regime, while for $campaigns - 3/4$ we are at the beginning of the inertial microfluidics regime [58]. The Capillary number values are in the range of $[10^{-4};\ 10^{-2}]$, so always below the order of 10^{-2} that confirms the theoretical expectancy of the droplet/slug formation. The Dean number expresses the relation between a secondary recirculation flow outside the slug due to the curves in the geometry taking into account the curvature radius [59]. The

Tab. 1.2. Air Fraction for the four experimental campaigns in $set-2$. The flow rates are in ml/min

AIR FRACTION (AF)			
CAMPAIGN-1 $V_{air}=0.12$ $V_{water}<1$	CAMPAIGN-3 $V_{air}=1.2$ $V_{water}>1$	CAMPAIGN-2 $V_{air}<1$ $V_{water}=0.16$	CAMPAIGN-4 $V_{air}>1$ $V_{water}=1.6$
0.158		0.433	
0.160		0.521	
0.162		0.614	
0.164		0.659	
0.167		0.733	
0.174		0.761	
0.182		0.776	
0.198		0.794	
0.233		0.817	
0.267		0.826	
0.347		0.837	
0.433		0.843	

Tab. 1.3. Range of most significant dimensionless numbers for the four experimental campaigns in $set-2$.

	Re	Ca (10^{-2})	De
CAMPAIGN-1	[0.93-2.54]	[0.015-0.042]	[0.65-1.8]
CAMPAIGN-2	[0.93-3.35]	[0.015-0.055]	[0.65-1.8]
CAMPAIGN-3	[9.26-25.4]	[0.153-0.419]	[6.55-17.96]
CAMPAIGN-4	[9.26-33.53]	[0.153-0.553]	[6.55-23.71]

values in Table 1.3 underline a stronger influence at the increase of the input flow rate.

A variable pace was used varying V_{water} and V_{air} based on flow visual inspection. In Table 1.2, the air fraction (AF) values associated to each experiment per campaign are reported and used for the results discussion. The air fraction values in $campaigns-1/3$ are equal, as those in $campaigns-2/4$, but it is important to notice that the input flow rates used in case of $campaigns-3/4$ are one order greater than in $campaigns-1/2$. Each experiment recording lasts 20 s; being the channel width greater and the process faster than in the experiment $set-1$, a shorter time recording was sufficient to capture the flow dynamics.

The experimental $set-3$ consists of 9 experiments and the microchannel considered was $G3$. The aim of this investigation was the analysis of the changes in the slug patterns at different microchannel positions (or as well areas): close to the inlet point-A, at the center point-B and close to the outlet point-C. For each position a total of three experiments were considered assuming the input flow rates equal

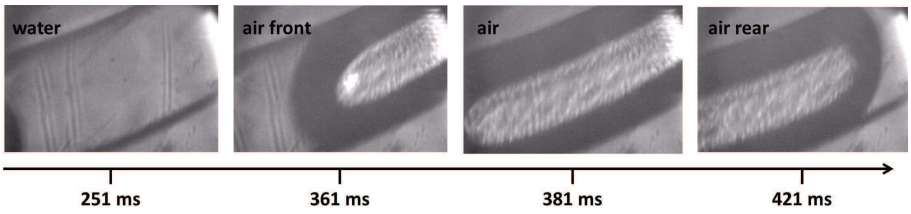

Fig. 1.6. A CCD video frame sequence during an air slug passage in the investigation area B of the micro-channel $G3$.

($f = V_{air} = V_{water}$) varying in the set $\{0.3,\ 1,\ 3\}\ ml/min$. The acquisition procedure consisted in three steps: the optical system was centred in one of those points, then the two reference optical signals (micro-channel filled with water and filled with air) were recorded and, finally, the acquisitions for the three established flow rates began. This experiment set is marked with stars in the input flow rates space reconstruction of Figure 1.5. Each experiment recording lasts 240 s, to capture slight variations and dynamical changes in the slug flow at the different positions.

The signals acquired by the photodiodes range on two or three levels. The top level reveals the water presence in the channel and, the lower value the air slug passage, while some lowest peaks are for the slugs fronts and rears. In Table 1.4 the means of air and water levels for each experimental set are reported. Looking at the frame sequence of a slug passage in a designed micro-channel's position (see Figure 1.6), it can be noticed that during the air slugs' passage the intensity of the light signal decreases suddenly due to the difference between the refraction index of COC ($n_{COC} = 1.5$) and air ($n_{air} = 1$), so the air slug contour becomes darker than the inside of the slug and the chip wall. This effect is less evident during the water passage being the water refraction index ($n_{water} = 1.3$) closer to the one

Tab. 1.4. Means of air and water levels for each experimental set.

	Air level (mV)	**Water level (mV)**
Esperimental set-1	-2	0.5
Experimental set-2	-5	10
Campaigns-1/2	-4	4
Campaigns-3/4		
Experimental set-3	-1	0.6

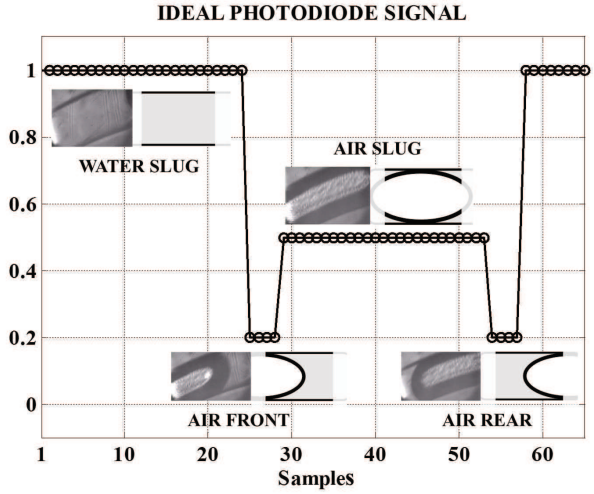

Fig. 1.7. The ideal trend of the optical signal correlated with the slug passage. Three levels of luminosity are distinguished. The top reveals the water presence, the middle one the air passage, and the two lowest peaks are for the slug front and rear.

of the COC. Thanks to this phenomenon, it is possible to distinguish clearly the slug passage in the optical signals acquired by photodiode after the preprocessing frequency filtering. In Figure 1.7 is shown the ideal trend of the optical signal and the related CCD video frames acquired during a slug passage in the investigation area of the micro-channel. In fast slug flows, based on the acquisition system set-up, it could possible to distinguish only the air and water levels.

1.4 Indicators for slug flows characterization

Based on the experimental setups used, two flow patterns can be clear distinguished by visual inspection of the signal dynamics, defined as slow and fast. In the slow dynamics, the length of both air and water intervals can have significant variations during the experiment and the flow can be characterized by a sequence of smaller water intervals compared to the air intervals or vice versa (see Figure 1.8(a) and (b)). In the fast dynamics, the length of air and water intervals are closer than in the previous case and during the time course, the significant changes cannot be detected in their lengths but in their inter-distances. It can be interpreted as a fast train of small air/water slugs of similar lengths (see Figure 1.8(c)

and (d)). The signals related to the slow patterns can be associated to a square wave trend and those related to the fast patterns to an oscillating behaviour. It can be verified that the transition point between the two dynamics is correlated to the input flow rates and the geometries. In case of experimental $sets - 1/3$ considering equal input flow rates, the fast dynamics were detected respectively at $f > 0.7\ ml/min$ for $\{G1;\ G2\}$ and at $f > 3\ ml/min$ for $G3$. It is worth to notice that, the hydraulic resistances of $G1$ and $G20$ are greater than that of $G30$, so it was expected a transition for smaller flow rate in the experimental $sets - 1/3$ than in the $set - 2$. In case of experimental $set - 2$, due to the different values of two inputs flow rates, the fast dynamics were detected for $\{V_{air}; V_{water}\}$ both greater than 1 ml/min.

Another important aspect is the possibility to trace out the information about the slugs length from the signals and the characteristics of the optical setup: the sample frequency, the size of the optical window and objective magnification. During the fast patterns, in the experimental $set - 2$, a slug passage lasts on an average of 5 samples that is equivalent to 5 ms (based on optical $setup - 1$ where the sample frequency 1 kHz, the photodiode area 1 mm^2 and objective magnification $20X$) whereas, in experimental $set - 3$, lasts on an average of 10 samples that is equivalent to 2.5 ms (based on optical $setup - 2$ where the sample frequency 4 kHz, the photodiode area 6 mm^2 and objective magnification $10X$).

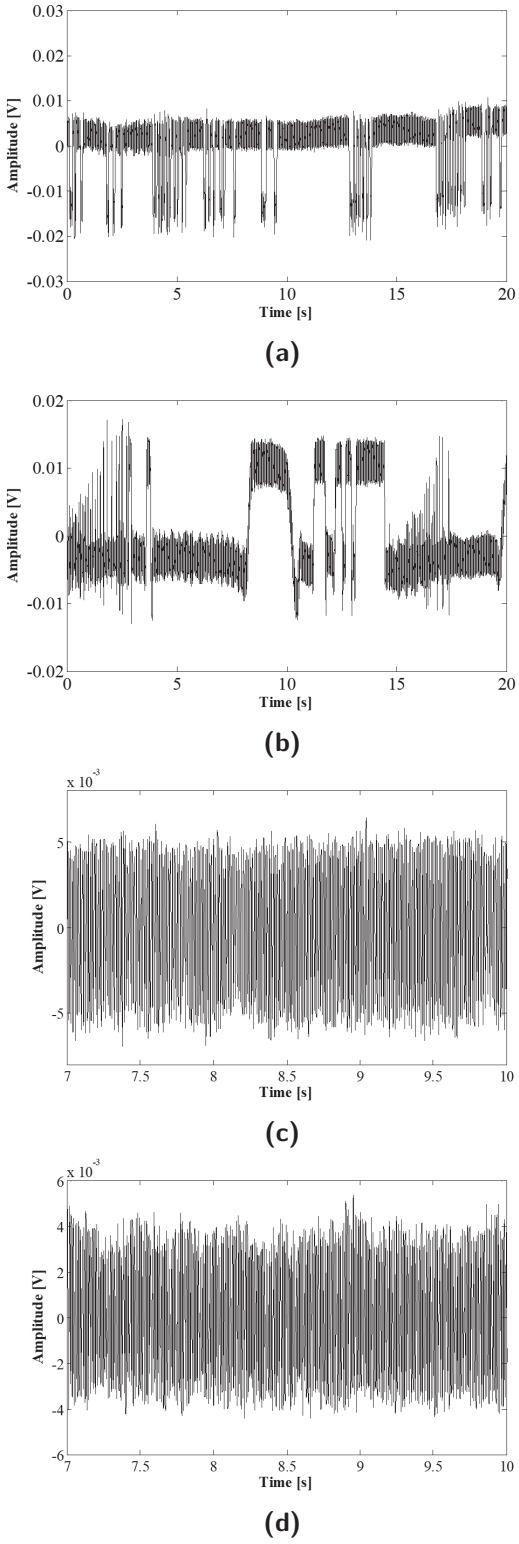

Fig. 1.8. Experimental $set-2$. Signals related to one experiment per campaign: (a) $campaign-1$ with $AF = 0.158$; (b) $campaign-2$ with $AF = 0.794$; (c) $campaign-3$ with $AF = 0.158$; (d) $campaign-4$ with $AF = 0.794$.

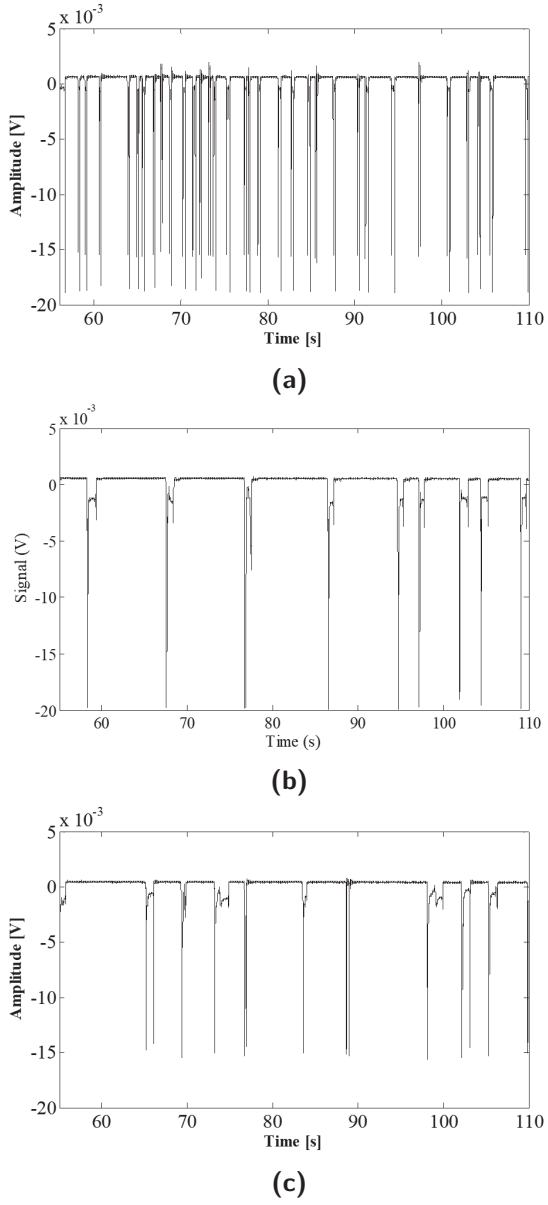

Fig. 1.9. Experimental $set-3$. Signals acquired with inputs flow rates $f = 0.3\ ml/min$ in the selected channel positions. (a) A close to the inlet; (b)B at the channel length center; (c) C close to the outlet.

For the experimental $set-2$, in $campaigns-1/2$ for input flow rates ranges $f \leq 1\ ml/min$, the slug patterns can be identified as slow dynamics. It is possible to evidence in the signal trend that for campaign-1 the dominant input flow is the water (see Figure 1.8(a)) and air for $campaign-2$ (see Figure 1.8(b)). Differently,

in $campaign-3/4$, for input flow rates $f \geq 1\ ml/min$, the fast dynamics are clearly distinguishable, and by visual inspection the dominant input flow cannot be detectable. In Figure 1.9 four experiments, one per campaign, were selected to sum up the signals features: $V_{water} = 0.64\ ml/min$, $V_{air} = 0.12\ ml/min$ ($campaign-1$, $AF = 0.158$); $V_{water} = 0.16\ ml/min$, $V_{air} = 0.60\ ml/min$ ($campaign-2$, $AF = 0.794$); $V_{water} = 6.4\ ml/min$, $V_{air} = 1.2\ ml/min$ ($campaign-3$, $AF = 0.158$); $V_{water} = 1.6\ ml/min$, $V_{air} = 6.0\ ml/min$ ($campaign-4$, $AF = 0.794$).
For both the experimental $sets-1/3$ only slow dynamics were considered, that allows to evince the signals changes also by visual inspection. In Figure 1.9, the signals acquired for input flow rate $f = 0.3\ ml/min$ in the three positions A, B, C are reported.
Four indicators were computed to classify flow patterns by the signals characteristics of the signal and to quantify the dynamics sensitivity to the experimental conditions. The indicator, named delta, was introduced for both slow and fast patterns, to quantify the air or water dominance in the micro-channel. Additionally, it was considered: for the slow patterns the slug passage in $[ms]$ (named length), for the fast patterns the slugs inter-distance mean and variation (named spectrum peak and spectrum area).
The delta was computed by statistical distribution of the acquired signals. It shows a bimodal shape in which the two peaks identify the presence of air (P1) and water (P2). Two examples of the bimodal distribution obtained for respectively slow and fast patterns are in Figure 1.10 (a) and (b). The delta was evaluated as the difference of two peaks amplitudes normalized in percentage, as in eq. 1.11. The positive values of delta are for the dominance of the water and negative for the air.

$$delta(\%) = \frac{(P_2 - P_1)}{max(P_1, P_2)} * 100 \tag{1.11}$$

For the slow patterns, where it is possible to distinguish longer interval of water or air, the changes in the length of air and water intervals were considered. A square wave model was correlated to the signal trend (see Figure 1.10(c)) and a procedure based an adaptive threshold was used for its reconstruction. By means of this square model, it was possible to derive the length (in $[ms]$) of each water/air

interval and the number of intervals. Combining these two information the plot of trend of water/air intervals mean length in an experiment can be reconstructed as shown in Figure 1.11. It can be noticed that, the length trace could present some irregular peaks due to the unexpected longer air/water intervals compared with the value assumed on the average. In the results these outliers were neglected. For the fast patterns, by assuming constant the length for air and water slugs, as it can be drawn from the oscillating trend, the mean inter-distance and variability were computed. The content in the frequency domain, that is not significant in slow flow, becomes relevant, and the signal spectrum was used for the inter-distance evaluation. The spectrum profile was approximated with a Gaussian model to characterize the maximum in the spectrum and the area under the Gaussian curve (see Figure 1.10(d)) associated respectively to the mean slug interdistance and its variability. An iterative procedure, that uses an unconstrained nonlinear optimization algorithm to decompose the overlapping-peak signal into its components, was considered for the fitting in O'Haver [60]. By this Gaussian model it was possible to extract: the peak position in the spectrum, its amplitudes as well as the area under the Gaussian curve. The latter was considered proportional to the spectrum bandwidth. From a theoretical perspective, smaller is the bandwidth closer is the flow dynamics to a periodic behaviour, so this parameter can be used as indicator of the process nonlinearity.

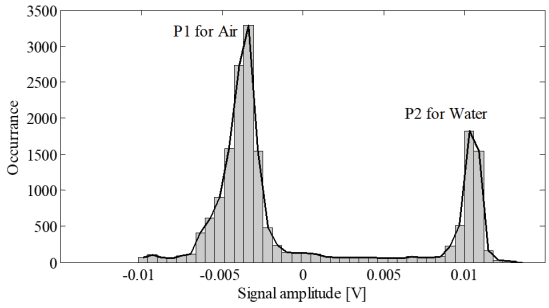

(a)

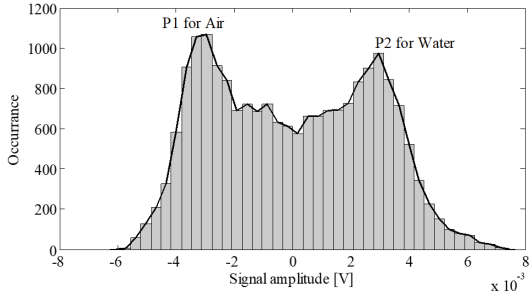

(b)

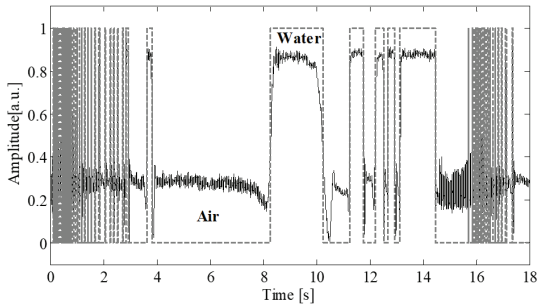

(c)

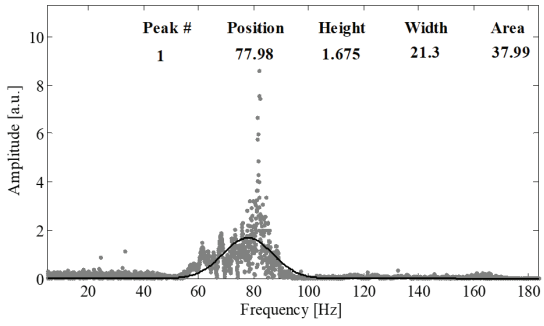

(d)

Fig. 1.10. Slug patterns characterization by signal analysis. For the delta computation, the bimodal distribution in case of (a) slow flows and (b) fast flows; (c) for the slow dynamics: fitting of the signal with a square wave model for the lengths of the air/ water intervals computation; (d) for the fast dynamics: fitting of the spectrum Gaussian profile and evaluation of the peak position, the amplitude, the area under the curve.

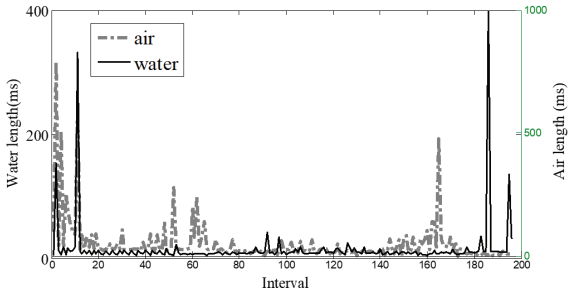

Fig. 1.11. Intervals length trace reconstruction by signal analysis for the experiment ($campaigns - 1/2$, $AF = 0.433$): the water is in black line and air in dotted gray line.

1.5 Slug flows dynamics

1.5.1 Varying the micro-channel geometry ($set - 1$)

Due to the experimental setting, for the input flow conditions $f = \{0.1, 0.3, 0.5\}$ ml/min the signals show a slow dynamics with long water intervals and smaller air slugs, as in experimental $set - 3$ (see Figure 1.9). The delta and the number of slugs intervals per minute per experiment were computed. In Figure 1.12(a) and Figure 1.13(a) the bar diagrams related to the delta values and the number of intervals at the different the input flow rate conditions are represented for both geometries $\{G1;\ G2\}$. In Figure 1.12(b) and Figure 1.13(b) the trends of these parameters obtained by the values interpolation versus the input flow conditions $f = \{0.1, 0.3, 0.5\}$ ml/min per $\{G1;\ G2\}$ are represented. In the Figure 1.12(b) and Figure 1.13(b), respectively, the delta decreases and the number of intervals increases following a linear trend in case of the straight channel and a parabolic trend in the serpentine. Being the hydraulic resistance of the straight channel ($Rh1$) three time greater than the one of the serpentine ($Rh2$) a faster change in both these parameters was expected. Nevertheless, it is possible to notice that distances between the parameters trends for $G1$ and $G2$ are not conservative respect to the ratio of 3 increasing nonlinearly with the input flow rates. That confirms the higher sensitivity to the input flow conditions in the straight channel compared with the curved one, so the robustness introduced into the processes by a winding geometry.

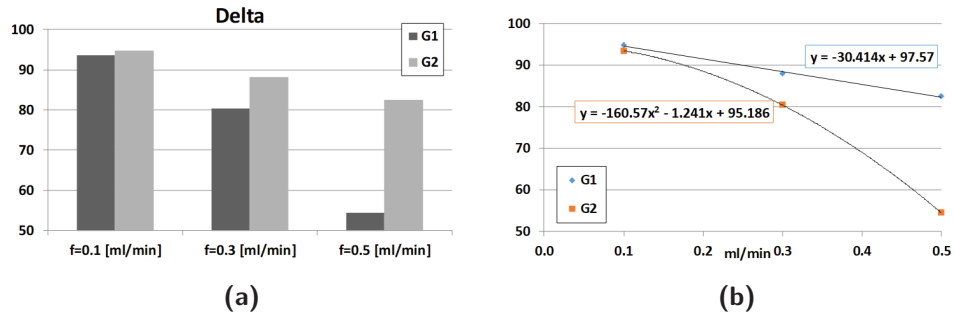

Fig. 1.12. Experimental $set-1$. (a) Delta bar diagram and (b) the trends obtained by values interpolation versus the input flow conditions $f=\{0.1,0.3,0.5\}\ ml/min$ per $\{G1;\ G2\}$.

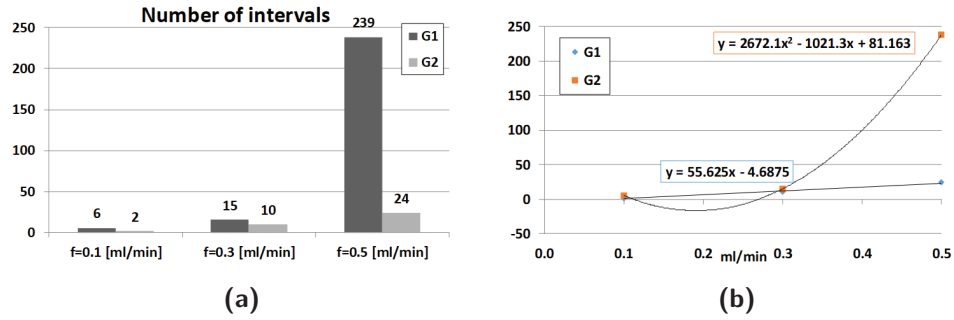

Fig. 1.13. Experimental $set-2$. (a) Number of intervals per minute bar diagram and (b) the trends obtained by values interpolation versus the input flow conditions $f=\{0.1,0.3,0.5\}\ ml/min$ per $\{G1;\ G2\}$.

1.5.2 Varying the input flow rate ($set-2$)

In $campaigns-1/2$ for input flow rates $f\leq 1\ ml/min$ the signals show slow dynamics and no bands of interest are detected in the spectra. Differently in $campaigns-3/4$ for input flow rates $f\geq 1\ ml/min$ the signals show fast dynamics and it is always possible to identify in the spectra a band of interest.

In Figure 1.14 the results obtained per experiment in the $campaigns-1/2$ are summarized. Figure 1.14(a) and (b) report the average length in $[ms]$ of the air (gray line) and water (black line) slugs versus the AF respectively in $campaign-1$ and $campaign-2$. In $campaign-1$, the air slugs are longer than those of water for

$AF > 0.19$, while in $campaign - 2$ in all the AF range. At the value $AF \cong 0.43$, present in both campaigns, the length of the air and water intervals are equal. For $0.19 < AF < 0.40$ and $0.46 < AF < 0.70$ respectively in $campaign - 1$ (see Figure 1.14(a)) and $campaign - 2$ (see Figure 1.14(b)) air and water intervals increase and decrease with a parabolic trend can be identified.
In $campaign - 1$, the air intervals are in the range $[50 - 500]$ ms and the water intervals in the range $[50 - 350]$ ms, both the mean length of the air and water intervals increase until $AF = 0.35$. In $campaign - 2$ the air intervals are in the range $[50 - 800]$ ms and the water intervals in the range $[50 - 350]$ ms, both the mean length of the air and water intervals increase until $AF = 0.521$. In $campaign - 1$ for $AF < 0.19$ a second smaller parabolic trend was detected in which the water interval are bigger than the water, but no correlation between the two trends is visible. Finally, in campaign for the $AF > 0.73$ a stable behaviour arises in which both intervals are almost unvaried: the mean length of the water slugs is around 50 ms and of the air slugs 150 ms.
In Figure 1.14(c) and (d) the bar diagrams related to the delta values versus the AF respectively in $campaign - 1$ and $campaign - 2$ are plotted. In $campaign - 1$, consistently with the previous results, a stronger water dominance up the 90% can be found for $AF < 0.19$, and then a slow decrease leads to the air dominance for $AF > 0.23$. This trend lasts until the AF = 0.43 with a delta around -95%. In $campaign - 2$ the delta is always negative, meaning air dominance. For $0.43 < AF < 0.733$ the subsequent delta increase and decrease reflects the sensitivity to the air and water slug length increase and decrease. The oscillating value for the $0.733 < AF < 0.817$ in the range $[-95\%; -50\%]$ can be correlated to a transitory behaviour before the stabilization. It is worth to notice that in both campaigns the trends of the air and water mean length are mainly specular respect to the AF value 0.433, irrespectively of which input flow rate is dominant.

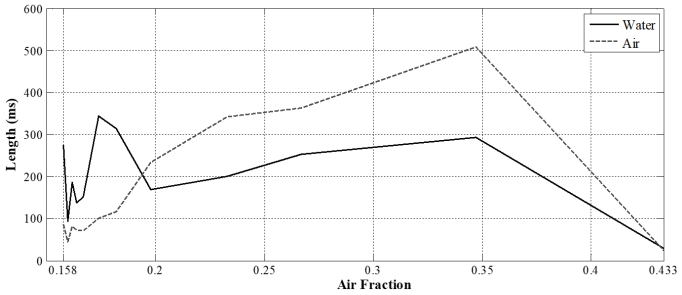

(a)

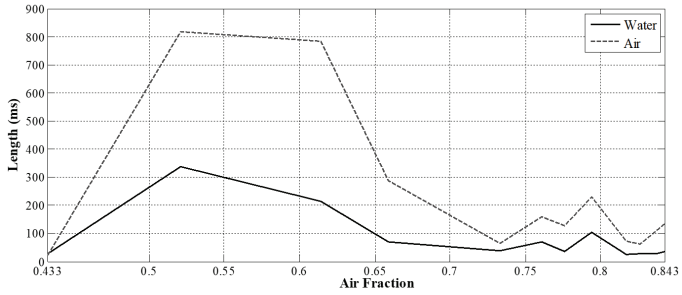

(b)

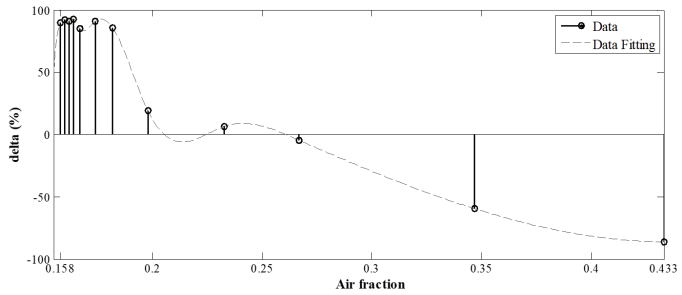

(c)

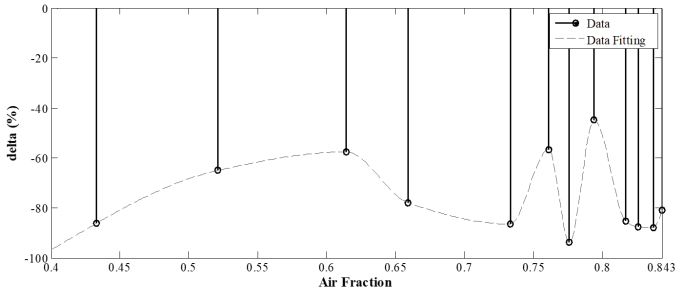

(d)

Fig. 1.14. Experimental $set-2$ with $f < 1\ ml/min$. The intervals average length of the air (dotted line) and water (black line) slug versus AF in the $campaign-1$ (a) and in the $campaign-2$ (b); The delta value versus AF in the $campaign-1$ (c) and in the $campaign-2$ (d).

The maximum mean length of the air in $campaign-2$ is 800 ms greater than the one in $campaign-1$ (300 ms), while the maximum mean of the water length is around 300 ms in both cases. It is important to underline that, considering an experiment with longer slugs, to have a significant number of slugs a longer time interval is necessary.

In $campaigns-3/4$, for the experimental campaigns with $f > 1$ ml/min, the Figure 1.15(a) and (b) report the position of the peak in the spectrum (black solid line) and the value of area under the Gaussian (gray dotted line) versus AF, respectively, for $campaigns-3/4$. The frequency peak trend decreases almost linearly in $campaing-3$ in $[30, 90]$ Hz and then increases in the same range in $campaign-4$. An opposite behaviour is shown for the Gaussian area: its lowest values is around 30 $[a.u.]$ in $campaign-3$ and 10 $[a.u.]$ in $campaign-4$. This translation of the peak position in the spectrum reflects the changes in the interdistance between slugs. The higher frequencies, so the smaller inter-distances, were for low value of AF in $campaign-1$ and high in $campaign-2$. For the same AF values the area under the Gaussian curve decreases leading to a reduction in the inter-distance variability. It means that, increasing the input flow rate it is possible to obtain dynamics in which the nonlinearity effects are reduced, toward a tendency to an oscillating periodic behaviour. In Figure 1.15(c) and (d), the bar diagrams related to the delta variation versus AF respectively for $campaign-3$ and $campaign-4$ are shown. In $campaign-3$ there is always water dominance, while in the $campaign-4$ the delta (Figure 1.15(d)) initially is positive (water dominance) then for $AF = 0.521$ becomes negative (air dominance). For $AF \leq 0.167$ in $campaign-3$, for $AF > 0.817$ in $campaign-4$ the delta values are smaller and oscillating respectively around 20% and -5%. The reduction of delta was obtained because the two peaks have close amplitude, and it is correlated with the same length of the air and water intervals. For$AF = 0.233$ in $campaign-3$ and $AF = 0.614$ in $campaign-4$ the maximum delta values are obtained around $\pm 40\%$. Both results confirm that the increase of input flow rate produces a effect on the slug displacement along the micro-channel leading to a stabilization of the process toward a periodic regime where the length of the air and water interval are closer.

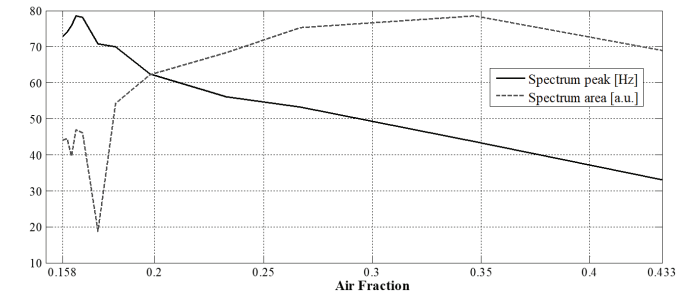

(a)

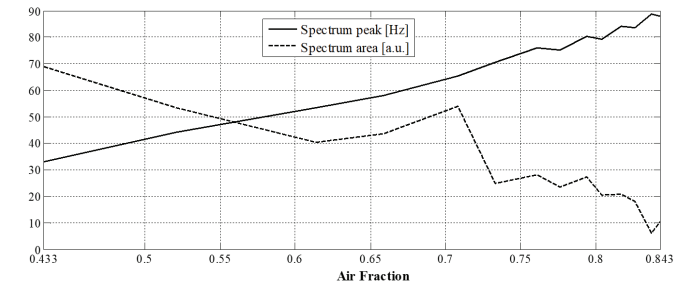

(b)

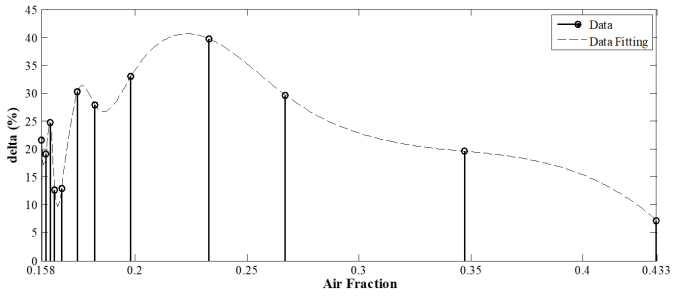

(c)

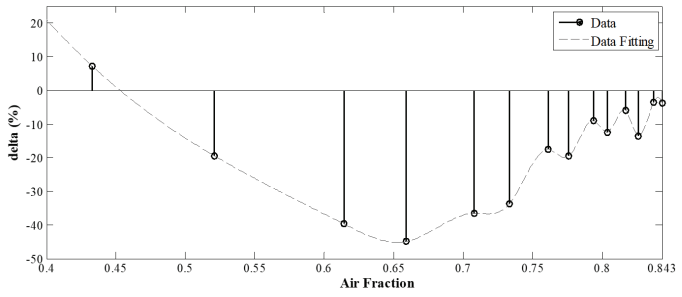

(d)

Fig. 1.15. Experimental $set-2$ with $f > 1\ ml/min$. The position of the peak in the spectrum (black line) and the area under the Gaussian (dotted line) versus AF in the $campaign-3$ (a) and in the $campaign-4$ (b); The delta value versus AF in in the $campaign-3$ (c) and in the $campaign-4$ (d).

1.5.3 Varying the investigation points ($set-3$)

Due to the experimental setting, for all the input flow conditions $f = \{0.3, 1, 3\}$ ml/min the signals show slow dynamics with long water intervals and small air slugs, this was important for the characterization of the behaviour at the different positions {A, B, C} of the micro-channel.
In Figure 1.16, the bar diagrams related to the delta value for the three flow rates and the three selected positions are shown. It is possible to notice that there is water dominance with a positive delta value in a range of [80%; 90%]. The delta at the points (A, B) is similar, while it changes at the point C, becoming slightly greater for $f = 0.3$ ml/min and smaller for $f = \{1, 3\}$ ml/min. The growth of delta in point C for $f = 0.3$ ml/min could due to a predominant effect of the curves inducing a slowdown of the process at the outlet. From the other hand, the delta reduction in point C for $f = \{1, 3\}$ ml/min can be related to output pressure increase for higher slug velocity. As a consequence of the air compression in the position C, the air slugs mean lengths are always less than in the other positions, this effect is amplified by the flow velocity. In Figure 1.17 and Figure 1.18 the mean length in $[ms]$ of respectively the air and water intervals are reported for the three positions. The Figure 1.17(a) and Figure 1.18(a) show the results for the three input flow rates $f = \{0.3, 1, 3\}$ ml/min, while the Figure 1.17(b) and Figure 1.18(b) report a zoom on for $f = \{1, 3\}$ ml/min.
That was necessary because the mean length for $f = 0.3$ ml/min is definitely greater than in the other two flow conditions, for example in point B for $f =$

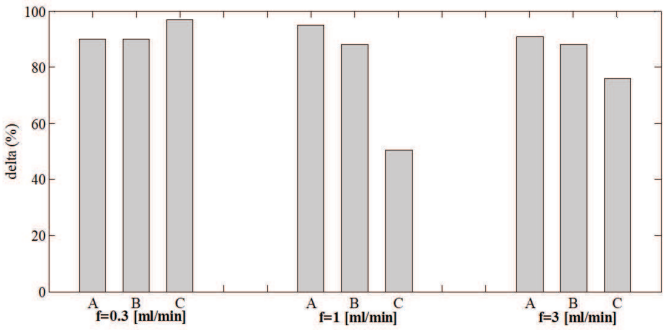

Fig. 1.16. Experimental $set-3$. Delta value for $f = \{0.3, 1, 3\}$ ml/min in the section tests $\{A, B, C\}$.

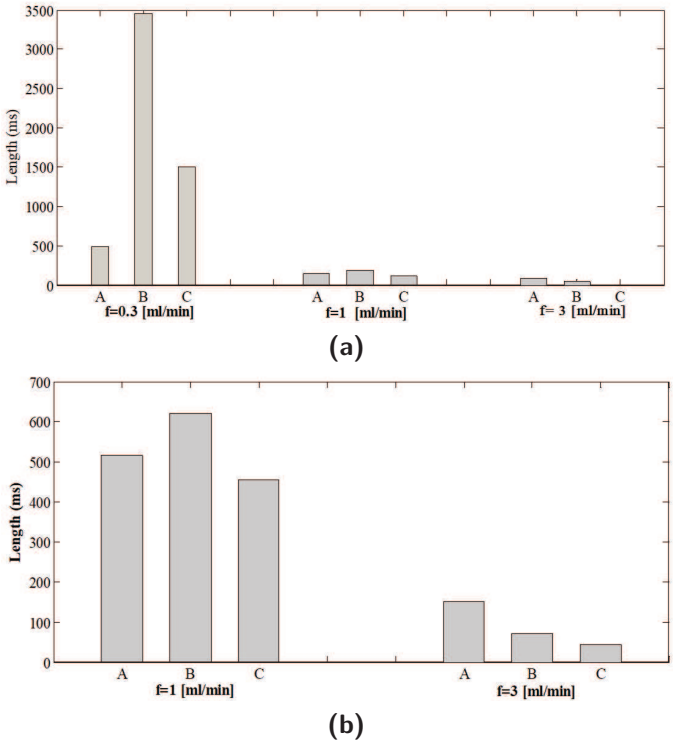

Fig. 1.17. Experimental $set-3$. The average length of the air intervals in the channel positions $\{A, B, C\}$ respectively close to the inlet, at the center and close to the outlet; (a) $f = \{0.3, 1, 3\}$ ml/min; (b) a zoom for $f = \{1, 3\}$ ml/min.

$\{0.3, 1, 3\}$ ml/min the water slug length is respectively $\{3.5; 0.6; 0.1\}$ s for the air and $\{20; 0.18; 0.06\}$ s for the water. It is possible to notice that both the mean air and the water intervals lengths are sensitive at the same way to the acquisition points and the input flow rates.

In addition, it is possible to detect how the dynamics at the inlet is affect by the increasing of the flow. In both the experiments with the $f = \{0.3; 1\}$ ml/min a Gaussian profile is detectable, so the mean slug length increases at the center of the channel (B) and decrease at the inlet and outlet.

Coherently with the analysis by delta, the mean of the slug length is lower in position C compared to position A for $f = \{1; 3\}$ ml/min, while for $f = 0.3$ ml/min the process slows down for the curved geometry inducing at an increase of the bubble length at the outlet.

It is worth to notice an inversion of the tendency for $f = \{0.3; 1\}$ ml/min where

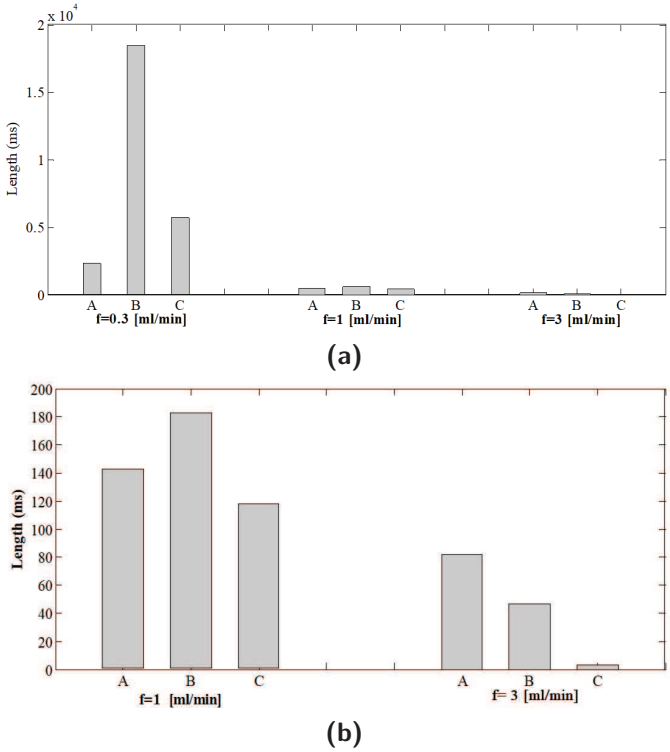

Fig. 1.18. Experimental $set-3$. The average length of the water intervals in the channel positions $\{A, B, C\}$ respectively close to the inlet, at the center and close to the outlet; (a) $f = \{0.3, 1, 3\}\ ml/min$; (b) a zoom for$f = \{1, 3\}\ ml/min$.

the mean slug length is greater at the center than at the inlet, compared with $f = 3\ ml/min$ in which the situation is opposite. The profile across three acquisition positions is decreasing, so the slug length decreases along the channel due to the input flow pressure increase.

A systematic experimental study on the slug flow patterns generation in an horizontal curved micro-channels of $\{320; 640\}\ \mu m$ width, where a continuous slug flow was generated by two upstream of water and air, is presented. The attention has been focused on three issues: the difference in the slug displacement in a straight channel compared with a serpentine; the role played by the input flow rates in the slugs flow patterns classification and the flow changes in different channel positions.

The photodiode signals acquired in all the experiments were analyzed, and organized in three experimental sets based on the investigated aspects. A classification

of the obtained slugs dynamic in slow and fast flow patterns was established, in slow patterns the long air intervals are combined with short water intervals (or vice versa), while in fast patterns both intervals are small and similar. The dependence of transition point between the two slugs regimes on the channel geometry and input flow rate was evinced.

From the experimental $set-1$ it was highlighted the difference in the flows generated in the straight and serpentine micro-channels but, above all, that by the serpentine geometry the robustness of the microfluidic processes to the flow input variations can be improved and controlled easily, also in fast conditions. From the experimental $set-2$, the changes in the flow due to the input flow rates for both slow and fast patterns in a serpentine was analyzed by the introduction of four indicators: the delta for the air/water presence, the slug length for slow patterns and the slug interdistance for fast patterns. In the slow flows, for $f < 1\ ml/min$, it was possible to notice that the air plays always a fundamental role and becomes dominant for $AF > 0.2$. Varying the AF, a synchronous increase and decrease of both air and water slugs lengths on different levels occurs and, only for $AF > 0.7$, their values are almost unvaried and stable: the air bubble lengths are almost three time greater than the water length. Based on that it is possible, in a generic geometry, to establish which flow rate gives a specified slug behaviour, although to quantify the exact value of the length is necessary to take into account the channel hydraulic resistance. In the fast flow for $f > 1\ ml/min$, increasing both air or water, the mean slug inter-distance and its variability is reduced, leading to a process stabilization toward a periodic regime. A fast train of small slugs can be produced with a modulation of the velocity set by the input flow rate with an a priori known uncertainty.

From the results of experimental $set-3$, it was possible to conclude that for slow input flow rates, the slowdown of the process induced by the curves is predominant and leads to an increase of the slug length at the outlet, while for fast input flow rates the increase of air compression, induced by the flow velocity, brings a reduction of the slug length along all the channel.

The results obtained highlight the advantages in the process control introduced by curve geometry, despite the presence of nonlinear phenomena. Technologically, the processes classification obtained by a simple analysis of optical signals, instead of

using costly and bulky equipment or invasive process detection systems represents a proof of concept for a future integration of both the detection and flow control in a single micro-system.

Chapter 2

Slug flows modelling by nonlinear systems synchronization

2.1 Experimental campaigns

The setup considered is the same described in Chapter 1, labelled $setup - 1$. The serpentine micro-channel $G3$ ($w = 640\ \mu m$, $l = 121\ mm$) was used (see Figure 1.4). The process was monitored at the center of straight part, tagged as point B in the figure. The signals acquired from the photodiodes were filtered, as described in detail in paragraph 1.2.

Two sets of 9 experiments were performed, where V_{air} and V_{water} represent the volumetric flow rates. To have a fast flow the input flow rates were set always greater than 1 ml/min.

In $campaign - A$, the air flow was fixed to $V_{air} = 1.2\ ml/min$ and in $campaign - B$ the water flow rate was $V_{water} = 1.6\ ml/min$. The second input flow rate was varied leading to different AF values per experiment (computed as in eq. 1.10) reported in Table 2.1. In $campaign - A$ the water dominance leads the AF in the range $[0.158 - 0.433]$ and in $campaign - B$ the air dominance brings the AF to $[0.433 - 0.804]$.

The values of the input flow rate were set considering the Capillary number and the Reynolds number. The Ca was always of the order of 10^{-3}, that confirms the theoretical expectancy of the slug formation. The Re was in the range $Re \in$

$[9.26 - 26.71]$ at the boundary with the laminar flow condition ($Re > 10$).

Tab. 2.1. The Air Fraction (AF) values per experiment in the Campaigns A and B.

Campaign A	Campaign B
V_{air}=1.2 ml/min	V_{water}=1.6 ml/min
0.158	0.433
0.167	0.614
0.182	0.659
0.194	0.708
0.198	0.733
0.233	0.761
0.267	0.776
0.347	0.794
0.433	0.804

2.2 Slug flows nonlinear characterization

In [48], it has been widely investigated the nonlinearity of the slugs flow and its classification through nonlinear indicators. Nonlinear time series analysis [61] has been applied to the experimental data in order to quantify the flow patterns and the bubbles' dynamics in terms of Largest Lyapunov exponent (LE). In Figure 2.1(a), considering both experimental campaigns, the values of LEs versus the AF are plotted. The two shaded areas are for the water dominance with $AF \in [0.1, 0.3]$ and air dominance with $AF \in [0.6, 0.8]$. In the range $AF \in [0.3, 0.6]$, the amount of air and water fed in the channel are almost balanced. A local peak associated with a rise in the LE trend and subsequently a drop can be detected in all the three areas.
For a in-depth analysis of the data, the frequency analysis of the time series was performed.

The obtained broadband spectrum resembles a bell-shaped curve, then its profile was approximated with a Gaussian model to characterize the peak in the spectrum and the area under the Gaussian curve, associated respectively to the mean slug inter-distance and its variability. The area under the Gaussian curve was considered proportional to the spectrum bandwidth. From a theoretical per-

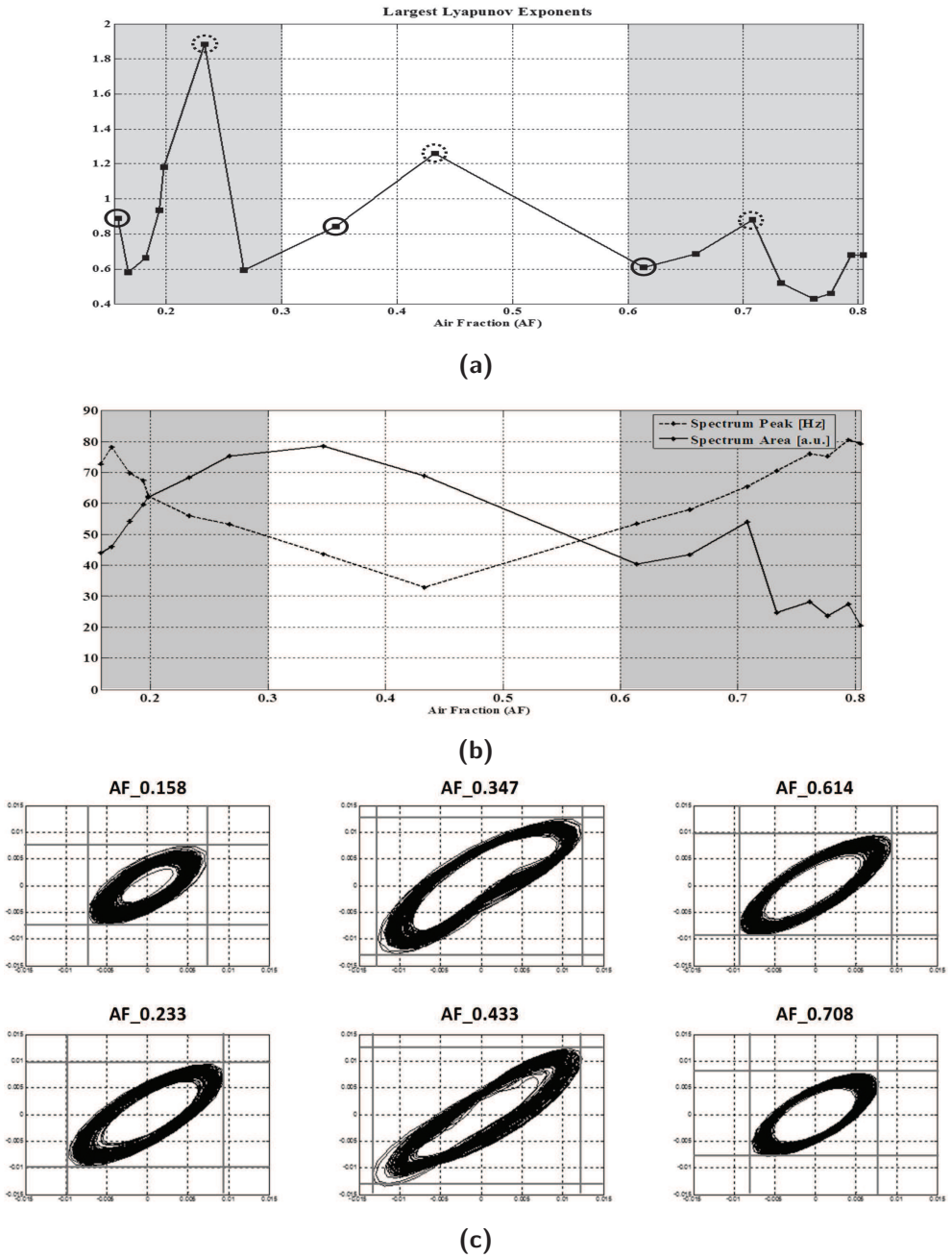

Fig. 2.1. (a) Largest Lyapunov exponent values versus the AF; the circled points are related to the conditions selected for the attractors reconstruction; (b) The frequency peak (gray dotted line) and area under the Gaussian (black solid line) versus the AF; (c) State-space representations at the top the experiments with $AF = [0.158, 0.347, 0.614]$, while at the bottom the experiments with $AF = [0.233, 0.433, 0.708]$.

spective, smaller is the bandwidth closer is the flow dynamics to a periodic behavior. The Figure 2.1(b) shows the peak frequency (grey dotted line) and the value of the area under the Gaussian (black solid line) versus AF. Corresponding to the water and air dominance, respectively, in the ranges $AF \in [0.1, 0.2]$ and $AF \in [0.7, 0.8]$, both trends show that the mean bubble inter-distance increases and its variability decreases. It can be confirmed by the two saddle points in the LE trend (Figure 2.1(a)) and proves that the process nonlinearity can be reduced by the increase in one input flow rate.
In Figure 2.1(c), the attractors obtained by the state space reconstruction in the six experiments, circled in Figure 2.1(a), are shown to give a visual characterization of the flow nonlinearity. At the top, there are the three experiments with the lowest LE values for $AF = [0.158, 0.347, 0.614]$ and, at the bottom, the experiments with the highest LE values for $AF = [0.233, 0.433, 0.708]$. The attractors comparison remarks that the stretching is greater when in the micro-channel there is no air or water dominance and the two phases are balanced. It is important to evidence that the attractors shape is always a single scroll.

2.3 Master-Slave synchronization

One property of the chaotic systems is the sensitivity to initial conditions, thus two identical systems starting from slightly different points in the state space evolve, in long-term, in a totally uncorrelated manner. The synchronization approach allows to drive the two systems toward a correlated time evolution. The two systems are named as Master and Slave. In this contest, the synchronization theory was used as a framework for the modelling and identification of real-world processes by means of experimental data.
The synchronization schemes are classified in two main classes: unidirectional or bidirectional coupling. In the identification process it is useful to use an unidirectional synchronization scheme that considers only how one system (Master) can affect a second system (Slave). Particularly, in the *method of decomposition into sub-systems*, the Slave system can be decomposed at least into two subsystems: a drive system and a stable response sub-system such that we can force

the drive system to follow a definite state variable (driven variable). It has been demonstrated that with this procedure the systems synchronize also in presence of noise [62]. Following this scheme and assuming a time series as a state variable of an unknown Master system, it can be estimated an optimal set of parameters of a Slave known model to reach the synchronization between the asymptotic time evolution of at least one of its state variables and the experimental data used to drive it [63].

It is possible to distinguish four main classes of synchronized behavior [64]: complete synchronization (CS) consists in a perfect matching of the two chaotic trajectories, the systems forget their initial conditions continuing to evolve chaotically; phase synchronization (PS) occurs in oscillators when their phases are locked, while amplitudes remain almost uncorrelated; lag synchronization (LS) occurs when the two trajectories are locked both in phase and amplitude but with a finite time lag; generalized synchronization (GS) is achieved when the dynamics of one of the coupled systems can be expressed as a function of the other dynamics.

The phase or lag synchronization are most significative being the slug passage in the flow strictly related to the frequency and the phase of the signal more than to its amplitude.

The experimental time series acquired from the microfluidic process, Y_m, was assumed as the asymptotic behavior of a generic state variable of an unknown Master system and this information was used to drive a Slave system with a known model with undefined parameters. The Slave system selected was the Chua's oscilltaor model being a nonlinear systems capable of reproducing a great number of experimental phenomena [46]. The dimensionless state equation of the Chua's oscillator follows.

$$\frac{dx}{dt} = k\alpha(y(t) - x(t) - f(x(t))) \tag{2.1}$$

$$\frac{dy}{dt} = k(x(t) - y(t) + z(t)) \tag{2.2}$$

$$\frac{dz}{dt} = k(-\beta y(t) - \gamma z(t)) \tag{2.3}$$

$$f(x(t)) = m_1 x(t) + \frac{1}{2}(m_0 - m_1)\{|\, x(t)+1 \,| - |\, x(t)-1 \,|\} \tag{2.4}$$

where x, y, and z are the state variables and α, β, γ, m_0 and m_1 the parameters. The unidirectional synchronization scheme based on the decomposition method was used and the Master-Slave system equations were re-written as follows:

$$\frac{dx(t)}{dt} = k\alpha(Y_m(t) - x(t) - f(x(t))) \tag{2.5}$$

$$\frac{dz(t)}{dt} = k(-\beta Y_m(t) - \gamma z(t)) \tag{2.6}$$

where the microfluidic time series Y_m affects the sub-system formed by the x and z variables of Chua's model. The drive sub-system of eqs.2.5-2.6 is solved by using the Dormand-Prince method [65] with fixed time-step T_s.

The equation related to the variable y is decoupled from the system and used to verify the convergence criteria, as in the following equations:

$$\frac{dy}{dt} = k(x(t) - Y_m(t) + z(t)) \tag{2.7}$$

$$lim_{t\to\infty} \mid y(t) - Y_m(t) \mid = 0 \tag{2.8}$$

The eq. 2.8 was implemented using as optimization method the genetic algorithm (GA) [47]. The optimal value of the parameters set $\{\alpha, \beta, \gamma, T_s\}$ that minimizes the error fitness function was searched in eq. 2.9. The parameter T_s is the sample step used during the simulation and it was included in the parameter set to be tuned with the changes in the time series due to the sample frequency at different slug flow velocities.

The root mean square error between the time series Y_m and the y state variable of the Chua's oscillator was chosen as error index (see eq. 2.9).

$$I\{\alpha, \beta, \gamma, T_s\} = \sqrt{\frac{\sum_{n=1}^{N}(Y_m(n) - y(nT_s))^2}{N}} \tag{2.9}$$

By a visual inspection of the Chua single-scroll attractor that can be obtained by tuning the parameters of the model [46], it was selected the one reported in plate

Tab. 2.2. Parameters for the Genetic Algorithm.

NIND	MAXG	GGAP	PREC
8	20	8	7

34 of [46] associated with the parameter set $\{\alpha = 1800, \beta = 10000, \gamma = 0\}$ and $\{m_0 = -1.026, m_1 = -0.982\}$. Starting from this condition, the GA algorithm was set to search the optimal parameters set $\{\alpha, \beta, \gamma\}$ respectively in the ranges $[1700, 2000]$, $[9500, 10000]$, $[0, 1]$, whereas the parameters of eq.2.4 were maintained fixed.

Being the sample frequency during the time series acquisition 1 kHz, the time step T_s was searched in the range $[0.001, 0.007]$. In the optimization procedure to set properly the GA parameters in Table 2.2 was fundamental: the number of individuals, the maximum number of generations, the generation gap and the precision.

2.4 Slug flows models

Each time series Y_m was normalized to zero mean and unit variance and two intervals of 5 seconds were extracted to construct two different sets used in the identification procedure: the training set and the test set.

For all the 18 experiments considered the optimal error index $I\{\alpha, \beta, \gamma, T_s\}$ obtained was in the training and test respectively of order of 10^{-2}, and 1. The optimal values of $\{\alpha, \beta, \gamma\}$ identified in the training phase are reported per experiment through the AF in Figure 2.2. The three plots describe the parameter changes per experimental condition. The α trend is similar to the one of area spectrum in Figure 2.1(b) (solid black line). It can be correlated with the process nonlinearity induced by the co-existence of the two phases in the micro-channel when there is not a flow dominance. Considering the β plot three areas can be distinguished as in the LE trend (see Figure 2.1(a)) with a peak for the same AF values. That remarks the relation between this parameter and the flow dynamic nonlinearity. γ oscillates between $[0.5, 1]$ and it is constant in the AF range $[0.3, 0.6]$ in the condition of no fluid dominance.

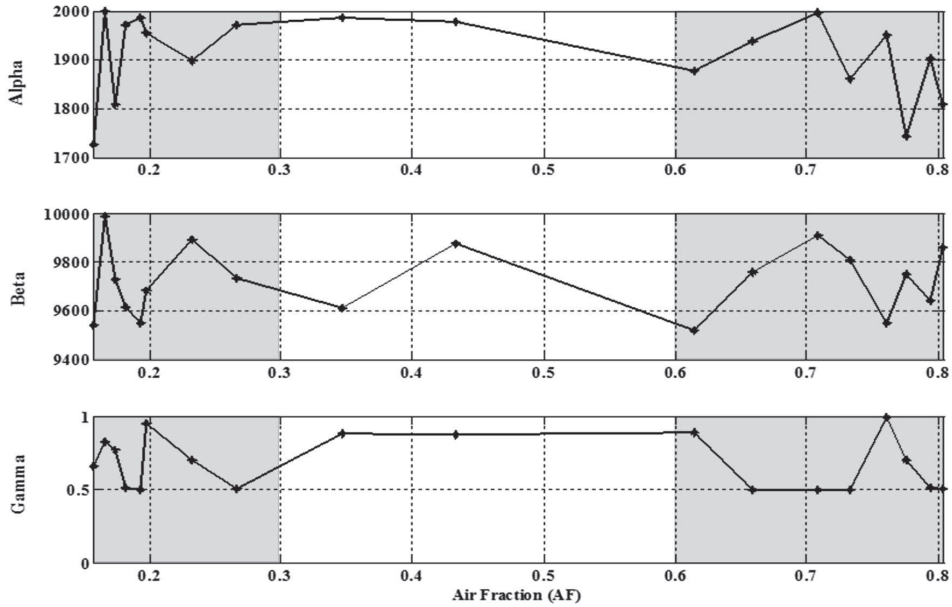

Fig. 2.2. The trends of the optimal parameters set $\{\alpha, \beta, \gamma\}$ of the Chua's model per experiments (versus AF).

These optimal parameters $\{\alpha, \beta, \gamma\}$ and the optimal time step T_s have been used in the comparison with the test data set (see Figure 2.2). For the set of experiments $AF \in \{0.158, 0.347, 0.614\}$, the state space representation comparisons between the microfluidic time series Y_M of the test set and the identified y state variable are shown in Figure 2.3.

Figure 2.4(a)-(c) show the comparisons of the experimental time series Y_M of the test set (grey dotted line) and the identified y state variable (black solid line) for three experiments with $AF \in \{0.158, 0.347, 0.614\}$.

The zooms in a time interval of about 0.5 s evidence the lag synchronization error, the synchronization occurs for a certain time lag and then is lost. The amplitude of the two signals matches mostly along all the time evolution.

For the same three experiments the results are enforced by looking at the spectra in Figure 2.5 and at the state space representations in Figure 2.3(a) - Figure 2.3(c). The Fourier spectra of the three identified state variable y for the selected experiments (black lines) have been compared with the spectra of the three experimental time series (grey lines). In the spectra of the identified signals it is possible to no-

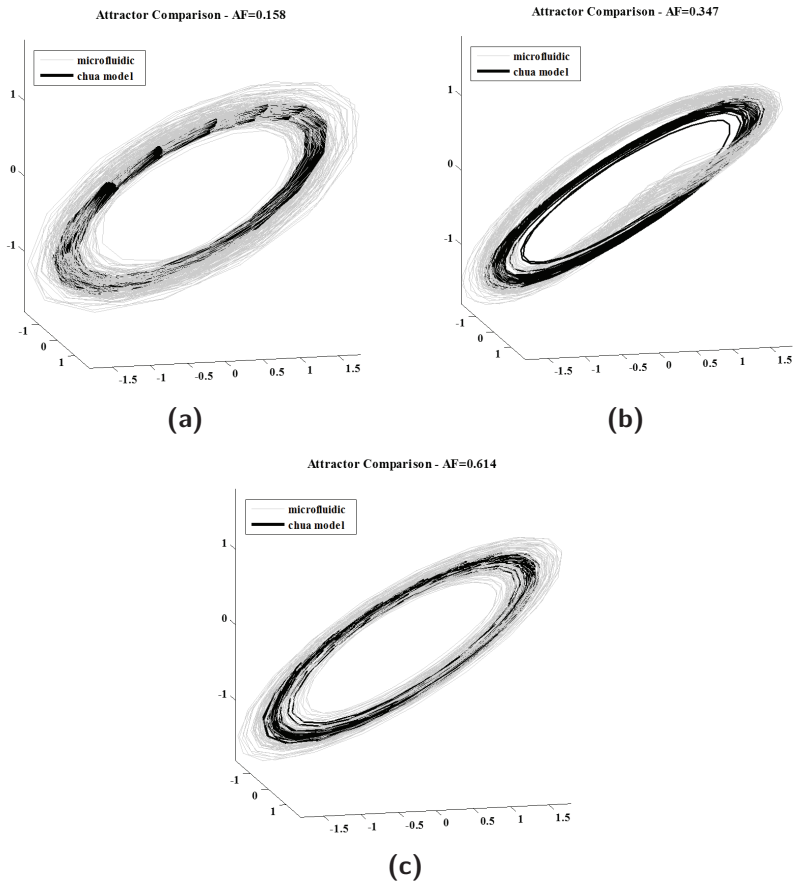

Fig. 2.3. State space representations comparison between the microfluidic time series Y_m of the test set (grey dotted line) and the identified y state variable related to the test set (black solid line) for the experiments with (a) AF=0.158; (b) AF=0.347; (c) AF=0.614.

tice always a satisfactory match in the frequency peaks but a smaller bandwidth than in the experimental time series. Coherently, in the superimposition of the y and Y_m state space representations the attractors show the same span but with same difference in their variability.

To evaluate the performance of the lag synchronization, the cross-correlation between the micro-fluidic time series in test set and the identified y-state variable was computed for all the experiments. The extraction of the zero-lag correlation and delay at the first maximum (d) has allowed to determine the lag interval range and its variability across the time series. The synchronization lag varies per ex-

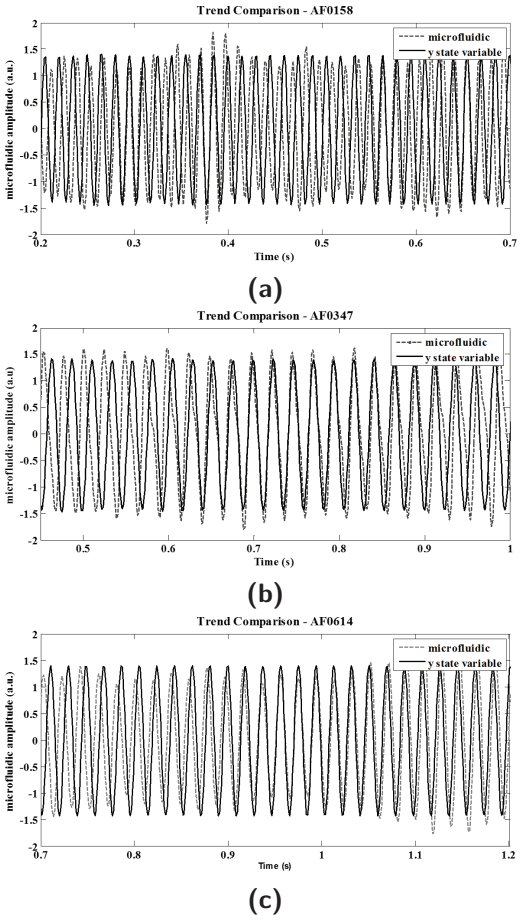

Fig. 2.4. A time zoom of the comparison between the microfluidcs time series Y_m of the test set (grey dotted line) and the identified y state variable (black solid line) for the experiments with (a) $AF = 0.158$; (b) $AF = 0.347$; (c) $AF = 0.614$.

periment in a range between $[40, 200]$ ms. The delay associate to the maximum in the cross-correlation was considered as the maximum shift of the two dynamics to have a best match in a time lag.

To evidence that, in Figure 2.6 for the experiment $AF = 0.158$ the trends comparison of the microfluidic time series and the identified y-state variable is presented in a time interval of 0.1 s for different delay $d \in \{0, 3, 7\}$ ms. In the subplot at the top no shift is applied, then in the subplot at the center a shift $d = 3$ ms leads to the lag synchronization in the first interval of 0.4 s. In the subplot at the bottom, the maximum delay detected for this experiment $d = 7$ ms is applied leading to the lag synchronization in the last interval of 0.4 s. The value of this delay in ms

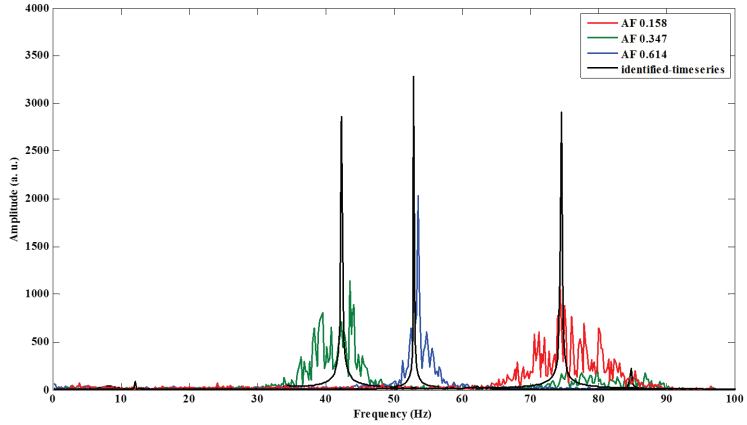

Fig. 2.5. For three experiments with $AF \in \{0.158, 0.347, 0.614\}$ the Fourier spectra of the identified y state variable are superimposed in black and compared with the three respective spectra of the experimental time series of the test set in colors.

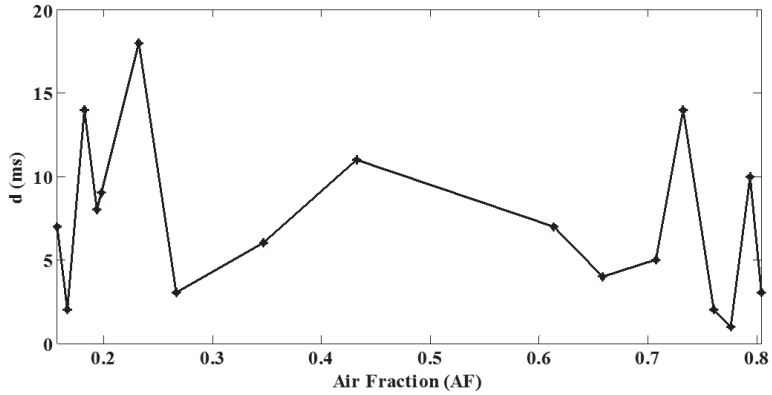

Fig. 2.7. The value of the delay d in ms for all the experiments.

for all the experiments is shown in Figure 2.7. It can be noticed a trend similar to that of LEs (see Figure 2.1(a)), so increasing the processes nonlinearity the range of variability of the shift increases. A class of models can be defined to identify the displacement of the slugs in a microfluidic channel in unknown experimental conditions. In the identification procedure adopted the experimental time series acquired from the microfluidic process was assumed as a generic state variable of an unknown Master system and this information was used to drive the Chua's slave system, with a known model and undefined parameters. By the genetic algorithm optimization procedure was searched a parameter set of the Chua's model

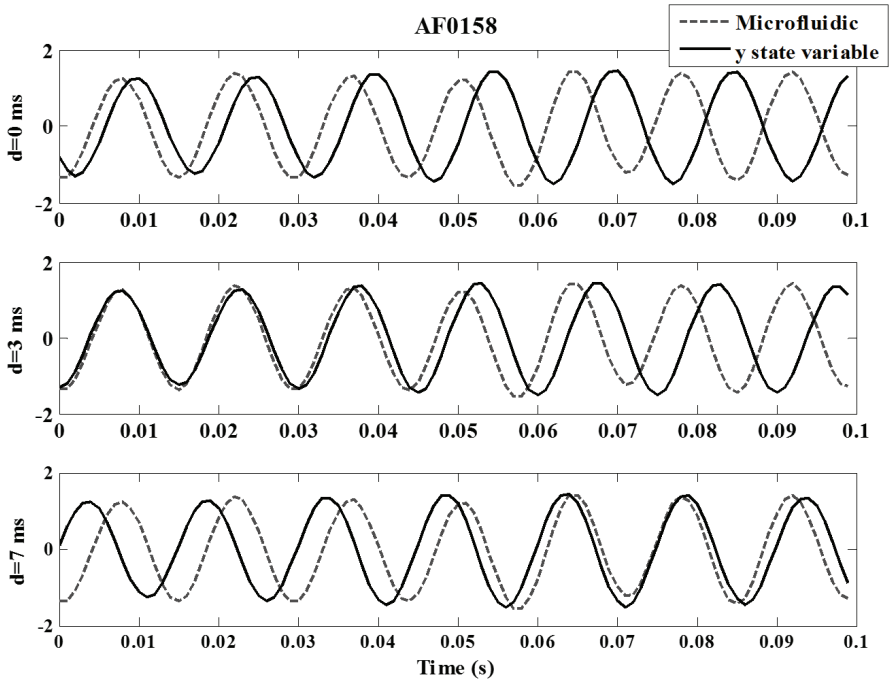

Fig. 2.6. The trends comparison (for the experiment $AF = 0.158$) of the microfluidic time series and the identified y-state variable is presented in a time interval of $0.1\ s$ for different delay $d \in \{0, 3, 7\}\ ms$.

that can guarantee the two systems synchronization, leading to the time series identification. The lag synchronization was reached for all the experiments.

This result highlights the possibility with a single model to identify a variety of flow regimes generated in two-phase microfluidic processes, independently of how the processes have been generated, no directed relations with the input flow rate used are in the model.

The opportunity of an adaptive model for process identification to be used in unknown experimental conditions can represent a great advantage in the microfluidics process control towards compact and robust Lab on a Chip (LOC) technology.

Chapter 3

Slug flows tracking by NARX models

3.1 Experimental campaign

The setup considered is the same described in Chapter 1, labelled $setup - 1$. The serpentine micro-channel $G3$ ($w = 640\ \mu m$, $l = 121\ mm$) is used (see Figure 1.4). The process was monitored at the center of straight part, tagged as point B in the figure, to investigate on the flow after the slugs have experienced the mixing meander. The signals acquired from the photodiodes were filtered, as described in detail in paragraph 1.2.
Two experimental campaigns were designed. Each campaign consists of 12 experiments where V_{air} and V_{water} represent the volumetric flow rates. To have a fast flow the input flow rates were set always greater than $1ml/min$.
In the campaign tagged $campaign - A$, the flow rate of air was fixed to $V_{air} = 1.2\ ml/min$ and the water changes in the range $V_{water} \in [1.6 - 6.4]\ ml/min$. In the campaign tagged $campaign - B$, the water flow rate was fixed to $V_{water} = 1.6\ ml/min$ and the air changes in the range $V_{air} \in [1.2 - 8.5]\ ml/min$.
The Air Fraction (AF), computed as in eq. 1.10, was used to tag the experiments based on the amount of air at inlet respect to the water. Its values are reported in Table 3.1. In $campaign - A$, the AF is in the range $[0.158 - 0.433]$, whereas in $campaign - B$ in $[0.521 - 0.843]$. The values of the input flow rate were set con-

sidering the Capillary number and the Reynolds number. The Ca was always of the order of 10^{-3}, that confirms the theoretical expectancy of the slug formation. The Re was in the range $Re \in [9.26 - 33.53]$ at the boundary with the laminar flow condition ($Re > 10$).

Tab. 3.1. The Air Fraction (AF) and Reynolds Number (Re) per experiment in campaigns A and B.

$campaign - A$ $V_{air} = 1.2\ ml/min$		$campaign - B$ $V_{water} = 1.6\ ml/min$	
AF	Re	AF	Re
0.158	25.41	0.521	10.96
0.160	25.07	0.614	13.61
0.162	24.74	0.659	15.38
0.164	24.47	0.708	17.98
0.167	24.07	0.733	19.62
0.174	23.07	0.761	21.96
0.182	22.06	0.776	23.43
0.198	20.29	0.794	25.44
0.233	17.25	0.804	26.71
0.267	15.04	0.817	28.71
0.347	11.57	0.826	30.08
0.433	9.26	0.843	33.53

3.2 Multi-scale dynamics in slug flows

Considering fast flows, it was possible to detect an oscillating flow trend on two levels, representing the air and water passages (see for example the Figure 1.8(a) and (b)). Each experiment lasts 20 s, evaluated to be a recording time sufficient to capture the flow dynamics considering that the air and water passages occur in about $[5 - 10]$ ms. The signals analysis in the frequency domain was applied to compute two indicators: $Peak$ (ω_p) and $Width$ (ω_b). For each experiment, the signal spectrum was fit using a Gaussian model whose mean and standard deviation were correlated to the frequency spectrum peak and the bandwidth (see in Figure 3.1). To evaluate these parameters was applied an iterative procedure based on an unconstrained nonlinear optimization algorithm [60].
The $Peak$ gives information about the mean of the slugs inter-distance, greater is the frequency faster is the slug flows, and the $Width$ is an indicator of its variation,

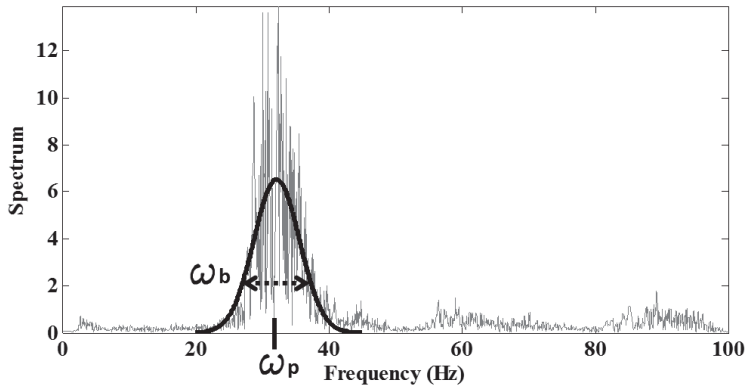

Fig. 3.1. The signal spectrum fitted with a Gaussian model whose mean and standard deviation were correlated with the frequency of the slugs passage.

as smaller is the bandwidth closer is the flow dynamics to a periodic behavior.
To use these parameters for the flow identification it was necessary to investigate their robustness for the characterization of the process in different time scales. On this purpose, four different time windows were considered of respectively $[1; 3; 5; 13]$ s. All the optical signals were analyzed in those time windows to extract $\{\omega_p, \omega_b\}$ per experiment. The values obtained versus AF in the four conditions are plotted respectively in Figure 3.2. It can be observed in Figure 3.2(a) that the trend of the parameter ω_p is unchanged varying the time-scale, and ranges in $\omega_p \in [30-90]$ Hz for both $campaign-A$ and $campaign-B$. The slowest slugs train is when the two fluids are counterbalanced at the inlet $AF = 0.433$.
As it can be noticed in Figure 3.2(b), the trend of the parameter ω_b is on two levels: a greater one in $campaign-A$ for AF $\in [0.158-0.433]$ with the water dominance at the inlet and a lower one in $campaign-B$ for AF $\in [0.521-0.843]$ with the air dominance at the inlet. That allows us to assert that water flow rate dominance at the inlet increases the slug flows irregularity, enhancing the sensitivity of ω_b to the time-scale change. Moreover, it is important to highlight that both parameters are sufficiently stable to be used for the flows identification.

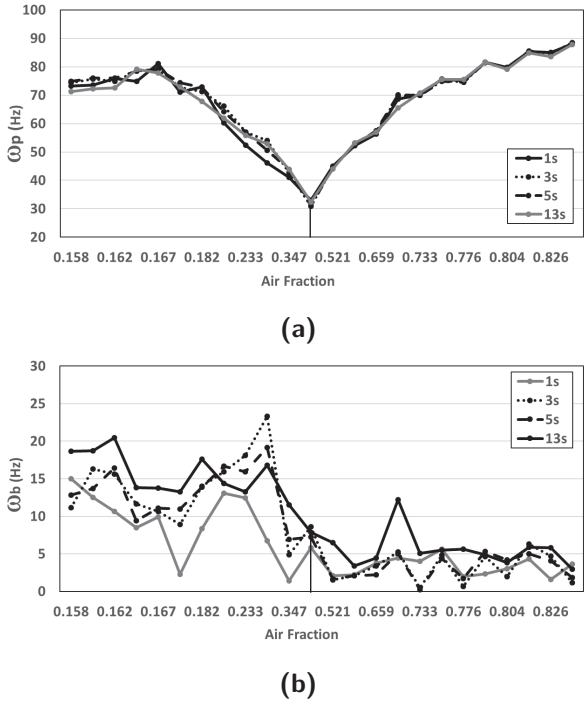

Fig. 3.2. Trends of parameters (a) ω_p and (b) ω_b per experiment versus AF for the four time-windows of length $[1; 3; 5; 13]$ s. For a easy reading of the AF values on the x-axis, those values are graduated as samples not taking in to account their linear distribution.

3.3 NARX models definition

For the data-driven identification processes the nonlinear autoregressive exogenous models (NARX) were considered, as follows in equation 3.1.

$$\begin{aligned} y(k) = F(y(k-1), ..., y(k-n_a), \\ u(k-n_k), ..., u(k-n_k-n_b+1)) + e(k) \end{aligned} \tag{3.1}$$

The process output $y(k)$ at time k is obtained by the nonlinear regression mapping through the function F of the process output variable itself, the process inputs $(u(k))$ and the noise $e(k)$. $\{n_a, n_b, n_k\}$ are respectively the regressors associated to the output and input variable, and the time-delay on the input. The regressor vector, generally used in the models, is defined in eq. 3.2.

$$x(k) = [y(k-1), ..., y(k-n_a), u(k-n_k), ..., u(k-n_k-n_b+1)]^T \tag{3.2}$$

Two different representations of the nonlinear estimator F were considered in this work: the standard neural networks (NN) and the wavelet networks (WN).
In the NARX modelling by using NN [43] the function F is implemented as a multi-layer feed-forward neural network. The topology defined consisted of one hidden layer with an optimal number of nodes N to be set. Based on that the model in eq. 3.1 can be rewritten as in eq. 3.3.

$$y(k) = f_2[LW * f_1(IW * p + b_1) + b_2] \tag{3.3}$$

where LW $[1 \times N]$ and b_1 $[N \times 1]$ are weight matrix and bias vector of the one-hidden layer, IW $[N \times n_a]$ is the input weight matrix, and b_2 $[1 \times 1]$ is the bias of the output layer. The sigmoidal function (f_1) was chosen for each node of the hidden layer (f_1), and the linear function (f_2) for the node of the output layer. The back-propagation algorithm was used during training for the parameters identification. It is a fast supervised algorithm that updates weights and biases according to Levenberg-Marquardt optimization. The initial conditions for the weights and biases are random values in an appropriate range. The one hidden-layer architecture was chosen to maintain the equivalence with the WN model.
The NARX modelling by using WN [44, 66] is an approach for systems identification in which the nonlinear function F is approximated as the superposition of dilated and translated version of a single function, the mother wavelet. The idea of combining wavelet and neural network arises from the similarity between the wavelet decomposition and one-hidden layer neural network. The following eq. 3.4 provides a specific re-formulation of eq. 3.1:

$$F(x) = L^T * (x - r) + d + \sum_{k=1}^{N} a_k * g(b_k(x - r))) \tag{3.4}$$

where $L^T * (x - r) + d$ is the output of the linear function block, L is the vector of the linear coefficients, d is a scalar offset, and r is the mean of the regressors x. The nonlinear function g is the wavelet, and a_k and b_k are the scaling and wavelet parameters to be identified together with d and L.

The parameters a_k and b_k depend on the number of nodes N and on the dimension of regressor vector x. The algorithm used for the parameters estimation was a fast non-iterative technique with successive refinements after the first estimation [44].

3.3.1 Patterns creation

Another important aspect in the model definition is the pattern characterization.
The air and water input flow rates, respectively $[u_1(k), u_2(k)]$, were the two input variables and the optical signal related to slug passage in the micro-channel $y(k)$ was assumed as the output variable. The output variable $y(k)$ was always normalized in the range $[-1; 1]$.
Two classes of patterns were constructed and named respectively: *Single-Pattern* and *Multi-Pattern*.
The *Single-Pattern* training and test patterns were built using the input-output data for each one of the 24 experiments. The training patterns were used for the parameters identification and the test patterns for the performance evaluation, both built of the same length including up to 7000 data samples (7 s of experiment). For a future models integration in real-time control scheme, the final choice was to have 1s, where it would be possible to detect the passage of [10, 30] slugs.
In the *Multi-Pattern* the input-output data were made up by appending 1 s fragments from more experiments in a sequence. Three *Multi-Pattern* sets were considered collecting three, five and seven experiments, as follows:

- $Set-1$, $AF \in [0.182; 0.433; 0.733]$;
- $Set-2$, $AF \in [0.162; 0.182; 0.433; 0.733; 0.826]$;
- $Set-3$, $AF \in [0.162; 0.182; 0.267; 0.433; 0.614; 0.733; 0.826]$.

In Figure 3.3, the dynamics of the output variable $y(k)$ for $Set-1$, $Set-2$ and $Set-3$ are shown. In all the three cases the variable $y(k)$ was analyzed in the frequency domain. In the three spectra were distinguishable respectively the three, five and seven peaks (ω_p) identified previously in the analysis per experiment, and reported in Table 3.2 as expected peaks.

Tab. 3.2. The peaks detected (ω_p) in the spectra of the estimated signals for three sets $\{Set-1;\ Set-2;\ Set-3\}$ with both NN and WN models compared with the expected values computed using the data of the single experiments per AF.

AF		0.162	0.182	0.267	0.433	0.614	0.733	0.826
Expected Peak		75.92	76.72	46.09	33.05	52.17	70.14	85.07
Set-1	WN	-	72.95	-	33.64	-	69.92	-
	NN	-	72.95	-	34.64	-	70.19	-
Set-2	WN	74.14	75.54	-	34.97	-	69.74	84.53
	NN	73.14	76.34	-	34.57	-	70.54	85.73
Set-3	WN	73.65	75.93	48.96	32.12	54.10	69.08	84.21
	NN	72.94	76.93	47.39	35.11	52.38	69.8	86.78

Also in this case the length of the training and test patterns were set including the same number of samples $\{3000,\ 5000,\ 7000\}$ respectively for $\{Set-1,\ Set-2,\ Set-3\}$.

3.3.2 Performance indices

Being the two inputs constant, the input regressor orders n_b and delay n_k were set to 1, whereas the range considered for the output regressor n_a was $[1-7]$, as in eq. 3.5.

$$\hat{y(k)} = \hat{F}(\hat{y}(k-1), ..., \hat{y}(k-n_a), u_1(k-1), u_2(k-1)) \tag{3.5}$$

where $\hat{y}(k)$ is the estimated output and $\hat{F}$ the identified nonlinear function.
The optimal number of nodes in the model was searched in the set $node = \{5; 10; 15\}$. The performance of identified models were evaluated both in time and in frequency domain by using three indices: the root mean square error ($RMSE(\%)$), the frequency peak shift ($\Delta_{Peak}(\%)$) and the width difference ($\Delta_{Width}(\%)$), as follows:

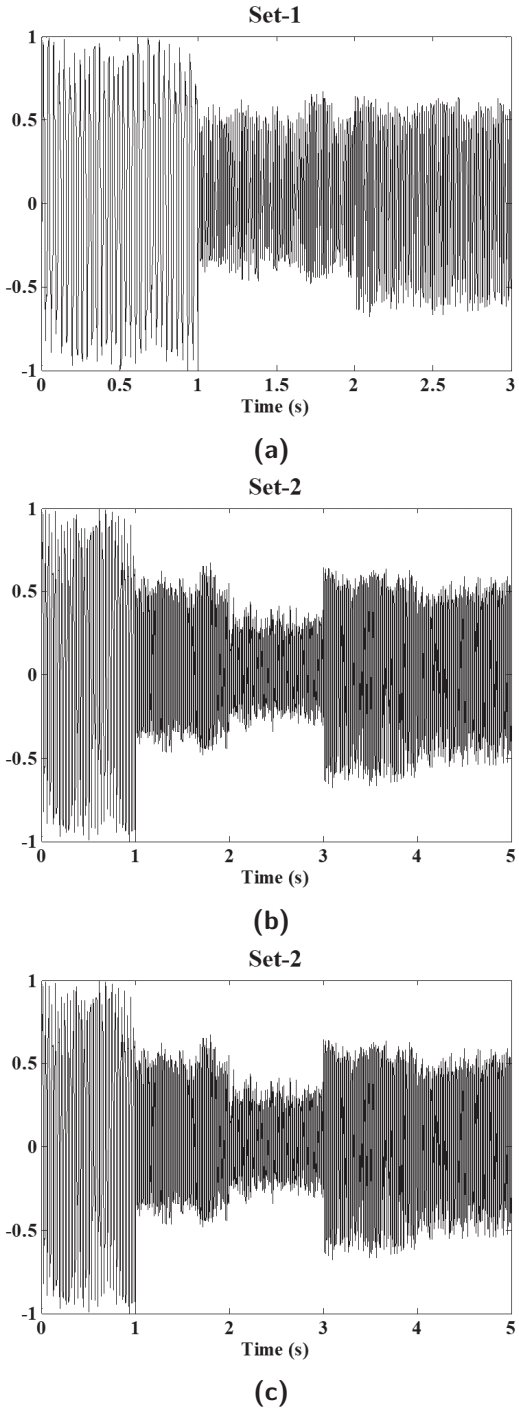

Fig. 3.3. The variable $y(k)$ time-constructed for *Multi-Pattern* and normalized $[-1;1]$. (a) $Set-1$: sequence including 1 s of three experiments; (b) $Set-2$: sequence of including 1 s of five experiments; (c) $Set-3$: sequence including 1 s of seven experiments.

$$RMSE(\%) = \sqrt{\sum_{k=1}^{N} \frac{(y(k)-\hat{y}(k))^2}{N_{sample}}} * 100 \tag{3.6}$$

$$\Delta_{Peak}(\%) = \frac{|\omega_p - \hat{\omega}_p|}{f_{out}} * 100 \tag{3.7}$$

and

$$\Delta_{Width}(\%) = \frac{|\omega_b - \hat{\omega}_b|}{f_{out}} * 100 \tag{3.8}$$

where $\hat{y}$, $\hat{\omega}_p$ and $\hat{\omega}_b$ are respectively for the identified signal, and the frequency at the spectrum peak and the bandwidth of the spectrum. Those indices are evaluated in percentage. N is the number of samples in the patterns and $f_{out} = 100\ Hz$ is the whole spectrum range.

To determine the optimal number of the auto-regressions and nodes, the attention was focus on one experiment ($V_{air} = 1.2\ ml/min$; $V_{water} = 1.5\ ml/min$, with $AF = 0.433$), repeated twice one time per campaign and giving consisted results. The identification procedure was repeated for $n_a \in [1; 7]$ using $\{5, 10, 15\}$ nodes. In Figure 3.4, the bar diagram of the $RMSE(\%)$ summarizes the results. It is possible to observe that, a greatest number of nodes does not bring a significant improvement in the model, in spite of the model complexity increases and in some case even a worsening can be noticed. The best choice was for 10 *nodes*. Regarding the auto-regression order it is evident a decreasing trend with a first local minimum at $n_a = 2$, and then a stabilization for $n_a \geq 4$ at the same error level than in $n_a = 2$.

In Figure 3.5(a) and (b) two zooms of the real and identified signals for ($n_a = 5$ with $node = 5$) and ($n_a = 4$ with $node = 10$) are shown: it is evident that although no significant difference is detectable by the error values, the quality of the signals is not satisfactory. In Figure 3.5(c) it is presented the comparison of the real and identified dynamics for the selected optimal condition ($n_a = 2$ and $node = 10$) in the time domain.

Based on these results, the pair of parameters for the model structure in the identification of the dynamics was set to ($n_a = 2$; $node = 10$). The 24 models, one per experiment, were identified in *Single-Pattern* case study, and three models, one

per set, was obtained in the *Multi-Pattern* case study.
In the test phase, for both NN and WN models, the estimate output values in the first two iterations $k = \{1,\ 2\}$ ($\{\hat{y}(1), \hat{y}(2)\}$) were set equal to the first two values of the output signal in the test pattern ($\{y(1), y(2)\}$). It is worth to underline that a closed-form model is obtained with the identification by the WN, so the model, after the first two iterations, evolves autonomously from the real-data. Conversely, the open-form model, identified with the NN procedure, can be used feeding the model either with the real-data or the identified one. In the test phase for the NN models, two modalities to compute the estimated output $\hat{y}(k)$ were considered: either by feeding the model with previous samples of the estimated output itself or supplying the real-data after a certain number of iterations (T in samples) for two iterations (being $n_a = 2$). Only in the first case, when $\hat{y}(k)$ was obtained autonomously by the real-data, the NN model performance can be compared with the one of the WN model. The use of real-data, avoiding the problem of the error propagation, brings a drastic reduction of the error.

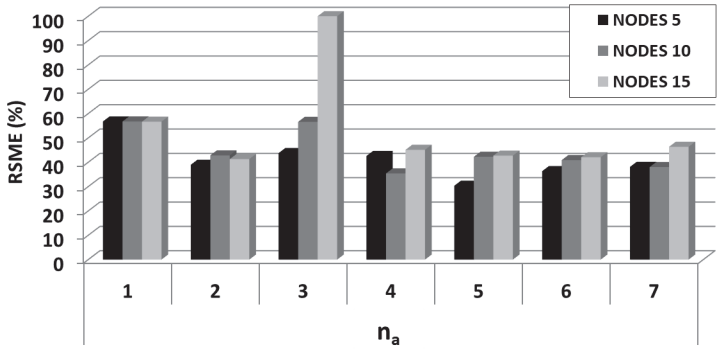

Fig. 3.4. Comparisons of the error $RMSE(\%)$ related to the identification of the experiment ($V_{air} = 1.2\ ml/min$; $V_{water} = 1.5\ ml/min$, with $AF = 0.433$).

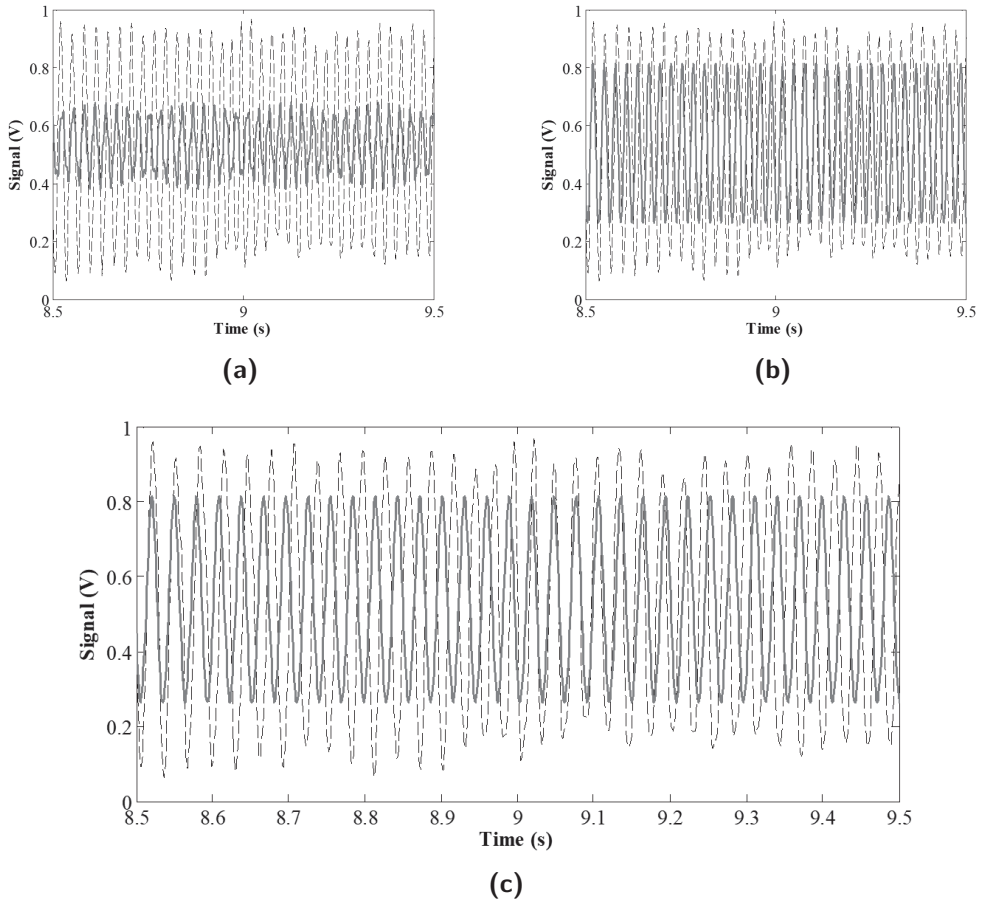

Fig. 3.5. Zoom to compare the trends related to the experiment ($V_{air} = 1.2\ ml/min$; $V_{water} = 1.5\ ml/min$, with $AF = 0.433$) with (a) ($n_a = 5$; $node = 5$); (b) ($n_a = 4$; $node = 10$); (c) ($n_a = 2$; $node = 10$). The real signal is the dotted black line and the identified trend is in grey.

3.4 Slug flows identification

3.4.1 Tracking by Single-Pattern

The aim of this case study was to define models that are able to capture the nonlinear dynamics of time series correlated to the slug passage in micro-channels. For both NN and WN architectures, the one-layer topology was chosen. Based on the results of the previous section, the optimal number of nonlinear unities (nodes) in the WN models was set to $node = 10$ for all the experiments.

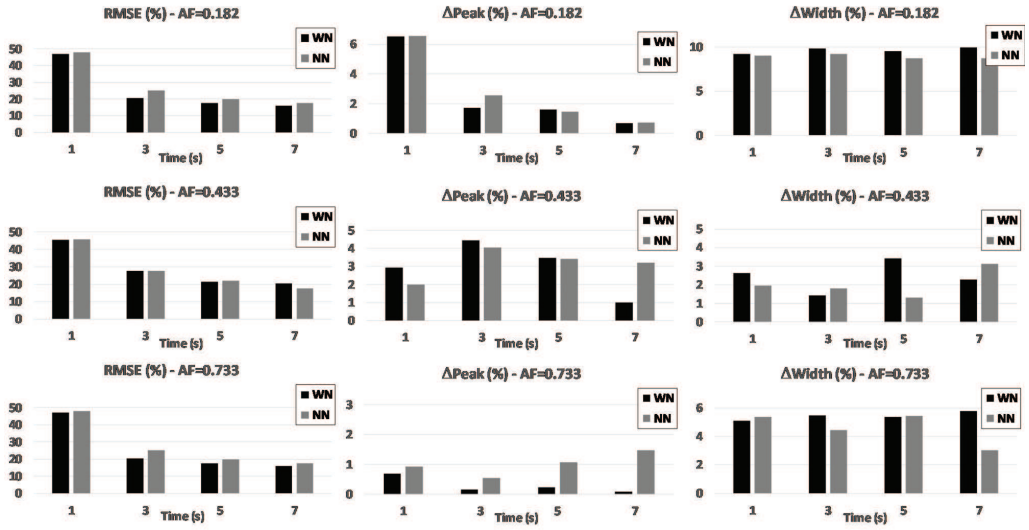

Fig. 3.6. The bar histograms of the performance indices related to the three experiments $AF \in \{0.182; 0.433; 0.733\}$ (organized by row) for WN model (in black) and NN model (in grey) changing the pattern duration in the set $\{1; 3; 5; 7\}$ s.

For the NN models, the optimal numbers of nodes was searched in set $node = [1; 3; 5; 7; 10]$ by repeating the identification process three times for all the 24 experiments. It was possible to compute the percentage of failures (*fail*), as the number of times in which $\hat{y}$ was not properly identified over the total number of the experiments. This percentage of failures decreases $fails(\%) \in \{91.6; 45.8; 12.5; 8.3; 0\}$ respectively as the number of nodes increases $node \in \{1; 3; 5; 7; 10\}$. Then, also for the NN architecture, the number of nodes was set to $node = 10$.

The first aspect to be studied was the change of the identified models performance varying the length of the train and test patterns in the set $\{1; 3; 5; 7\}$ s. The attention was focused on the experiments $AF \in \{0.182; 0.433; 0.733\}$.

In Figure 3.6, the bar histograms show the performance indices $\{RMSE(\%), \Delta_{Peak}(\%), \Delta_{Width}(\%)\}$ related to the three experiments (organized by row) for WN models (in black) and NN models (in grey) changing the pattern duration. It is possible to observe that, the performance of the two classes of models NN and WN are quite equivalent, and the $\{\Delta_{Peak}(\%), \Delta_{Width}(\%)\}$ are respectively lower than $\{5\%, 10\%\}$ for all the patterns lengths. Instead a great difference is visible in the $RMSE(\%)$ for the pattern length of 1 s, the 50% error is double respect to

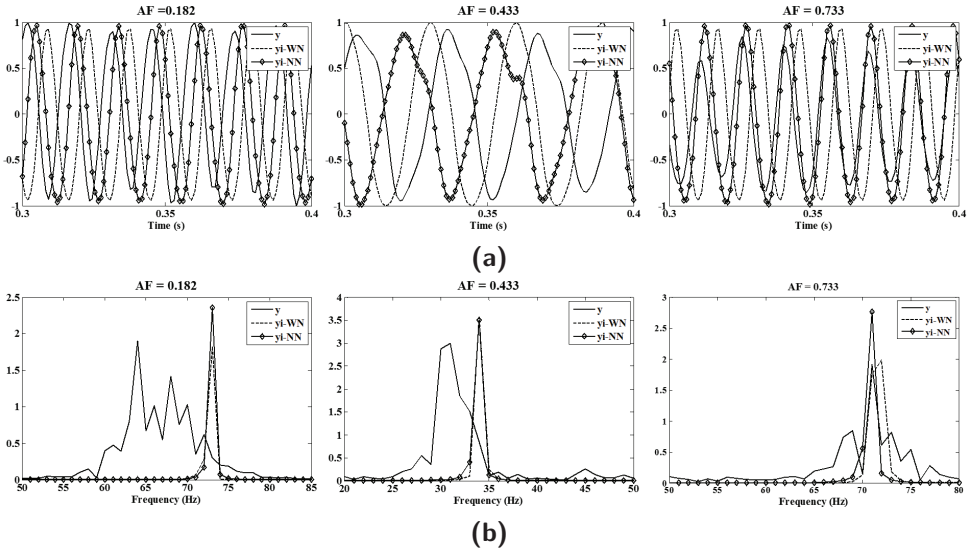

Fig. 3.7. The comparison of (a) the trends and (b) the spectra of the signal $y(k)$ (solid line) with the signals estimated by the NN ($\hat{y}_{NN}(k)$, dotted line) and the WN ($\hat{y}_{WN}(k)$, dashed line) in the time interval $[0.3 - 0.4]$ s.

the value of the 25% for longer time windows.

For better understanding of this phenomenon, for the three experiments in Figure 3.7 the comparison of the trends and of the spectra of the output signals $y(k)$ with the signals estimated by the NN ($\hat{y}_{NN}(k)$) and the WN ($\hat{y}_{WN}(k)$) are presented. Whereas the spectra are almost superimposed (see Figure 3.7(b)), in the zoom of the trend in the interval $[0.3 - 0.4]$ s (see Figure 3.7(a)) a time-shift is evident. Both the errors related to the $\{RMSE(\%),\ \Delta_{Width}(\%)\}$ are more sensitive than $\Delta_{Peak}(\%)$ to the process nonlinearity. That explains their greater values respect to the $\Delta_{Peak}(\%)$ whose low error guarantees a satisfactory identification of the slugs mean inter-distance. The NN models were also tested by using the real-data at each iteration ($T = 1$ sample) and a reduction of the $RMSE(\%)$ up to 1% was reached. Choosing a time window of 1 s, the identification process was applied to the 24 experiments. In Figure 3.8, the three plots represent the errors trends $\{RMSE(\%),\ \Delta_{Peak}(\%),\ \Delta_{Width}(\%)\}$ per experiment (versus AF) both considering the NN and WN models. Similarly to the three experiments already investigated, the errors are less than $\{50\%; 10\%; 15\%\}$ respectively for $\{RMSE(\%),\ \Delta_{Peak}(\%),\ \Delta_{Width}(\%)\}$, and no significant difference can be detected

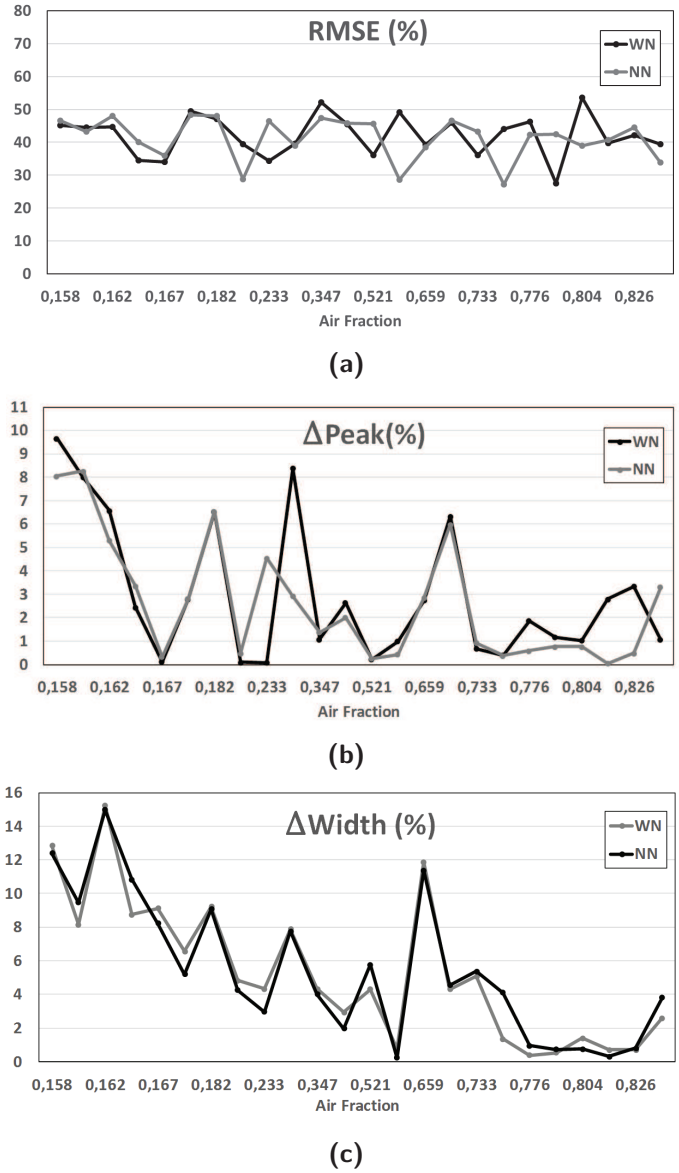

Fig. 3.8. Three plots for the trends of (a)$RMSE(\%)$, (b) $\Delta_{Peak}(\%)$, (c) $\Delta_{Width}(\%)$, per experiment versus AF both considering NN (grey line) and WN (black line) models. For an easy reading of the AF values on the x-axis, those values are graduated as samples not taking in to account their linear distribution.

between the two classes of models. The value of $\Delta_{Peak}(\%)$ less than 10% guarantees the identification of the mean slug inter-distance for all experimental conditions, so the possibility to detect the mean slugs velocity, but to face the problem of the phase-shift is necessary to reach the slug tracking. On this purpose in the

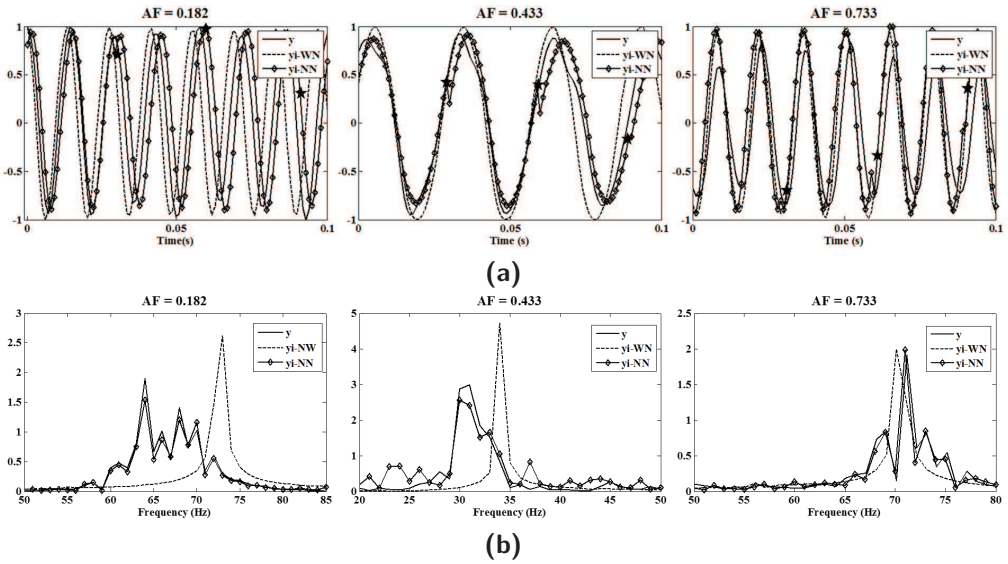

Fig. 3.9. The comparison among (a) the trends starting from the same initial conditions and (b) the spectra of the signal $y(k)$ (solid line), with the signals estimated by the NN ($\hat{y}_{NN}(k)$, dotted line) and the WN ($\hat{y}_{WN}(k)$, dashed line) in a time-windows of 0.1 s.

test phase using the NN models the variables $\hat{y}_{NN}(k)$ has been computed using the real-data after a number of iterations varying in the range $T = [1, 100]$. The optimal trade-off, to avoid the time-shift due to the error propagation, and to maintain the models autonomy from the real-data was reached for $T = 30$.

In Figure 3.9(a), as to Figure 3.7(a), for the experiments $AF \in \{0.182; 0.433; 0.733\}$ the comparison among the trends of the signals $\{y(k), \hat{y}_{NN}(k),\ \hat{y}_{WN}(k)\}$ are plotted in a time interval of 0.1 s (equivalent to 100 iterations). The models to obtain $\{\hat{y}_{NN}(k),\ \hat{y}_{WN}(k)\}$ were feed with the real data for the first two-time iterations $k = \{1, 2\}$.

Using the wavelet models is possible a satisfactory autonomous tracking for 0.1 s, then the loose in the synchronization between model and the real data become significant, no feeding for the correction is possible with these models. Thus, confirming the robustness of these models in slugs tracking for small time-intervals autonomously.

Using the neural networks models, the dynamical evolution of $\hat{y}_{NN}(k)$ was computed feeding the models with real-data periodically each $T = 30$ iterations, see the marker in the $\hat{y}_{NN}(k)$ trends of Figure 3.9(a). This procedure reduces drasti-

cally the time shift visible in Figure 3.7(a). Within 30 iterations, the model tracks autonomously the passage three slugs for fast flows $AF \in \{0.182; 0.733\}$ and one in the slow flow $AF = 0.433$. Whereas, the periodical real-data feeding produces a successful tracking also in long-time evolution. The improvement in the identification is confirmed, also, by the spectra comparison in Figure 3.9(b). In particular, the spectra of the signals identified by NN, $\hat{y}_{NN}(k)$, is perfectly superimposed with the $y(k)$ spectra for all the experiments. That underlines the capability of the NN model to identify the nonlinear effects in the slug passage, otherwise by the WN models only the mean of the frequency slug passage is detected as shown in the spectra of $\hat{y}_{WN}(k)$.

3.4.2 Tracking by Multi-Pattern

To study the possibility to have a single model in the case of input flow rate variations, the *Multi-Pattern* pattern were considered.
By using the WN identification procedure for a pattern composed by three experiments, the optimal number of nonlinearity units of the estimator was set to $nodes = 40$.
Starting from this value, both NN and WN models were tested for all the three sets $\{Set-1;\ Set-2;\ Set-3\}$ searching the minimum number of neurons that ensures the correct signals identification. A one-hidden layer topology with 40 nonlinear units proved to have good performance also in the case $Set-3$ including seven experiments. For all the three sets $\{Set-1;\ Set-2;\ Set-3\}$ the error bar histograms related to the performance of the three NN and WN models ($\{RMSE(\%),\ \Delta_{Peak}(\%),\ \Delta_{Width}(\%)\}$) are plotted in Figure 3.10. In the test phase no real-data was used to obtain $\{\hat{y}_{NN}(k),\ \hat{y}_{WN}(k)\}$ with the exception of the first two iterations ($k = 1, 2$).

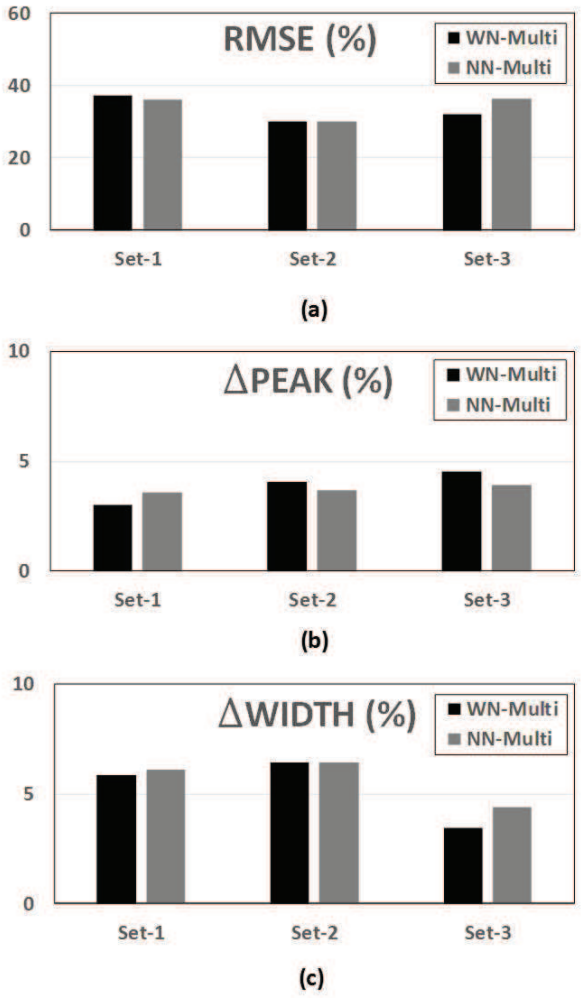

Fig. 3.10. Performance indices for the three sets $\{Set-1;\ Set-2;\ Set-3\}$ the error bar histograms related to the performance of the NN and WN models evaluated by the error indices: (a) $RMSE(\%)$; (b) $\Delta_{Peak}(\%)$; (c) $\Delta_{Width}(\%)$.

The performance of the two classes of models are quite equivalent maintaining the same error level as in the *Single-Pattern* case $\{50\%; 10\%; 15\%\}$.
For $Set-2$, the comparisons of spectra $\{y(k),\ \hat{y}_{WN}(k)\}$ and $\{y(k),\ \hat{y}_{NN}(k)\}$ are respectively in the Figure 3.11(a) and (b). The superimposition of the spectra confirms the enhancement of the *Multi-Pattern* identification procedure to capture the system nonlinearity. Finally, in Table 3.2 the peaks detected in the spectra (ω_p) of the estimated signals for $\{Set-1;\ Set-1;\ Set-1\}$ are compared among each other and with the expected values computed per single experiment. A satisfactory

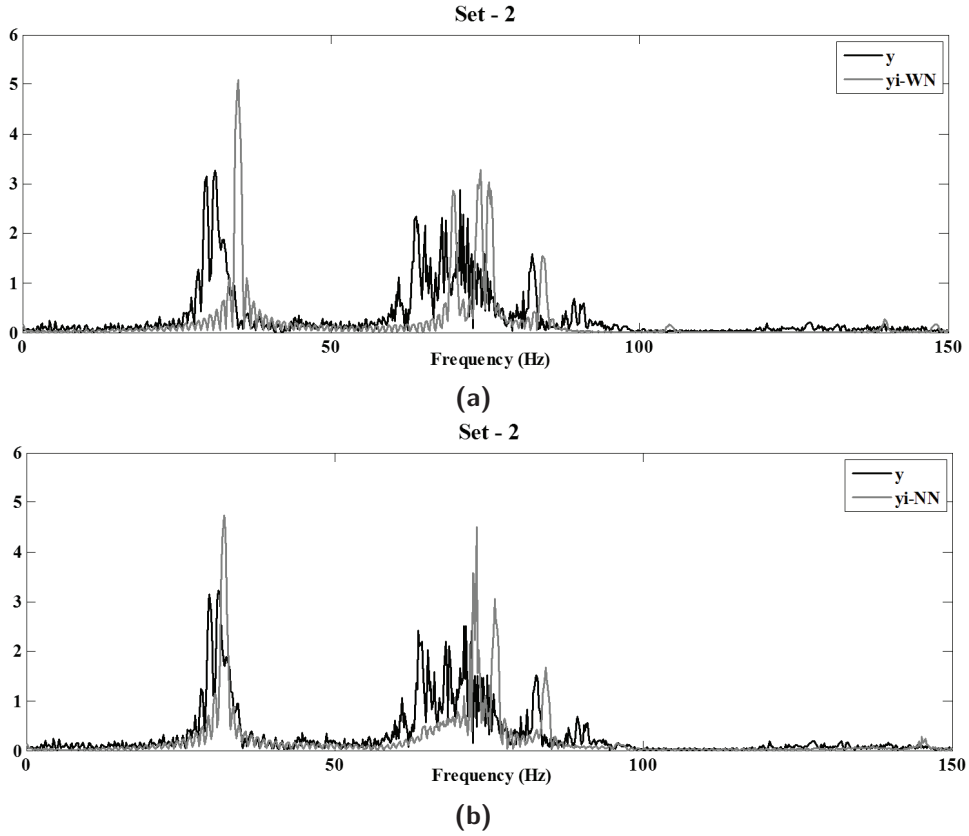

Fig. 3.11. For Set_2, the comparisons of the spectra (a) $\{y(k),\ \hat{y}_{WN}(k)\}$ and (b) $\{y(k),\ \hat{y}_{NN}(k)\}$.

agreement was obtained.

That confirms the possibility to use one model for the identification of the mean slug inter-distance in different experimental conditions. Additionally, to obtain the slugs tracking, showing this model the same sensitivity to the process nonlinearity by means of the indexes $\{RMSE(\%),\ \Delta_{Width}(\%)\}$ as in the case study of *Single-Pattern*, a procedure based on real-data feeding after T iterations could be applied.

In conclusion, the data-driven modelling has been proposed to identify the dynamics of fast two-phase flows in microchannels.

The two classes of NARX models implemented by neural networks and wavelet networks were investigated. The identification process was applied to the single experiment (*Single-Pattern*), and collecting up to seven experiments together (*Multi-Pattern*). The performance of the identified models were evaluated both

in time and in frequency domain by the introduction of parameters for the flow velocity characterization.

For the identification of the slug flows velocity, assumed as the mean of the slugs inter-distance, both NN and WN models show satisfactory performance. This result is confirmed in the case of *Single-Pattern* and *Multi-Pattern*, opening to the use of the model also in the case of varying input flow rates.

The slugs tracking being more sensitive to the process nonlinearity required a study on the *pro and cons* of the two models implementation. Indeed, the value to test both WN and NN models is associated to the advantage to have a model in a closed-form respect to an open-form. The WN closed-form model is autonomous from the real-data but suffers from the error propagation, so in the slug tracking for long time-interval a significant phase shift can be produced. Conversely, the NN models can give good performance autonomously from real-data for smaller time-interval but, being in an open-form, can be used for very long time-interval by feeding the model with real-data repetitively after a certain number of iterations. Based on the process needs both modelling techniques could be implemented satisfactory.

These results represent an important step toward the development of predictive controls for SoC applications taking the advantages of the simplicity in the optical technology used for the process detection, and of the models developed for both the flow velocity identification and the slugs tracking.

Chapter 4

Real-time slug flows control

4.1 Experimental campaign

The setup considered is described in Chapter 1 and it is labeled as $setup - 2$. The serpentine micro-channel $G3$ ($w = 640\ \mu m$, $l = 121\ mm$) was used (see Figure 1.4). The process was monitored at the center of straight part, tagged as point B in the figure. The signals acquired from the photodiodes were filtered, as described in detail in paragraph 1.2. The sampling frequency of the data acquisition board was set to 2 kHz.
The two input flow rates were set equal ($V = V_{air} = V_{water}$) in the range $[0.3, 0.9]$ ml/min with a step of 0.2 ml/min and in the range $[1, 4]$ ml/min with a step 0.25 ml/min. A total of 18 experiments repeated three times were analyzed, each lasted 60 s. The Air Fraction (AF) is 0.5. All the experiments are summarized in the Table 4.1. In Figure 4.1 and Figure 4.2, a zoom of the filtered signals in time and in frequency domain, respectively, for $V = 0.3\ ml/min$ and $V = 3.75\ ml/min$. It is possible to notice that, increasing the flow rate the trend of the signal changes; in particular, the signal in Figure 4.1 has a square shape and it represents a slow flow dynamic; while in Figure 4.2 the fast dynamic is shown and its signal can be associated to an oscillating behavior. Moreover, it is possible to notice that the peak in the spectra is positioned at higher frequencies in experiment with $V = 3.75\ ml/min$ respect to the one with $V = 0.3\ ml/min$.

Tab. 4.1. Experimental campaign: Flow rate (ml/min) and Frequency peak (Hz). The Air Fraction (AF) is 0.5.

Flow rate [ml/min]	0.3	0.5	0.7	0.9	1.0	1.25
Frequency [Hz]	0.55	2.99	6.85	7.43	9.16	12.01
Flow rate [ml/min]	1.5	1.75	2.0	2.25	2.5	2.75
Frequency [Hz]	15.66	18.03	17.94	26.40	26.40	33.63
Flow rate [ml/min]	3.0	3.25	3.5	3.75	4.0	
Frequency [Hz]	30.84	36.34	29.46	37.32	47.81	

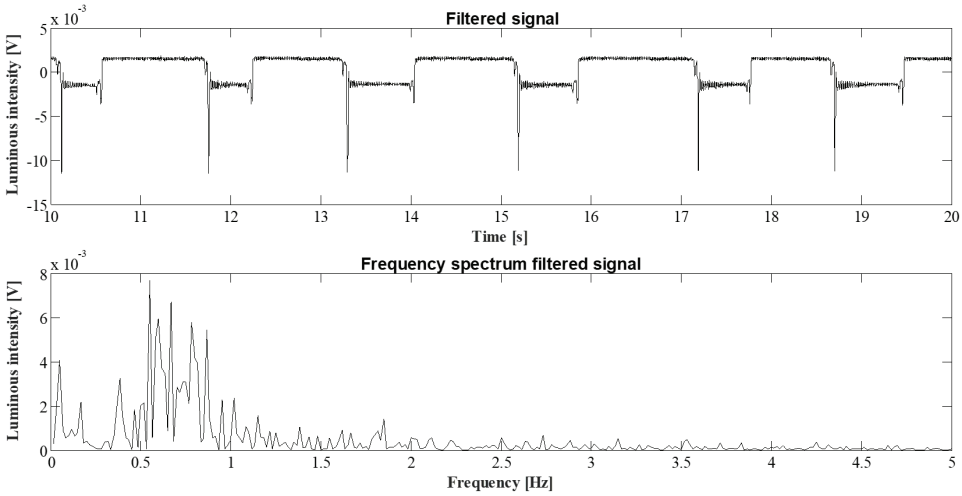

Fig. 4.1. Filtered signal and spectra of experiment with $V = 0.3\ ml/min$.

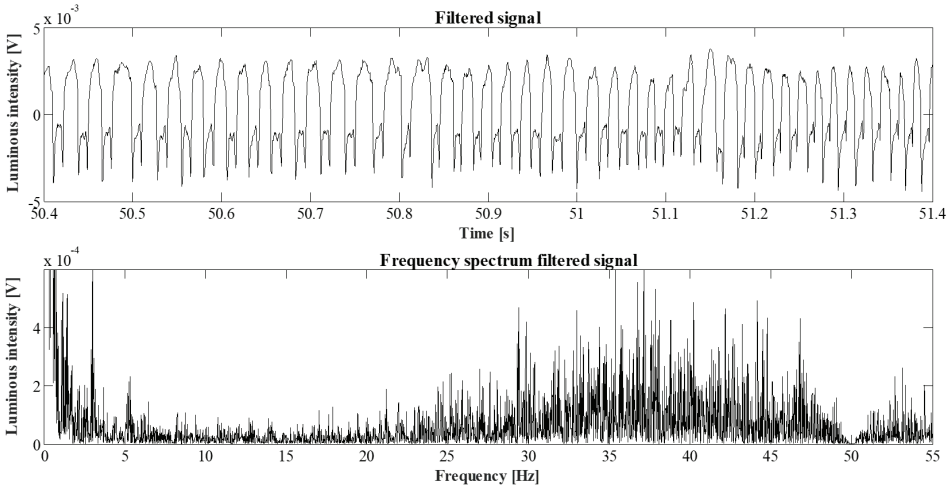

Fig. 4.2. Filtered signal and spectra of experiment with $V = 3.75\ ml/min$.

Tab. 4.2. Transitory time

Initial flow rate [ml/min]	**Final flow rate [ml/min]**	**Transitory time [s]**
0	4	30
4	0	70
0	2	110
2	0	50
0	0.1	>400
0.1	0	30
0.1	0.3	60
0.3	0.1	40
1	1.5	70
1.5	1	40

The active control of the slug flow is based on the on-line signal processing approach. Starting from the optical signal monitoring, an analysis procedure for the flow characterization in frequency domain was developed. The parameter extracted from the characterization phase was used as control parameter. To correctly design the active control system, it is important to evaluate the transitory time that the process takes to move from one dynamic to another. The table Table 4.2 shows the transitory time computed for several conditions. When the flow starts, the time to reach the regime flow increases as the flow rate decreases; while stopping the stream, the time taken so that in the micro-channel there is no more movement decreases as the flow rate decreases. Moving from a lower to an higher flow rate, the transition time is always bigger than moving from a higher to a lower flow rate. Taking into account these considerations, the average transitory time was set to be 50 s.

A procedure in the frequency domain was developed and the peak detected. Starting from the spectrum of the signals, as described in detail in paragraph 1.4, its profile was approximated with a Gaussian model to extract the maximum in the spectrum, reported in Table 4.1 for each experiment considered. In Figure 4.3, the peaks computed by the Gaussian fitting (black solid line) are plotted and compared with the maximum spectrum peaks of the signals acquired by the two photodiodes (black dashed lined and gray solid line). It is possible to notice that, the three trends are quite similar, specially at low frequency ($freq \leq 1\ Hz$), therefore the Gaussian peaks can be used as slugs flow control parameter.

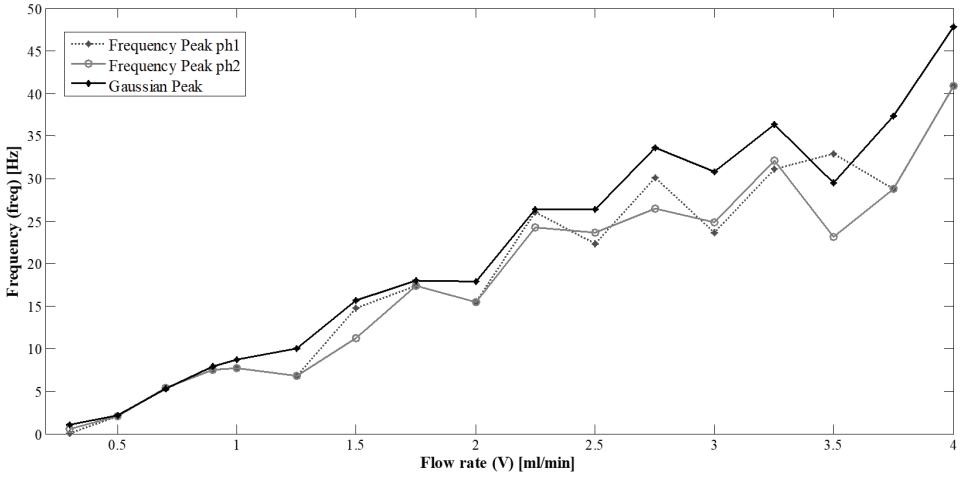

Fig. 4.3. Comparison between the peaks computed by the Gaussian fitting (black solid line) and the maximum spectrum peaks of the signals acquired by the two photodiodes (black dashed lined and gray solid line).

4.2 Control law definition

Based on the system theory definition, the microfluidic two-phase processes can be considered in the class of the two inputs and single output nonlinear dynamical systems where the inputs are the air and water input flow rates and the output is related to the type of flow regime (slow or fast) and the slug/air length or the inter-distance between slugs. Considering as control parameter the frequency peak ($freq$), it is possible to design a control system in order to impose a dynamics to the system in terms of desired slug frequency. Specifically, the open loop and closed loop control systems were defined.

In the Figure 4.4, the peaks detected per experiment ($freq$) are plotted in function of the manipulation variable (V). Two zones are distinguishable: the zone-1 (in the range of flow rate $[0.3 - 2.75]$ ml/min and frequency $[0.55 - 30.0]$ Hz), that shows a regular behaviour and a more irregular part, named zone-2 (in the range of flow rate $[3.0 - 4.0]$ ml/min and frequency $[30.0 - 47.0]$ Hz). For this reason, it was decided to limit the implementation of the control law to the zone- 1.

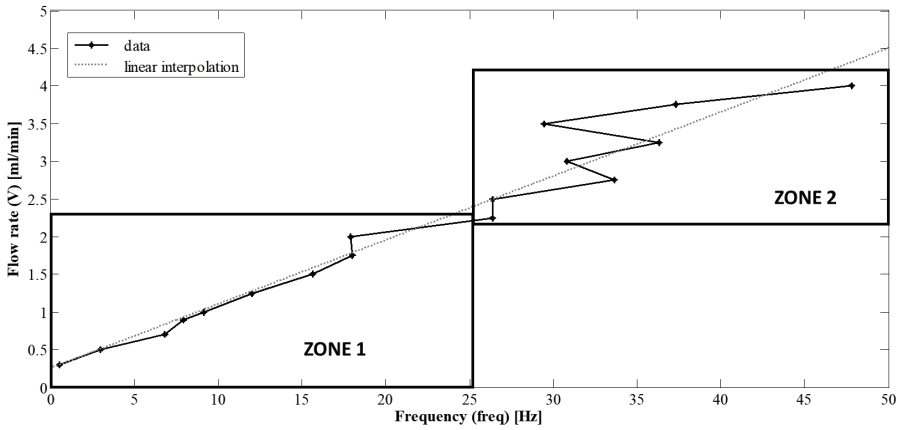

Fig. 4.4. The peaks detected per experiment ($freq$) are plotted in function of the manipulation variable (V). Two zones are distinguishable: the zone-1, that shows a regular behaviour and, a more irregular part, named zone-2.

4.2.1 Open loop

The general equation of the linear fitting can be formalized by the eq. 4.1:

$$V = m \cdot freq + n \tag{4.1}$$

where the manipulation variables of the control system are the two input flow rates ($V = V_{air} = V_{water}$) that allow to reach the desired dynamics.
The Figure 4.5 shows the schematic of the open loop control system for the microfluidic process (Σ): the frequency parameter ($freq_{des}$) is associated to a desired flow behaviour and ($freq_{act}$) is its actual value computed by the signal analysis procedure represented by the soft sensors. Given the eq. 4.1 and the desired control parameter, it is possible to compute the new input flow rate ($V = V_{air} = V_{water}$) to be imposed to the system inputs. The ideal condition is verified when $freq_{des} = freq_{act}$.

4.2.2 Closed loop

The closed loop control scheme is schematized in the Figure 4.6. In this control strategy, the control parameter ($\Delta freq$) is the error between the desired condition ($freq_{des}$) and the actual ($freq_{act}$). The possible control action is related to the

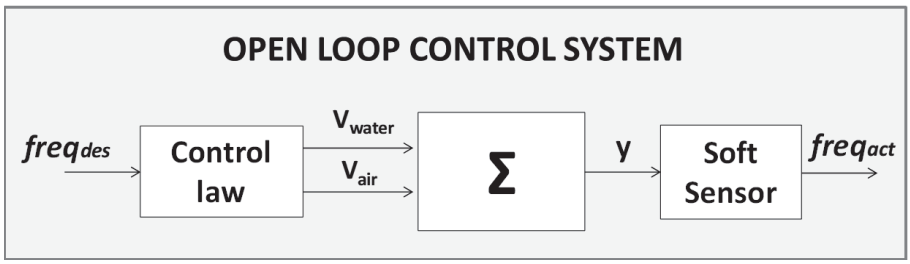

Fig. 4.5. Open loop control scheme.

tuning of the input flow rates ($V = V_{air} = V_{water}$), in a way to have the desired dynamics at the output of the system. For the tuning, the new value of flow rate is increased or decreased of a quantity (ΔV) respect to the actual value, depending on the linear control law considered.

After that the control law defines the first input flow rates to start the process, if the absolute value of the control parameter ($\Delta freq$) is greater than a threshold ($|\Delta freq| \geq Th_{MAX}$), the flow rate will not be updated because it is considered, in the specific control system defined, to be in a dynamic transient phase.

Meanwhile, if the absolute value of the control parameter ($\Delta freq$) is lower than a threshold ($|\Delta freq| < Th_{MIN}$), the microfluific process can be considered in a steady-state phase. The two thresholds (Th_{MAX}, Th_{MIN}) were defined experimentally.

The Figure 4.7(a) schematizes the control strategy implemented, where the input flow rates can be varied linearly taking into account the control law, while in the

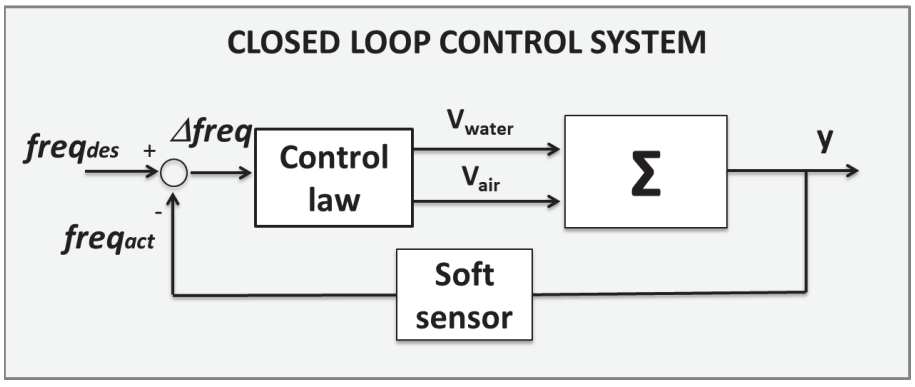

Fig. 4.6. Closed loop control scheme.

other cases the system can be in a transient or in a steady-state phase. The ideal condition to be achieved is $freq_{des} = freq_{act}$. The equations relative to the closed loop control are the following:

$$V_{des} = m \cdot freq_{des} + n \tag{4.2}$$

$$V_{act} = m \cdot freq_{act} + n \tag{4.3}$$

$$TRANSITORY: \quad if\ |\Delta freq| \geq Th_{MAX}; \tag{4.4}$$

$$STEADY - STATE: \quad elseif\ |\Delta freq| \leq Th_{MIN}; \tag{4.5}$$

$$FLOW\ RATE\ UPDATE: \quad else\ |\Delta V| = V_{des} - V_{act} \tag{4.6}$$

$$V = V + \Delta V \tag{4.7}$$

The open loop and the closed control systems designed were implemented in Labview. To validate the method proposed a subset of experiments in the zone-1 was considered, in particular the range of flow rate $[0.3 - 1.25]\ ml/min$ and frequency $[0.55 - 12.0]\ Hz$, represented in the Figure 4.7(b) (black line) with its linear interpolation (dashed line). The parameters of the eq. 4.1 were, in this case, $m = 0.082$ $n = 0.24$.

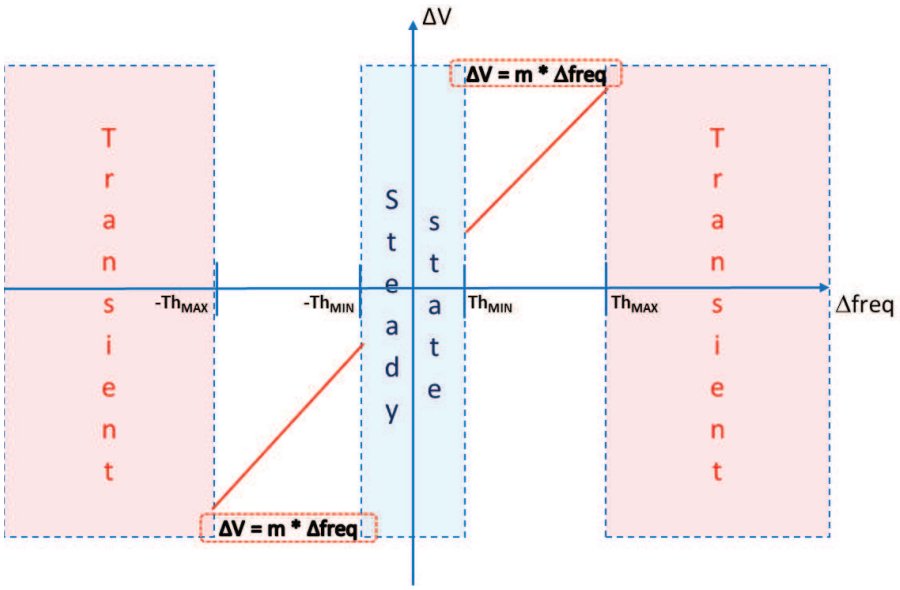

(a)

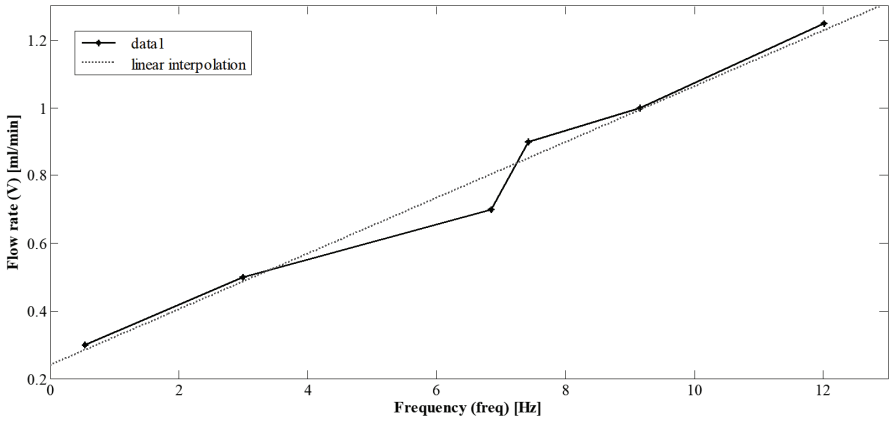

(b)

Fig. 4.7. (a) Scheme of the control strategy implemented, (b) a zoom of the linear interpolation between the manipulation variable (V) and the control parameter ($freq$).

4.3 Labview open loop implementation and results

The open loop Labview platform includes four modules: one to manage the communication between the PC and the syringe pumps, the second to manage the

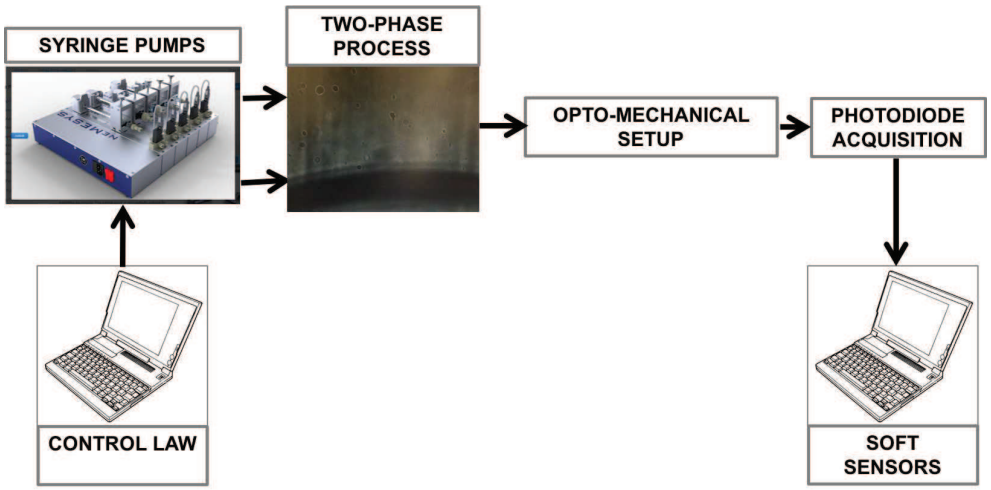

Fig. 4.8. Open loop control flow chart.

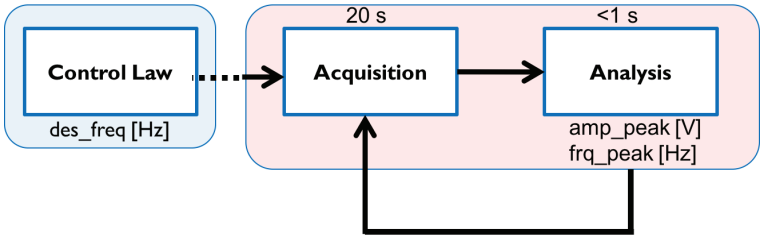

Fig. 4.9. Open loop control Labview algorithm.

signals acquisition from the photodiodes, the third to implement the soft-sensor for the analysis and the last to implement the control law. A flow chart of the open control loop is shown in Figure 4.8.

The Figure 4.9 represents the schematization of the algorithm realized in Labview where the input parameters of each part are specified; in the specific case of the open loop control are: the desired frequency to be set ($freq_{des}$) and the amplitude and the frequency ($amp\_peak, freq\_peak$) of the peak in the signal spectrum in the analysis step.

In the Figure 4.10 and Figure 4.11 are shown the implementation of the control law in the Labview platform, that allows to select and properly set the air and water flow rate ($V = V_{air} = V_{water}$). The flow value chosen is sent to the module that manage the communication with the syringe pumps.

First, the user selects the desired frequency ($freq_{des}$) and the process is initialized

imposing the correspondent flow rates ($V = V_{air} = V_{water}$) computed by using the control law in eq. 4.1. After the transitory time, defined in the section 4.1, the acquisition phase and then the analysis phase are started.
The acquisition is related to the number of samples to be read, and this value was properly set in the "DAQ assistant" block in order to monitor and analyze the process every 20 s. The analysis block is characterized by a low-pass filter whose cut-off frequency was set to be $f_c = 45\ Hz$, that allows to remove the noise of the power supply and that related to external lighting. Moreover, a band-stop filter was also used to remove the continuous frequency component and therefore it is possible to evaluate the maximum peak in the spectrum of the processed signal ($freq_{act}$).
During the control process, it is possible to monitor the raw and filtered signals and their relative frequency spectrum through the Labview GUI. The system also provides for saving the entire raw and filtered signals.

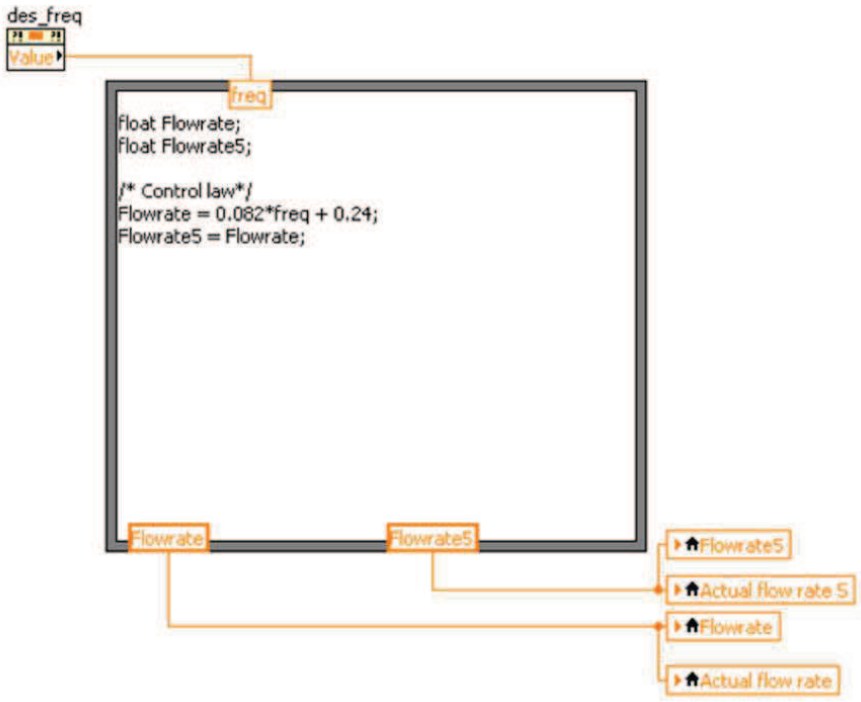

Fig. 4.10. Labview control law for open loop control scheme.

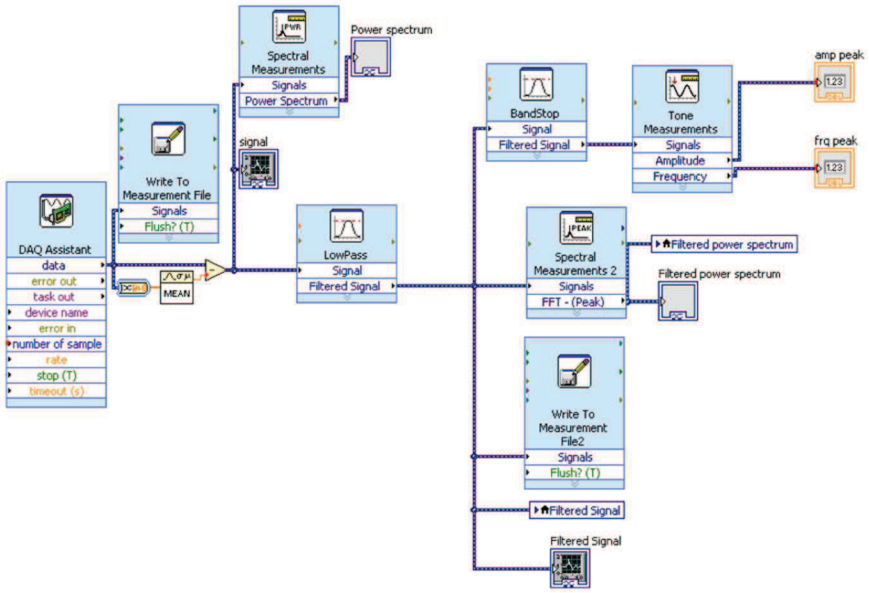

Fig. 4.11. Labview acquisition and analysis for open loop control.

In the GUI of the Labview platform reported Figure 4.12, it is possible to distinguish: the section related to the pumps control, the section to view the raw signal and the filtered signal in real-time and the control section. In the latter section, it is possible to set the frequency of the desired slugs flow ($freq_{des}$) and to read its actual value computed by the signal analysis procedure ($freq_{act}$). The desired frequency value is used to automatically set the syringe pump flow rate through the control law. The slugs flow in the microchannel is checked each 20 s by the soft-sensor implemented to control any variations on the flow velocity.

In Figure 4.13, it is reported a real-time experiment in which the value of the desired frequency was changed three times $freq_{des} = \{1, 5, 10\}\ Hz$. On the top of the figure is reported the filtered signal, on the bottom its spectrum in order to evaluate the global behaviour of the experiment. It can therefore be seen that the spectrum shows peaks just in correspondence with the areas near the desired frequencies.

In the Figure 4.14 it is reported on the top of the figure the filtered signal, where the three time windows showing the different dynamics were highlighted and labelled with the values of the desired frequency $freq_{des} = \{1, 5, 10\}\ Hz$.

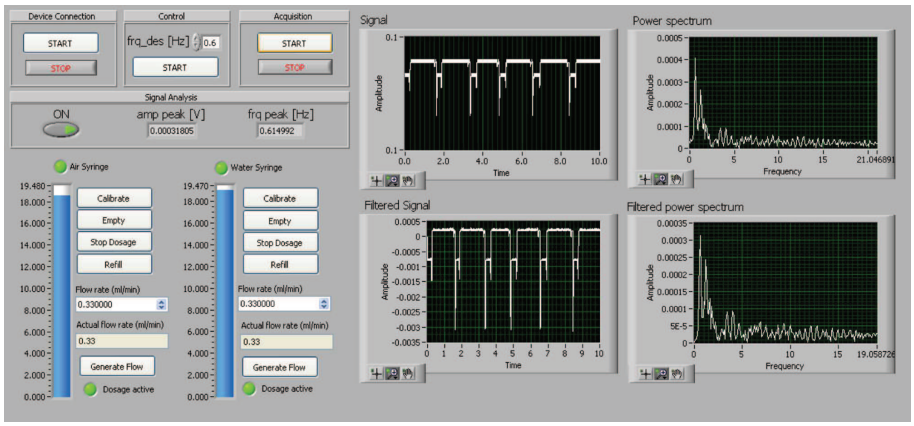

Fig. 4.12. Labview GUI for open loop control scheme.

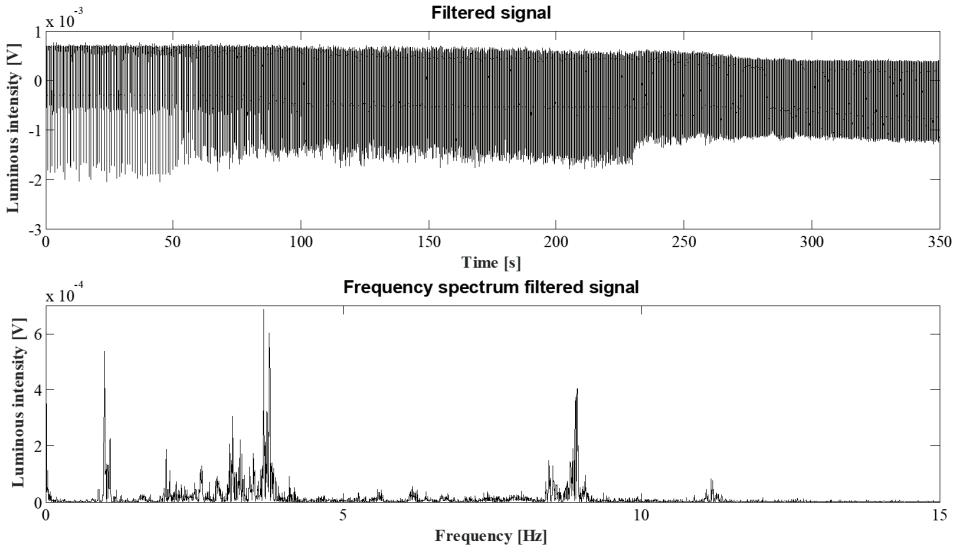

Fig. 4.13. Signal acquired by the open control Labview platform and its spectrum.

The first portion of signal relative to the $freq_{des} = 1\ Hz$ is plotted after the transition phase.

Considering the signal segmented in three parts (each relative to the change of desired frequency) and neglecting the part of the signal relative to the transitory phase, the spectra were computed and plotted (bottom part of Figure 4.14). The detected peaks are $freq_{act} = \{1.12, 3.74, 8.92\}\ Hz$. Since the control is used in the open loop configuration, the results obtained are not extremely precise and

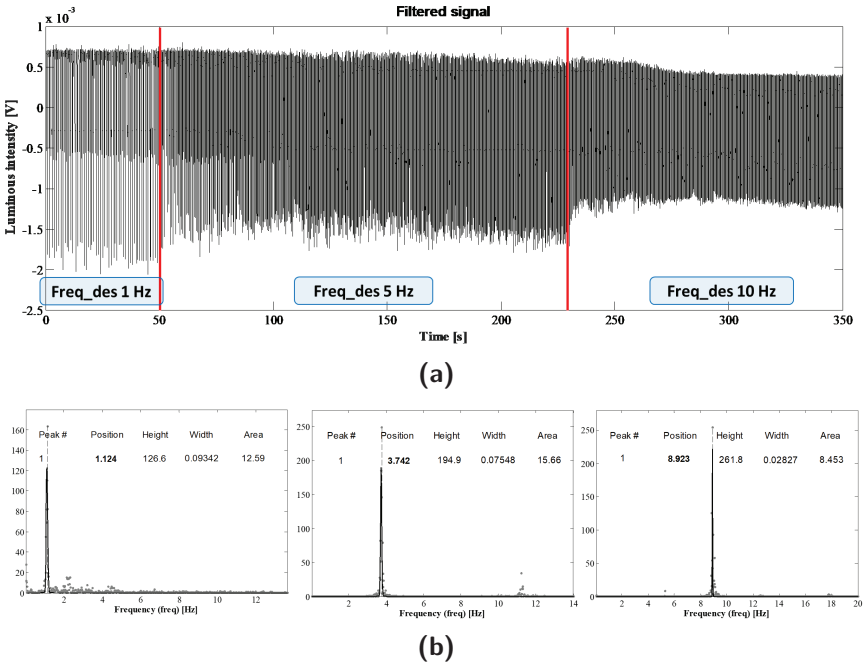

Fig. 4.14. (a) Signal acquired by the open control Labview platform divided in three time windows based on the desired flow rate (V); (b) Spectra (in grey), the gaussian interpolation of the spectra (in black).

therefore a certain error is present ($\Delta freq = freq_{des} - freq_{act}$).

4.4 Labview closed loop implementation and results

The closed loop Labview platform includes the same four modules described for the open loop but in this case there is an additional module whose task is to process the information coming from the analysis phase and then evaluate the appropriate corrections to be given to the air/water flow ($V = V_{air} = V_{water}$) in according with the closed loop control system described.
The flow chart of the closed control loop is shown in Figure 4.15 while the Figure 4.16 represents the scheme of the algorithm realized in Labview where the various input parameters are specified: desired frequency, parameters related to the configuration of DAQ (sampling frequency, number of samples to read and

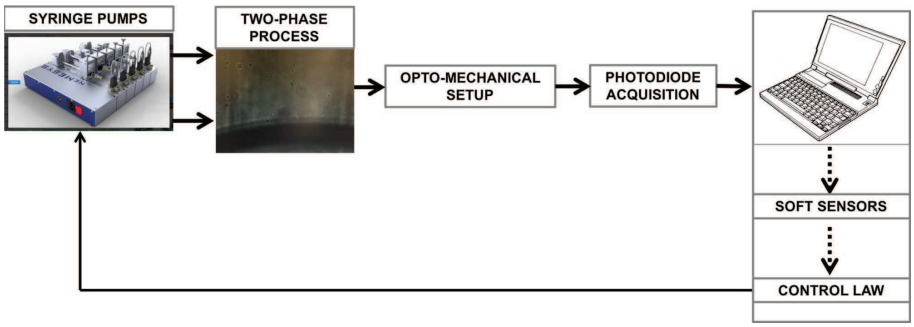

Fig. 4.15. Closed loop control flow chart.

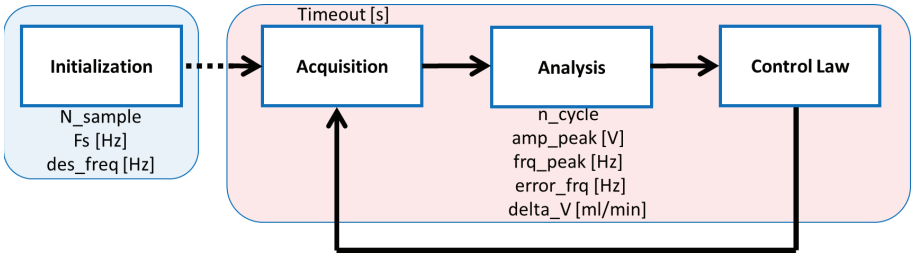

Fig. 4.16. Closed loop control labview algorithm.

timeout) and those related to the analysis phase (number of cycles of the control, amplitude and frequency of the peak in the spectrum, the frequency error and the tuning of the input flow rates (ΔV).

The user selects the desired frequency ($freq_{des}$) and the process is initialized imposing the correspondent flow rates ($V = V_{air} = V_{water}$) computed by using the control law in eq. 4.1. After the transitory time, defined in the section 4.1, the acquisition phase and then the analysis and control phases are started. The blocks that implement the control law, the acquisition and the analysis blocks are the same as those seen for the open loop platform.

The Figure 4.17 and Figure 4.18 show the blocks which implements the controller. This part is essentially constituted by a block "Formula Node" of Labview within the portion of code written in a pseudo-language 'C' is executed, through which the error in frequency is calculated and in function of this updated the flow rates ($V = V_{air} = V_{water}$) according to the closed-loop control scheme.

In particular, if the desired frequency is lower or equal to 1.5 Hz ($freq_{des} \leq 1.5\ Hz$), the two thresholds Th_{MAX} and Th_{MIN} (represented in Figure 4.7), that

limit the transient and the steady-state zones, were set to be $Th_{MAX} = 3\ Hz$ and $Th_{MIN} = 0.1\ Hz$. Whereas, $Th_{MIN} = 0.5\ Hz$. The V_{des} was computed taking into account the $freq_{des}$ and the eq. 4.2. From the signal acquired by the optical system, the $freq_{act}$ was extracted and then the relative V_{act} (eq. 4.3). The difference between the desired and actual frequencies was computed ($\Delta freq = freq_{des} - freq_{act}$) and compared with the thresholds. If the absolute value of $\Delta freq$ is greater than Th_{MAX} (eq. 4.4), the process is in the transitory phase and the flow rate does not need to be updated, instead, if the absolute value of $\Delta freq$ is lower than Th_{MIN} (eq. 4.5), the process is in the steady-state condition and also in this case the flow rate remains the same. In the other condition (eq. 4.6 - eq. 4.7), the difference between the desired and the actual flow rates was computed and added to the flow rate of the syringe pumps.

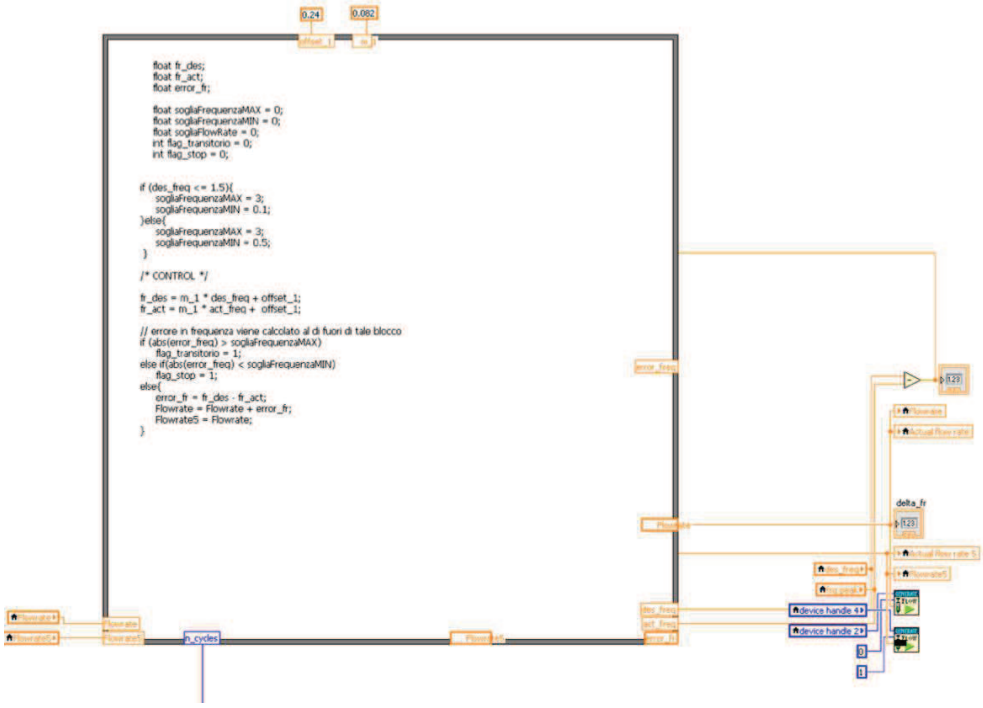

Fig. 4.17. Acquisition and analysis labview implementation for closed loop.

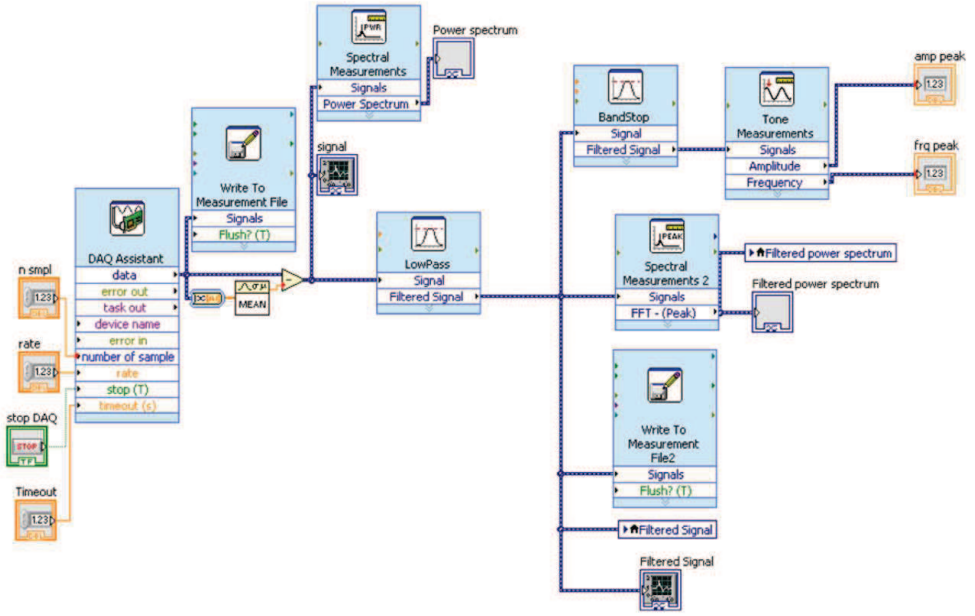

Fig. 4.18. Control labview implementation for closed loop.

In Figure 4.20, it is reported a real-time experiment for the closed loop control implemented in which the value of the desired frequency, as in the open loop control, was changed three times $freq_{des} = \{1, 5, 10\}\ Hz$. In this way it is possible to compare the efficiency of the closed-loop control system implemented by comparing the results obtained with the open-loop one. On the top of the figure is reported the filtered signal, on the the bottom its spectrum in order to evaluate the global behaviour of the experiment. In the Figure 4.21 (a), it is reported on the top the filtered signal, where the three time windows showing the different dynamics were highlighted and labelled with the values of the desired frequency $freq_{des} = \{1, 5, 10\}\ Hz$. In the bottom part (Figure 4.21 (b)) the three spectra evaluated in the temporal window labelled with $\{A, B, C\}$ are plotted. The detected peaks are $freq_{act} = \{0.99, 4.95, 10.33\}\ Hz$ that means a smaller frequency error ($\Delta freq$) respect to the desired and actual frequency than the open loop control condition.

In the Figure 4.22(a) is shown in detail the signal related to the transition from the frequency of 1 Hz to 5 Hz, in a time window of $[160 - 340]\ s$.

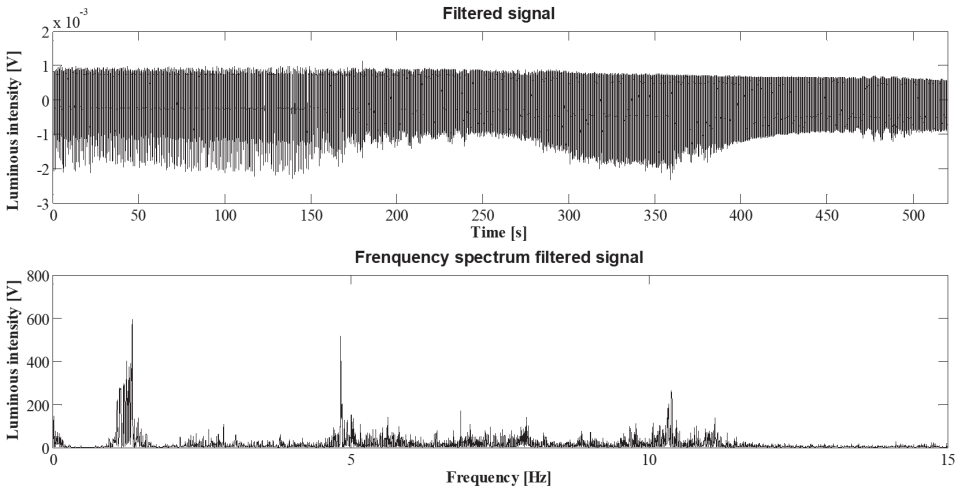

Fig. 4.20. Signal acquired by the closed control Labview platform and its spectrum.

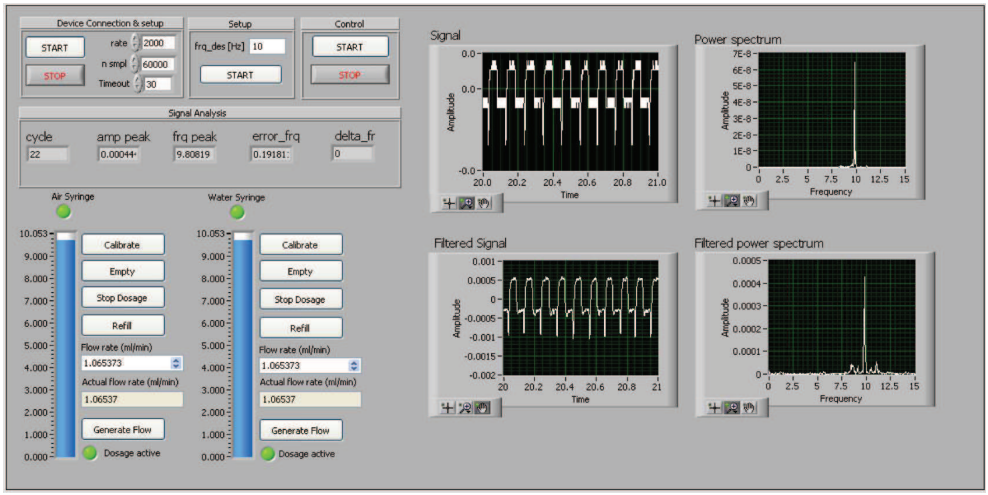

Fig. 4.19. Labview GUI for closed loop control scheme.

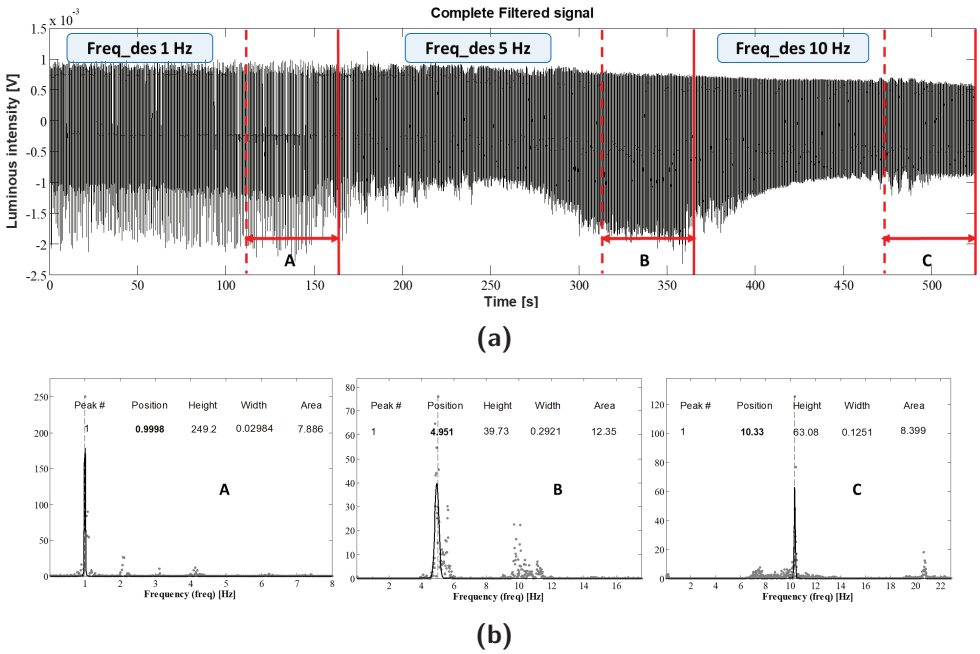

Fig. 4.21. (a) Signal acquired by the closed control Labview platform divided in three time windows based on the desired flow rate (V); (b) Spectra (in grey), the gaussian interpolation of the spectra (in black).

The dashed lines separate three zones of the signal. $B1$ is the transitory part of about 130 s, $B2$ a portion of 40 s of $B1$ and B that is the part considering for as regime state, whose spectrum was evaluated and the peak detected as control parameter. The spectra (in Figure 4.22(b)) revel that in the transient period ($B1$, $B2$) the peaks are not the ones desired instead, in the regime zone, the desired peak was reached.

In the histogram in Figure 4.23, the comparison between the frequency error $\Delta freq$ in the open loop (grey) and closed loop (black) control system: it is considerably lower in the closed scheme with a maximum error of 0.33 Hz when the desired frequency is 10 Hz.

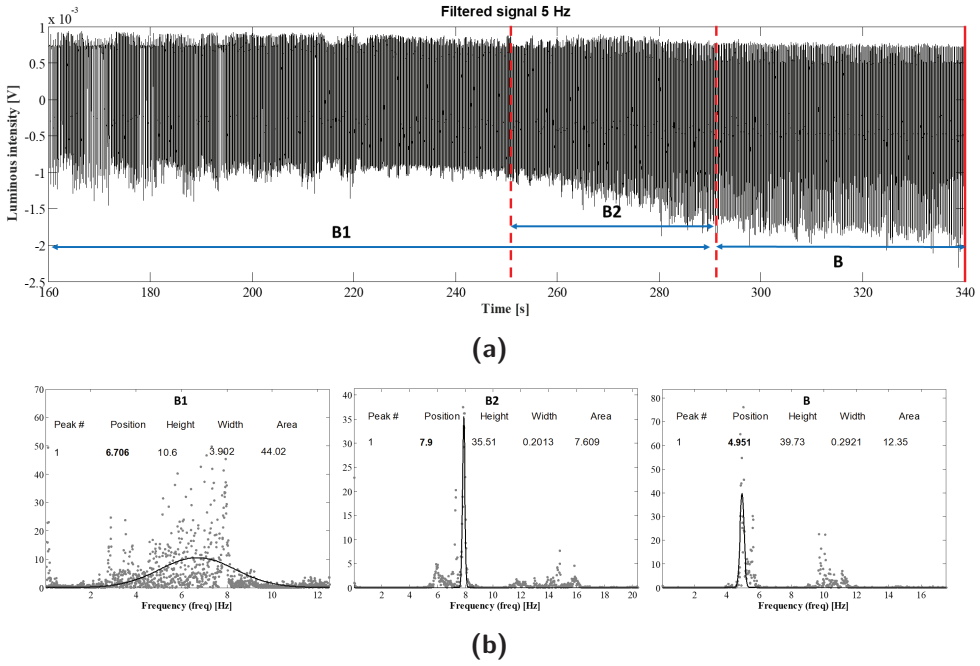

Fig. 4.22. (a) Signal related to the transition from the frequency of $1\ Hz$ to $5\ Hz$, in a time window of $[160 - 340]\ s$; (b) Spectra of transient zones (B1 and B2) and regime zone (B).

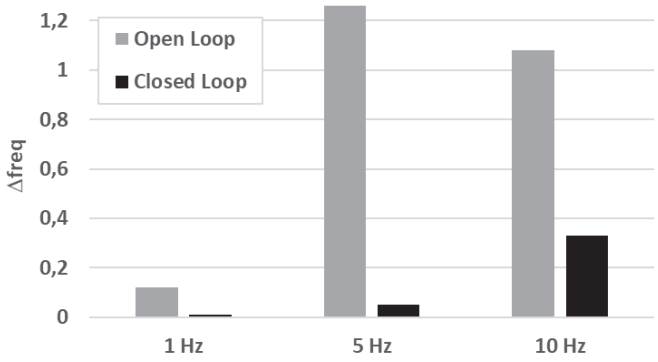

Fig. 4.23. Comparison of frequency error $\Delta freq$ in the open loop (grey) and closed loop (black) control system.

A real-time platform for the control of the slugs flow in micro-channel was implemented. In particular, the closed loop control strategy allows to have a continuous and stable maintenance of the desired flow conditions, simply by imposing the

frequency of slugs. This approach takes the advantages of the optical monitoring and the on-line signal processing.
In comparison with the standard passive and active microfluidic processes control strategies, it can be easily adapted in different experimental contexts and easily adapted for system on-chip control. Starting from this result, in the future works, the attention could be focused on the implementation of a more detailed control strategy in order to manage a wide range of dynamics by considering the jump from a range defined by a specific control law to another one. Moreover, taking into account the complexity of the processes in addition to the linear controller implemented, an integral action could also be considered for the optimal tuning and therefore to reduce the frequency error increasing the performance of the control.

Part II

MICRO-OPTOFLUIDICS DEVICE FOR SLUG FLOWS DETECTION

Introduction

Most of microfluidics applications requires accurate measures and control within the microfluidic channels [11]. Optical techniques were adopted to monitor, sensing and control the processes [12], leading to the research area of the optofluidics that are based on the integration of optics and fluidics [13].
The traditional methods to investigate the flows are based on the acquisition by using a fast CCD camera or a micro-PIV system. Both instrumentation are non-invasive and allow to have detailed and accurate information about the microfluidic process, but with the drawbacks related to costly and bulky equipments. A simplified monitoring setup was obtained by using photo-detectors coupled with micro-optical components [15].
In the fabrication of the micro-optofluidic devices two aspects have a central role: the material with which they are built and their properties, and the fabrication methods. It is important to highlight that these two aspects are strictly correlated, because each fabrication technology protocol can be applied to a specific material [67]. In literature, the most common polymers are the Poly(dimethylsiloxane) (PDMS), the Poly(methyl-methacrylate) (PMMA), and the Cyclic-Olefin Copolymers (COC).
The PDMS based soft-lithography technology [68,69] is probably the most used for the rapid prototyping of the devices. It merge the good resolution of the devices realized with the soft-lithography with the properties of the PDMS: a polymer biocompatible, optically transparent, impermeable to liquids and with high chemical resistance. This method is applied also to the realization of optic components: waveguides [70], micro-mirrors [71] and micro-lenses [72] that can be used for the flow monitoring in vivo [38] and in vitro [36] applications.
Recently, 3D Printing technology offers the possibility to quickly and inexpen-

sively print complex structures channels, by using low-cost equipment. The challenges faced in this part of the work was to extent its use in for the realization of micro-optofluidic devices. The major advantage, beyond the ease of use and the possibility of employing different materials, is the ability to build structures with different heights and more complex network of microchannels [73–76].
In micro-optofluidic devices, it is important to deliver, as closer as possible, the input light to the fluidic process and then, to collect the output signal, but also to steer the direction of the light beam. To do this, in chapter five, we proposed two methods to realize waveguides and mirrors and following in chapter six we present a prototype of the micro-optofluidic flow detector.
The theoretical principle exploits to design the components is the total internal reflection occurring at a boundary between two media, when the incident angle of a source light beam is greater than the critical angle related to the media refractive indexes. The same principle is applied [77] by using an external and more complex optical setup, that involves the light alignment related to the reflection and refraction at several subsequent boundaries. The embedding of the optical fiber insertions in the chip design has allowed a reduction in the number of the interfaces crossed by the light and a satisfactory performance is achieved even without the use of lenses.
The variety of applications related to the use of this class of embedded micro-optofluidic devices is enormous. Two examples based on single single-flow monitoring are described in [78] and [79]. In the first a micro-optofluidic device was used to determine the concentration of lactose in a liquid. In the latter, a variable optical attenuator device is obtained by altering the refractive index of the fluid within the micro-channel.
An innovative aspect highlighted is the use of the 3D Printing as alternative method to realize the master of the device, that is in general realized by the standard soft-lithography. Although 3D printed structures cannot currently compete with the resolution of structures defined using soft-lithography, several advantages can be foreseen such as the simplification in the fabrication of structures with different heights or suspensions and, the diversification of the chip's materials (no longer limited by the 3D printable resins). Thanks to its design flexibility, it would be possible to create channels quickly and inexpensively with unprecedented com-

plexity, as well as integrating micro-optic components.
In chapter five, all the steps related to the realization of micro-waveguides and mirrors were presented and discussed: from the CAD preparation to their optimization by ray-tracing simulations and the micro-optical components experimental test. In chapters six, a method to optimize the realization of micro-optical components is proposed and then they embedded into a micro-optofluidic flow detector. On the device was conducted experimental tests considering different slug flow.

Chapter 5

Micro-optical components

5.1 Fabrication method

The micro-optical components were realized by using the Poly(dimethyl-siloxane) (PDMS) and a low cost technology: the $3D$ printing. The fabrication process consists in the following steps: the design of the CAD of the master, the realization of the master by using the $3D$ printer, the treatment of the master surface and the PDMS system realization.
The CAD of the master was designed in Solidworks and sent to the $3D$ Printer (Object 30). It has a resolution of 49 μm in the work plane and, of 28 μm along the z-axis, that is the direction along which the printhead of the printer moves. The accuracy is around 0.1 mm with slight variations depending on the geometry, the size, the orientation, the material and the post-processing method. Two polymers are used by the printer: the Whiteplus 835 (inspired by ABS) is the main polymer and the FullCure 705 is the support polymer.
As regard the master treatment, in [80] a chemical solution was proposed by using $BASF\ Sokalan\ VA\ 64\ P$, but its use reduces the final quality of the PDMS device. The Sokalan does not allow the perfect and complete reticulation of the PDMS interface between the master and the device, as result its surface has not very precise contours, especially for geometries of the order of μm.
To overcome these disadvantages, a new protocol was developed. The steps are summarized in Figure 5.1. The principal difference respect to the previous pro-

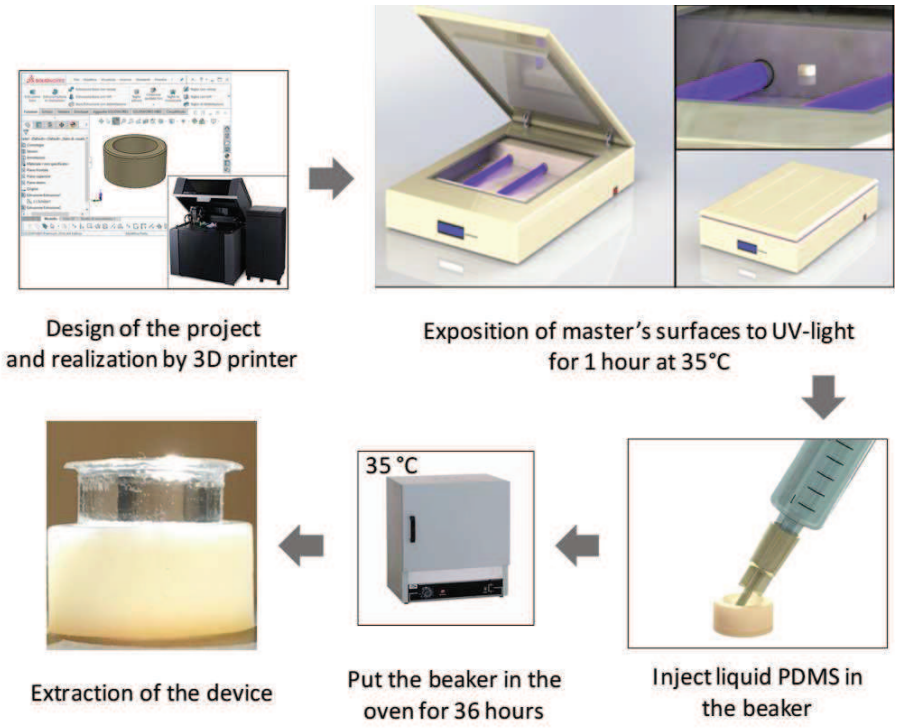

Fig. 5.1. Phases of the protocol presented to realize PDMS micro-systems by *PDMS-3D Printing*. After the Computer Aided Design (CAD) and printing of the master, its surface has to be treated for the PDMS device realization.

tocol consists in the exposition of the surface of the master to the UV light for 1 hour at 35 $°C$.

Generally, the master realized by the $3D$ Printer is obtained by the overlaying of thin layers (about 28 μm) of photo-sensible resin and between one layer and another, the printer lights up the resin with UV rays in order to reticulate it. At the end, it could happen that, microscopically, the master isn't perfectly reticulated and this could compromise the reticulation of the PDMS device. By using the protocol proposed, this problem was overcome. An UV exposition chamber controlled in temperature was realized. The neon tubes used for the UV treatment (Philips UV-A TL-8W G5) has a wavelength of 300 nm and it generates, unavoidably, also an increasing of temperature that, over certain values, can deform the master and, consequently, the PDMS device. A system for the temperature control inside the chamber was implemented by a micro-controller (with Arduino system) and a

temperature sensor.
The two components of PDMS (Sylgard 184 elastomer kit, Dow Corning), the silicone and the curing agent, were mixed together according to the proportion (10 : 1) for the device layer and with a proportion of (5 : 1) for the bulk cover layer. After the degassing procedure to eliminate any air bubbles, the PDMS was poured in the master and placed in oven at 35°C for 36 hours. Finally, the device was extracted from the master.

5.2 Waveguide design

In the design of optical micro-systems, the choice of materials play a fundamental role due the difference in their optical properties as in this context for the reflection indexes. In a waveguide the light travels inside a channel made with a material whose refractive index has to be greater than that of the surrounding material to cause the total reflection phenomena. In this case, the PDMS ($n_1 = 1.41$) waveguides were surrounded by the air ($n_0 = 1$). Another two important aspects for the optimal design of the waveguide are the numerical aperture of the optical fiber (NA, here set to 0.22), used to provide the light at the input, and the air gap between the optical fiber and the waveguide (named d), that causes a change of direction in a certain number of emitted light rays.
From the Snell's law and considering φ_0 ($\varphi_0 = arcsin(NA)$), it was possible to evaluate the angles with which the rays enter in the PDMS micro-waveguide (μWG) (see in Figure 5.2), as follows:

$$\varphi_1^{PDMS} = arcsin(\frac{n_0}{n_1} * sin\varphi) = 8.97^\circ \tag{5.1}$$

To have total reflection inside the waveguide, the rays should have an angle $\alpha > \alpha_{min}$. In particular,

$$\alpha_{min}^{PDMS} = arcsin(\frac{n_0}{n_1} * sin90^\circ) = 45.2^\circ \tag{5.2}$$

and

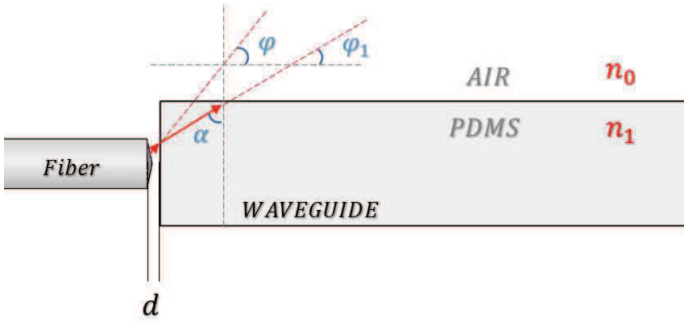

Fig. 5.2. Waveguide design based on the refraction indexes (n_0, n_1, n_2), the fiber optic numerical aperture (NA) and gap between the optical fiber and the waveguide (d).

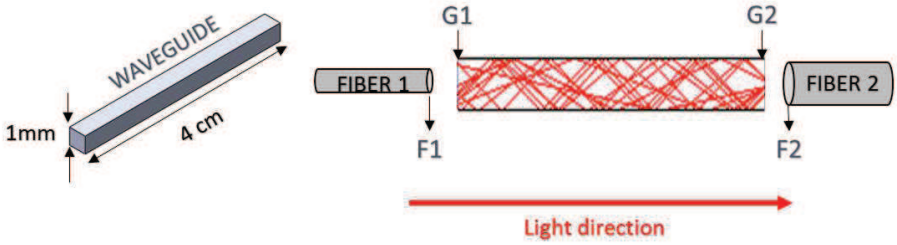

Fig. 5.3. On the left, the geometry of micro-waveguide: squared section of 1 mm side and a length $l = 4$ cm. On the right, A cartoon with a waveguide and the input and output fibers. All the surfaces of interest are labelled as $F1$, $G1$, $G2$ and $F2$.

$$\alpha^{PDMS} = 90° - \varphi_1^{PDMS} = 81.03° > \alpha_{min}^{PDMS} \tag{5.3}$$

Then, theoretically the μWG is expected to have the same behavior of an optical fiber. The waveguide was designed with a squared section of 1 mm side and a length $l = 4$ cm (Figure 5.3). Its performance was evaluated by ray tracing simulations (TracePro by Lamba Research Corporation) using the model in Figure 5.3. Two optical fibers with $NA = 0.22$ were used: one to drive the laser beam toward the waveguide input section ($G1$) and the other to collect the beam at the waveguide output section ($G2$). The distance d was set zero and the simulated input fiber emits 100 rays. The section diameters of the surfaces of the input and output fibers ($F1$ and $F2$) was set respectively of 400 μm and 1 mm.

In Figure 5.4 the radiance maps with the distribution and the percentage of light rays on the surfaces of the fibers and the waveguide are plotted. All maps have

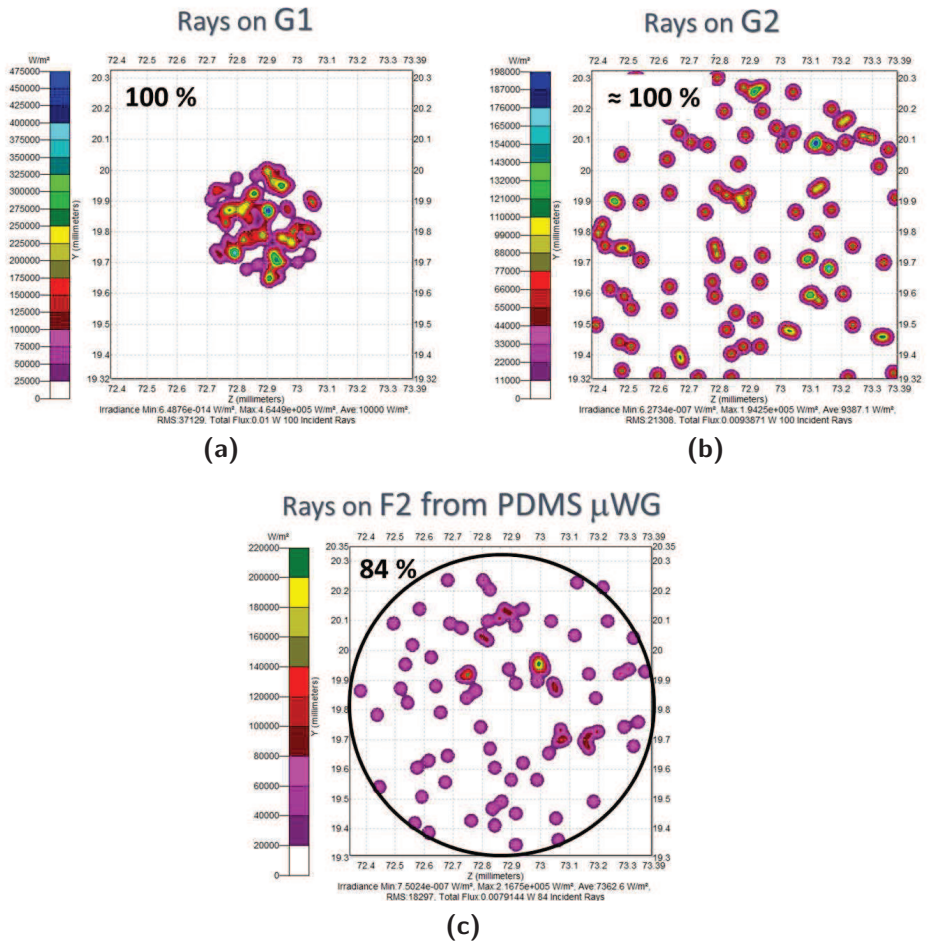

Fig. 5.4. Radiance maps for the distribution and the percentage of light rays on the PDMS μWG surfaces (a) $G1$ (b) $G2$, and on the output fiber $F2$ after the beam passed through (c) the PDMS μWG.

an area of 1 $mm * 1$ mm. The rays distribution in Figure 5.4(a)-(b) are related to the input ($G1$) and the output ($G2$) section of a PDMS μWG. No losses can be detected, that is also related to the choice of use an input fiber diameters half of the μWG diameter.

The rays distribution in Figure 5.4(c) is for the section of the output fiber ($F2$) in the case the beams pass through a PDMS waveguide. The 15% of rays lost. It is important to underline that some rays dispersion can due to the different geometry of the waveguide and fiber section (squared *vs* circular).

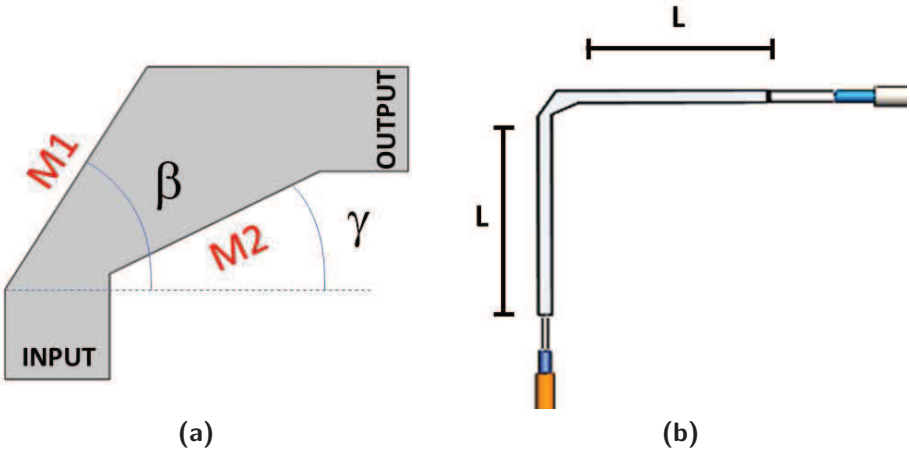

Fig. 5.5. Design of the micro-mirror. (a) Two surfaces $M1$ with an inclination of β, $M2$ is tilted of an angle γ, the extension sides is $L = 0\ cm$; (b) Extension of the sides $L = 2\ cm$.

5.3 Mirror and splitter design

To steer the light beam coming from the input source toward a specific point a mirror was integrated in the design.

The mirror geometry, shown in Figure 5.5 (a), consists in two surfaces $M1$ and $M2$ respectively tilted of an angle β and γ.

Despite of having only one surface inclined of 45°, this design leads to the minimization of the rays dispersion and coveys the beam along the micro-optical device path. The optimal tilt angles ($\{\beta, \gamma\}$) were obtained by ray tracing simulations.

Initially, only one surface $M1$ was considered with the inclination $\beta = 45°$ but most of the rays were dispersed (see Figure 5.6(a)). To improve the performances the angle β was varied and the best result was obtained with $\beta = 57.35°$, as shown in the Fig. **??**(b). At the end, the angle γ was changed (Figure 5.6 (c)) $\{\beta = 57.35°; \gamma = 26°\}$: in this way, $M1$ steers the rays coming from the input and $M2$ compensate any rays that entering in the waveguide would have a tilt angle greater than φ_1^{PDMS}.

The mirror was also simulated considering an extension of the sides of $L = 2\ cm$ (see Figure 5.5 (b)), to have a total length of 4 cm and to be able to compare this result to the performance related to the waveguide. The results, in terms of per-

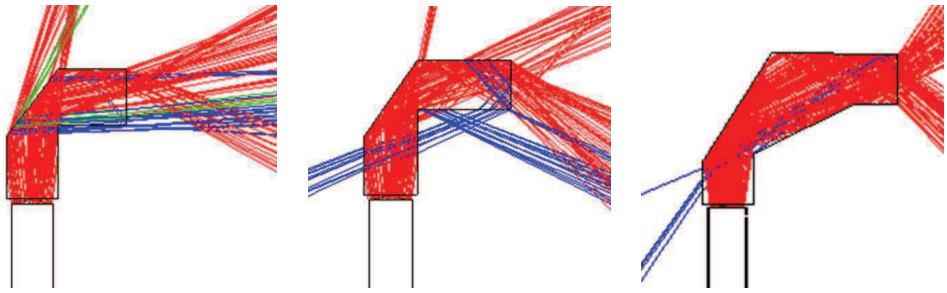

Fig. 5.6. TracePro simulations related to the (a) PDMS mirror with $\{\beta = 45° ; \gamma = 0°\}$; (b) with $\{\beta = 57.35°; \gamma = 0°\}$; (c) with $\{\beta = 57.35°; \gamma = 26°\}$.

centage of rays that reach the output fiber surfaces $F2$, are $\{74; 70\}$ % respectively for two different lengths $L = \{0; 2\}$ cm. Increasing the length L the percentage of output rays decreases, moreover, comparing the percentage of output rays of the waveguide with the mirror with $L = 2$ cm, it is possible to see that about 10% of losses (which add up to those previously evaluated) are due the introduction of the mirror.

An important phenomenon presents at the output of the device is the light splitting in two beams. The geometry designed not only steers all the rays from the input fiber, but it works also like a splitter. Analyzing the principal directions of the two light beams, it is possible to see that they have the same angle of about 36° respect to the line of the waveguide (see Figure 5.7). That suggests to replace, in the follow experimental acquisitions, the single output horizontal fiber with angled fibers, in order to acquire more signal.

5.4 Micro-optical components realization

The establishment of fabrication protocol was not the only issue to face in the micro-waveguide realization. Two aspects were considered. The first was related to a safe procedure to peel the PDMS μWG from the master and the second to create a support structure in a way that it will surrounded by air. In the micro-waveguide realized by Soft-Lithography this problem is not dominant because the smallest section diameter (few 100 μm) minimizes the effects of dispersions even if the micro-device is not surrounded by air [36, 38].

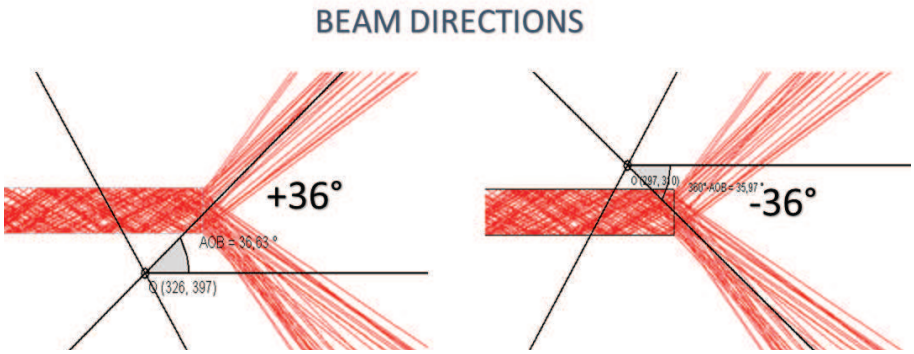

Fig. 5.7. The principal directions of the two output light beams in the mirror components.

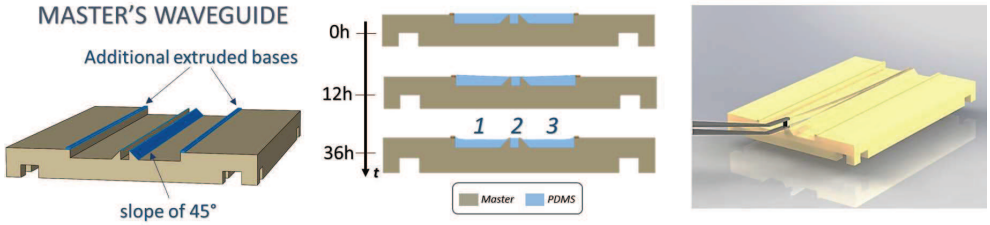

Fig. 5.8. On the left the design of the master for a safe extraction of the PDMS μWG the waveguide; at the center the auto-cutting PDMS phenomena during the PDMS curing; on the right the waveguide extraction.

For a safe peeling of the micro-waveguide, two extruded bases were added each with one wall inclined with a slope of 45° in proximity of the housing of the waveguide. This design has caused an auto-cutting phenomena, indeed the PDMS tends to collapse inside the bases 1 and 3 and the waveguide in the site 2 will result cut as a consequence (as shown in Figure 5.8).

To support the waveguide and make sure that it is surrounded by air, an holder was *3D Printed* produced (see Figure 5.9(a) on the left). The 4 pegs were designed to touch as little as possible the PDMS to minimize the dispersion. Finally, in order to align the input and output fibers, two PDMS frame has been created around the holder with two slots for the fibers insertions. In Figure 5.9(a) at the center it is shown the mounting scheme, and on the right a photo of the complete micro-waveguide system.

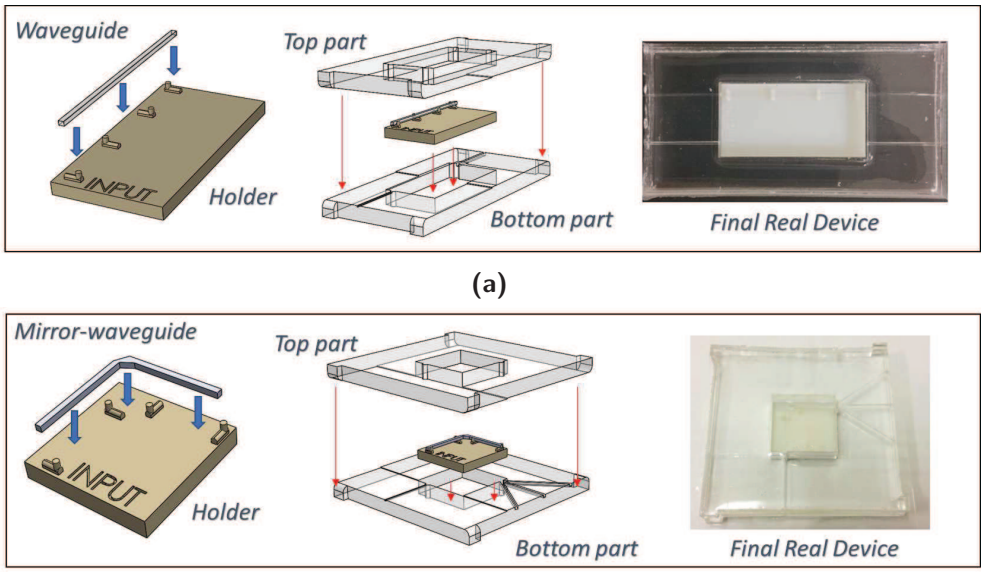

Fig. 5.9. Steps in the realization of the PDMS micro-optical systems:(a) PDMS micro-waveguide and (b) PDMS light splitter. In both charts: on the right the holder designed to support the micro-optical component; at the center mounting scheme of the holder and the top and bottom PDMS layer used for the fibers alignment; on the right a photo of the complete micro-optical system.

The same steps were applied to realize the mirror system. The Figure 5.9(b) shows the mirror and the holder, the bottom and top parts and the final device. The only different respect to the waveguide consists in the number and in the arrangement of the output optical fibers. In fact, as said the previous section, in order to acquire more signal, to the output horizontal fiber were added two angled fibers with an angle of 36°, in the opposite directions, respect to the horizontal waveguide line.

5.5 Micro-optical components characterization

The experimental setup for the micro-optical systems characterization is shown in Figure 5.10. The input light source is a laser system (RGB NovaPro Laser 660 – 125), that generates a light beam with a wavelength of 660 nm and an output power of 10 mW. The output acquisition system consists of a photodiode (PDA100A, Thorlabs) connected with a digital oscilloscope (Siglent SDS1102X). The input

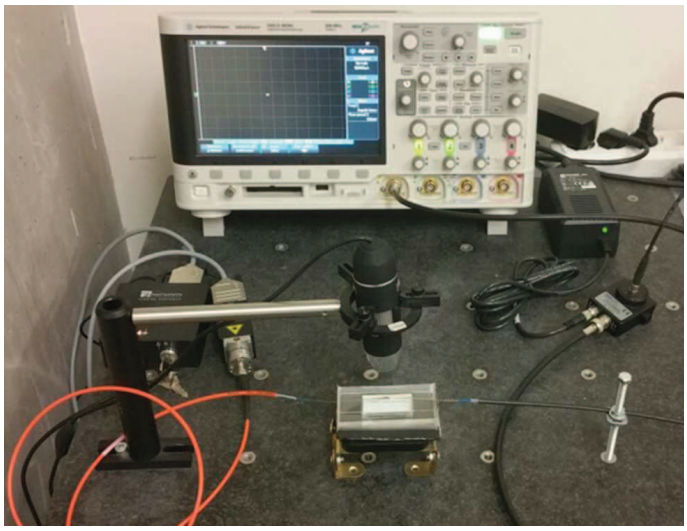

Fig. 5.10. Picture of the laboratory equipment. The laser provides the light input signal to the optical components. It is connected to a multi-mode optical fiber. At the output, the photodiode acquires the light and a digital oscilloscope was used to have the reading.

and output systems are coupled by multi-mode optical fibers with core diameters $\{910 \pm 30, 365 \pm 14\}$ μm and $NA = 0.22$. Three experimental configurations have been considered two for the setup calibration $\{C1,\ C2\}$ and a third for the static characterization of the micro-optical device $\{C3\}$ shown in Figure 5.11 and described as follows:

- condition *C1*: the laser light and the photo-diode were directly connected to the acquisition system by one optical fiber (core 910 μm, SMA to SMA, FG910LEC by Thorlabs);
- condition *C2* two tests were carried out in which the laser light coupled with the optical fiber (both cores were used 365 μm or 910 μm, SMA to free-end) was aligned at a distance of about 100 μm with a second optical fiber (core 910 μm, free-end to SMA) coupled with the acquisition system (see Figure 5.11(b));
- condition *C3* the micro-optical device was aligned in between the input and output systems, the laser light was coupled with the optical fiber of

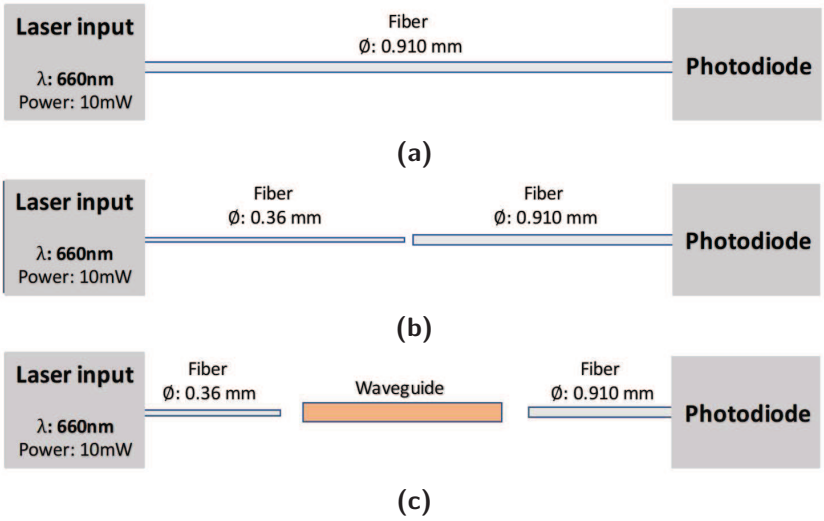

Fig. 5.11. Steps of characterization process for PDMS components. (a) $C1$; (b) $C2$; and (c) $C3$.

365 μm and the acquisition system with the optical fiber of 910 μm (see Figure 5.11(c)).

In the condition *C1* the oscilloscope reading of 10.7 V represents the ideal condition with no causes for light loss was present. In the condition *C2* the oscilloscope reading were 7.1 V with and 6.6 V respectively when the core diameter of the fiber coupled with the laser was 910 μm and 365 μm. The loss was due to the light passage between media at the alignment section. Using at the input and output two optical fibers with the same core diameter (910 μm) the loss increases up to $L_1 = 38.3\%$ with a reading of 6.6 V. A smaller core diameter at the input minimizes the beam dispersion with $L_2 = 33.6\%$ of loss. In the setup for micro-optical devices characterization (condition *C3*) two alignment sections were present, one at the input and the one at the output. The light, coming from the laser coupled with the input fiber (365 μm), passes through the first air gap to reach the waveguide then, at the output of the waveguide, after a second air gap the light is collected by the output fiber (910 μm) for the acquisition. Being the waveguide side section 1 mm, at the input it is expected a loss of $L_2 = 33.6\%$ and at the output $L_1 = 38.3\%$. A total value of $L = 72\%$ of loss leads to an maximum expected acquisition reading for the evaluation of the micro-optical device performance of

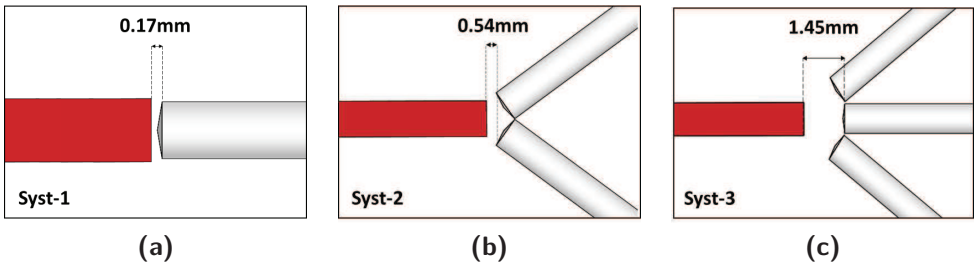

Fig. 5.12. Three different optical fiber arrangements. (a) with one optical fiber placed horizontally respect to the waveguide ($Syst-1$), (b) two optical fibers are tilted, in the opposite direction, of 36° respect to the waveguide ($Syst-2$), and (c) another optical fiber was inserted horizontally ($Syst-3$).

about 3 V.

For the acquisition of the output light in the mirror component system, the phenomena of the light splitting at the output of the system must be taking into account: three different arrangements were be considered (see Figure 5.12).

The first (see Figure 5.12 (a)) uses only an optical fiber (with diameter of 910 μm) placed horizontally respect to the waveguide ($Syst-1$), in the second arrangement (b) two optical fibers are tilted, in the opposite direction, of 36° respect to the waveguide ($Syst-2$), and in the last (c) another optical fiber was inserted horizontally ($Syst-3$). These fiber positions need a specific distance between the waveguide and the output fibers $\{0.17; 0.54; 1.45\}$ mm. In the histogram in Figure 5.13 are reported the results and the comparison for the PDMS mirror acquired in the three conditions explained. Several acquisition on the same system were made and then computed the mean and the standard deviation. The best performance are shown by the acquisition in $Syst-3$, that can be able to acquire the light splitted by the mirror itself.

A PDMS $3D$ printing based technique for producing waveguides and mirrors is presented. In micro-optofluidic devices, it is important to deliver, as closer as possible, the input light to the fluidic process and then, to collect the output signal, but also to steer the direction of the light beam. To do this, a method is proposed to realize waveguides and mirrors that can be integrated in the devices. The theoretical principle exploits to design the components is the total internal reflection occurring at a boundary between two media, when the incident angle of a source light beam is greater than the critical angle related to the media refractive

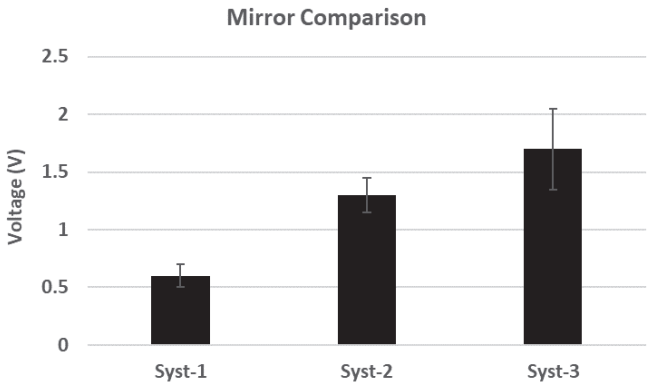

Fig. 5.13. Histogram of result (in V) and comparison for the PDMS mirror acquisition in $Syst-1$, $Syst-2$ and $Syst-3$.

indexes.

The new protocol with the UV-treatment for the post reticulation of the resin produced very high results. The components were individually tested to evaluate and compared the performance, but they can be totally embedded in the micro-optofluidic devices.

The tests on waveguide show losses of about 74% of the entire input signal, the mirror instead in the same experimental conditions presents 84% of losses. The efficiency of the components can be improved by using different material for the holder, as for example an holder made in copper.

It is important to underline that, respect the traditional methods adopted to realize micro-devices, the $3D$ printing based techniques offer several advantages, among which the simplicity of the design and the possibility to quickly and inexpensively print complex microfluidic channels, by using low-cost equipment.

Thanks to this advantages, the micro-optofluidic chips realized by using the two methods proposed could represent an important step ahead in the realization of devices with an higher level of functional complexity.

Chapter 6

Micro-optofluidic slug flow detector

6.1 Working principle and design

The micro-optofluidic slug flow detector was designed to be a compact device that integrate the optic components and the fluidic part. In Figure 6.1 a cartoon of the working principle: assuming that two fluids with quite different indexes flow in a microfluidic channel and an incident laser beam interferes with them in a test section, it is possible to obtain a different light transmission based on which fluid is interfering with the laser beam at the moment. The choice of the material to realize the chip and the optic parts, as well as, the choice of fluids for the slug flow played a fundamental role. The polymer selected to realize the whole device and the waveguide was the PDMS. To do this, it is important to surround the waveguide with a material whose refractive index is lower than the one of the PDMS ($n_{PDMS} = 1.41$). In this way, then, it is possible to cover the whole system with PDMS layers.

Based on the working principle on which the waveguide are based, as said in 5.2, the air is one of the material selected to have the total internal reflection; but its require an holder system to keep in place the waveguide and this involves having a device that is not unique but composed by different pieces.

Among the materials with refractive index lower than the one of the PDMS, the

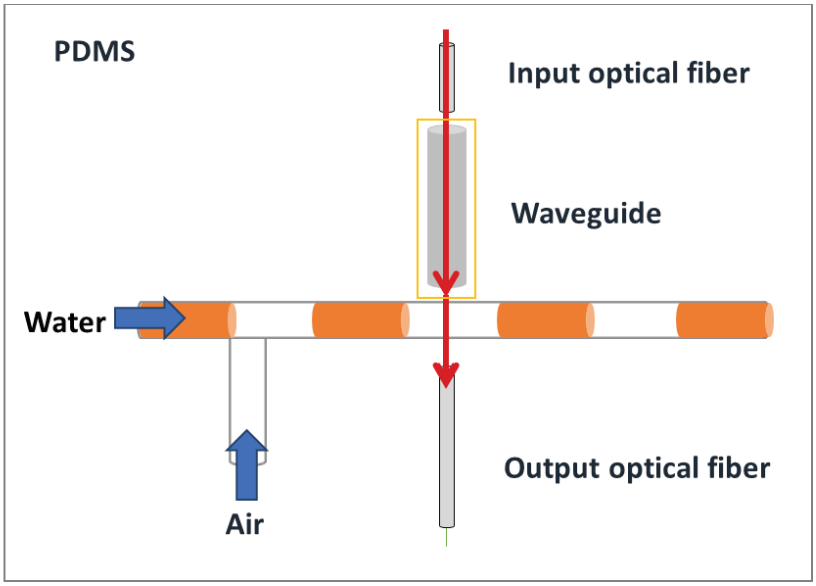

Fig. 6.1. Working principle of slug flow detector.

copper and the gold were selected ($n_{Cu} = 1.1$, $n_{Au} = 0.47$). In Figure 6.2, a schematic representation of waveguide covering, respectively, with PDMS, air, copper and gold.

The device computer design (CAD) of the detector consist in a micro-channel, two sections for the optical fiber insertions and an allocation for the waveguide (see Figure 6.3(a)). The micro-channel has a squared section of 400 μm side, the diameter of the inlets and outlet wells is 2.4 mm. The T-junction is at distance of 13 mm from the inlets. Some constraints must be taken into account in the design of the slug detector:

- the smallest dimension of the PDMS waveguide is 1 mm;
- the distance between waveguide and micro-channel it is such as to guarantee a safety closure for the micro-channel with liquid in pressure ($d_1 = \ 1mm$, $d_2 = \ 0.5\ mm$);
- the detection must be of the same order of the microchannel, so the output optical fiber has a diameter of 400 μm.

The details about the CAD are reported in Figure 6.3(b).

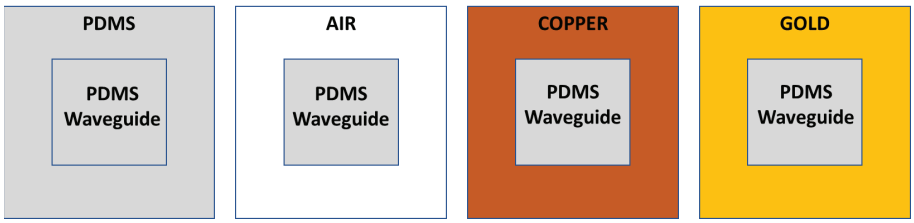

Fig. 6.2. Schematic representation of waveguide covering, respectively, with PDMS, air, copper and gold.

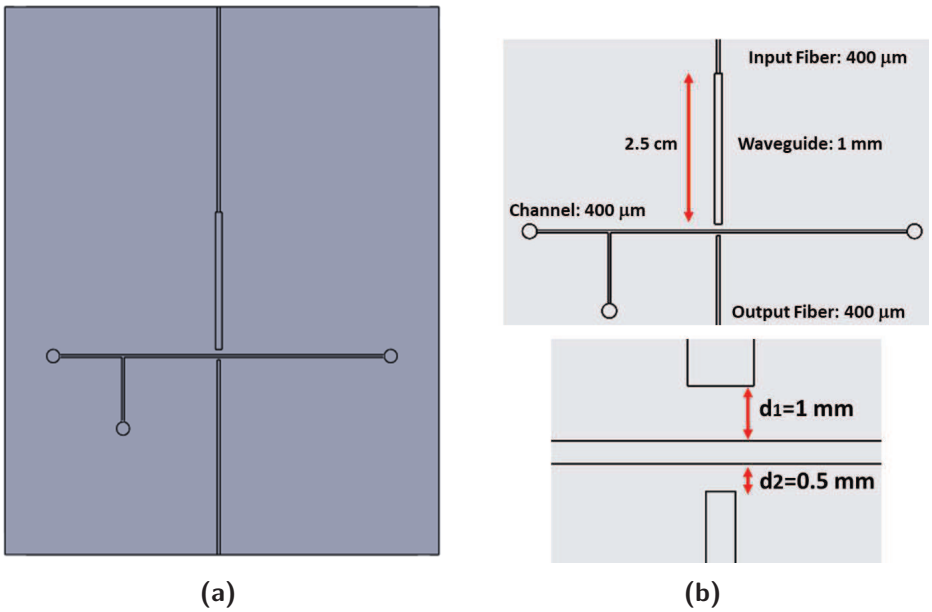

Fig. 6.3. (a) Device computer design (CAD) of the detector: a micro-channel, two sections for the optical fiber insertions and an allocation for the waveguide; (b) Details about the CAD measures and constrains.

6.2 Micro-optical components optimization

The performance were evaluated by the ray-tracing simulation (TracePro). Both for the waveguide and for the flow detector, the simulation involves the use of an input optical fiber, that emits simulated laser light of 10 mW (100 rays) and an output fiber, whose surface was selected as plane to collect the transmitted light.

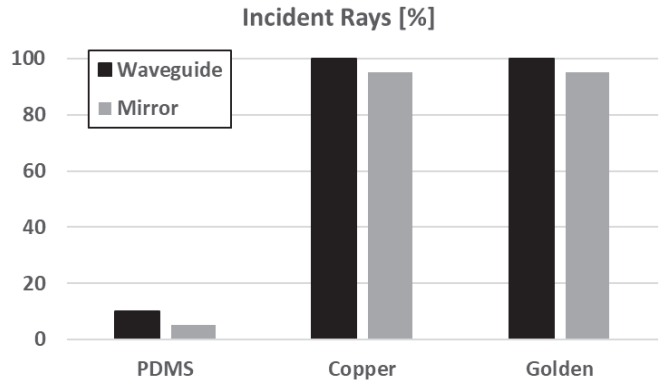

Fig. 6.4. Incident rays in percentage that reach the output fiber for waveguide and mirror.

It is worth to notice in the histogram in Figure 6.4 that, in the PDMS covering the most rays are dispersed (10% on output fiber), instead the total number of emitted rays reach the output fiber (100%) in the case of copper and gold covering for the waveguide. In the mirror simulation, the trend of the incident rays in the histogram is the same seen for the waveguide but the total amount of rays that reach the output fibers decreases, in particular [5, 95, 95]% respectively for PDMS, copper and gold.
From the results shown, can be observed that covering the components is a performing solution for the light's transmission, therefore on the output surface is read a considerable value of incident rays to permit to find a possible experimental implementation.

6.2.1 Realization approaches and optical characterization

The first step of the device realization process is the optimization of the holder for the micro-optical components by using the copper and gold. The attention was focused on the waveguide support realization.
To obtain a copper covering, two different methods are tested: by using a computer numerical control (CNC) to make a cut (Figure 6.5(a)); obtain the channel for imprint using a purpose master (Figure 6.5(b)). The second approach has different advantages respect the first one, cutting material by means of CNC pro-

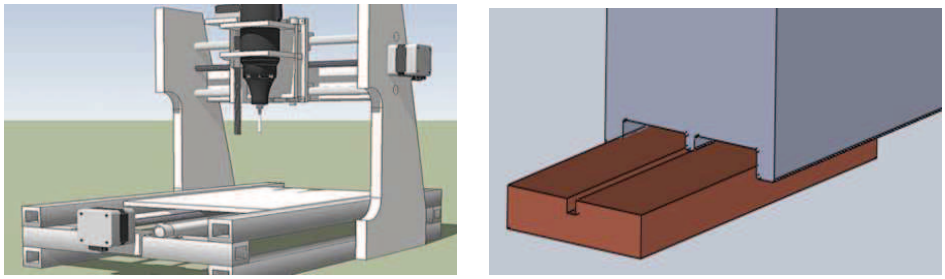

(a) (b)

Fig. 6.5. Copper holder realization: (a) by using CNC machine; (b) by imprinting technology.

(a) (b)

Fig. 6.6. Golden covering realization: (a) manual sputter coater machine; (b) a picture of machine used.

duces unavoidably micro scraps into the channel that can be fastidious when the waveguide in PDMS is disposed in the copper channel. Thus, using the imprinting method is applied a lower and more controllable stress. This has been obtained realizing a master in stainless steel and using a press in the channel (copper strip). To perform the gold covering is used a special machine (manual sputter coater machine) that is able to depose a tiny layer of gold in order of nanometres on the device (Figure 6.6). This is a simple-to-use basic instrument for gold coating of SEM specimens. It has fully variable current control, a digital process timer with pause option, a variable height specimen table, a hinged top plate and an o-ring sealed vacuum chamber. The control allows the sputter current to be set independently of the gas pressure, which is adjusted separately by a manual leak valve. Coverage and grain size are optimised for any specimen. The cool magnetron

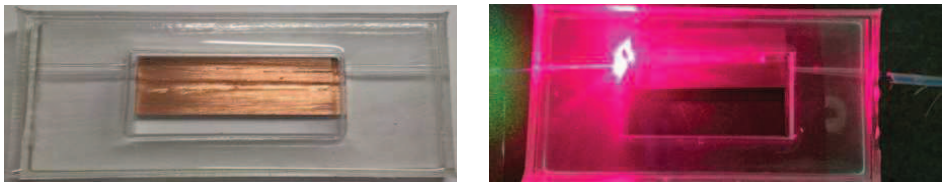

(a) (b)

Fig. 6.7. Cooper holder characterization: (a) waveguide in the copper support; (b) light propagation.

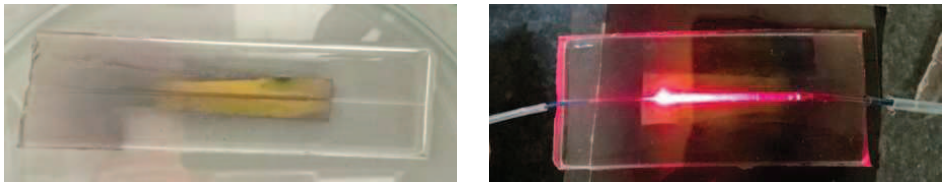

(a) (b)

Fig. 6.8. Golden covering characterization: (a) waveguide with golden covering; (b) light propagation.

type head with 57 mm diameter target gives efficient sputtering with minimal heating. Coating time is set by a timer with a digital readout and stored in the memory. The vacuum status and the sputter current are displayed on the panel meter.

A modular desktop design combines sputter control unit, pumping system and thickness monitor into an area of only $400x600$ mm. It is fully integrated using a quick release all-metal coupling system. The adjustable height specimen table will accept up to 12 pin type stubs or can be used as a platform for other types of stubs and specimens. A vacuum feed through is provided for the optional film thickness monitor. The golden process was applied to two PDMS layers with an allocation of dimensions suitable to accommodate the waveguide. These two layers were, then, reversely bounded after inserting the waveguide inside.

In both cases, the PDMS waveguides were realized following the protocol described in Section 5.4; for the copper holder, the waveguide was placed on the groove created for the allocation and, in the second case the waveguide was inserted in the golden PDMS layers.

The waveguides realized with the two methods were tested by using the same experimental setup described in Section 5.5. In Figure 6.7 is reported the test

on waveguide using copper support. This technique in testing phase shows good results. The photodiode connected to the output fiber read a signal of 5.5 V. Unlikely, copper has different disadvantages as the corrosion in time, that alters the chemical's property as the refractive index value. Test of a waveguide using golden covering is reported in Figure 6.8. The experimental results show excellent performance for the golden covering: 10.7 V read in output, the same value in the case of entire fiber connected between the light source and the photodiode. This method is easier to implement respect to the copper holder and the device is obtained involved less components; in fact, using only the PDMS and pass it through the golden coater machine, it is possible to obtain the final device. For this reason, the golden covering was selected to realize the slug flow detector.

6.3 Slug flows detector realization

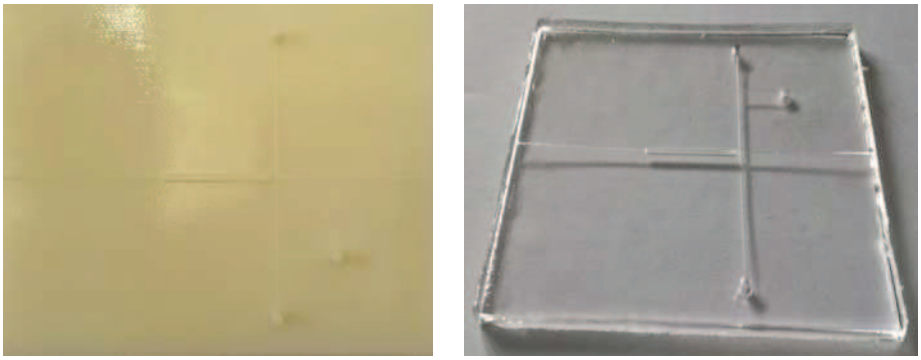

(a) **(b)**

Fig. 6.9. Slug flow detector (a) Master in 3D Printing; (b) PDMS device.

Starting from the design of the CAD, the master was produced by using the 3D printing machine and applying the protocol described in section 5.1 the PDMS device (see Figure 6.9(a)-(b)) and the PDMS waveguide were realized. The allocation for the waveguide was covered by golden layer (using the manual sputter coater machine) and then, was placed inside the waveguide. The device was closed with a thin PDMS bulk, obtained with a concentration of 5:1 of curing agent (see Figure 6.10(a)-(b)).

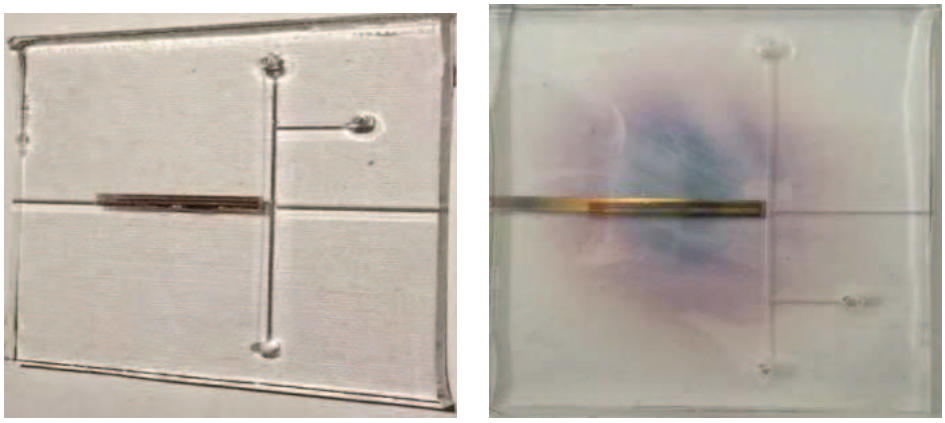

(a) (b)

Fig. 6.10. Slug flow detector (a) device with a thin golden covering; (b) final device with waveguide.

6.4 Flow detector characterization

6.4.1 Simulation performance

Taking into account the flow detector cartoon several simulations were made considering six configurations, four of these do not take into account the process but only the optical components $\{C1, C2, C3, C4\}$ and other two configurations were used to characterize the process $\{C5, C6\}$, they are described as follows (see Fig. 6.11):

- conditions $C1$ and $C2$: the laser light coupled with the optical fiber (with core of 365 μm, SMA to free end) was aligned at a distance of 100 μm with a second optical fiber (with core of 910 μm in $C1$ and of 365 μm in $C2$, SMA to free end) coupled with the acquisition system;
- condition $C3$: the optical fiber (with core of 910 μm, SMA to free end) was aligned at a distance of 100 μm with a second optical fiber (with core of 365 μm, SMA to free end);
- condition $C4$: is the same of $C2$, in which the two optical fibers were aligned at a distance of 2 mm, to simulate the real distance in the device;

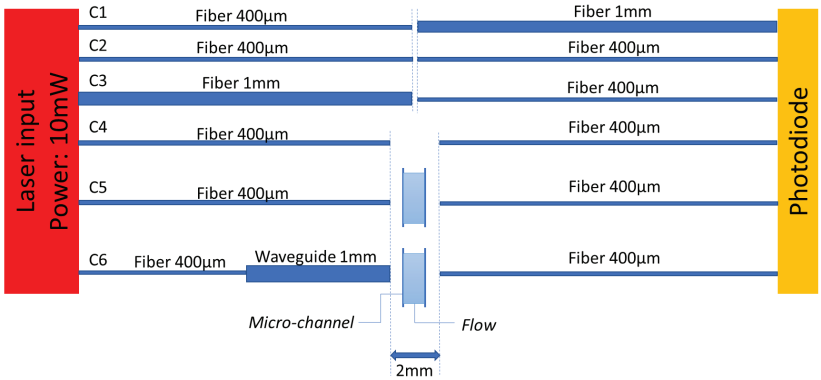

Fig. 6.11. Different configurations analysed by using a simulated laser light of 10 mW that emits 100 rays.

Tab. 6.1. Simulation results in terms of incident rays (%), transmitted power (mW) and losses (%).

	Incident rays (%)	**Power (mW)**	**Losses (%)**
(C1)	100	10	0
(C2)	74	7.399	26
(C3)	16	1.599	84
(C4)	34	3.381	66

- condition $C5$: the microchannel (of 1 mm) was inserted in the space between the two optical fibers and filled with different fluids;
- condition $C6$: the gilding waveguide was aligned to the input optical fiber. This configuration represents the condition of the real flow detector realized.

In the condition $C1$, the percentage of incident rays on the examined surface is maximum (100 %) and the power is equal to the transmitted one (10 mW), since the irradiation light cone is completely collected by the detector. In $C2$, the relative radiation map shows a percentage of incident rays of 74 % and also the condition $C2$ is interested by a significant amount of losses, in fact only the 16 % of rays reach the examined surface. This effect is due to the fact that the diameter of the transmission fiber is equal to or greater than that of the receiving fiber, which therefore can detect only a part of the light beams emitted.
In $C4$ the losses increase in fact the percentage of detected rays is 34 %. In table 6.1 the percentage of incident rays, the power in (mW) and the losses (%) are

Tab. 6.2. Simulation results in terms of incident rays (%), transmitted power (mW) and losses (%) in absence and presence of gold waveguide.

	Rays (%)		**Power (mW)**		**Losses (%)**	
	(C5)	**(C6)**	**(C5)**	**(C6)**	**(C5)**	**(C6)**
Air	38	40	3.358	3.507	66.4	64.9
Water	49	43	4.482	3.926	55.2	60.7
PBS	49	43	4.482	3.926	55.2	60.7
Hexadecane	50	43	4.541	3.904	54.6	61.0

represented.

In $C5$ and $C6$ simulations, different fluids were considered: air, water, phosphate-buffered saline (abbreviated as PBS) and hexadecane, whose refractive indexes are respectively, $n_{air} = 1$, $n_{water} = 1.33$, $n_{PBS} = 1.34$ and $n_{hex} = 1.434$. The table 6.2 summarized the results in terms of percentage of incident rays, the power in (mW) and the losses (%), respectively in the absence and presence of gold waveguide.

In both simulations, the rays that crossing the air flux lose more energy than in the case of water, PBS and hexadecane flows. The interpretation of the radiation maps of the condition $C6$ (Figure 6.12) shows a percentage of detected rays very similar for all the fluids under examination: 40% of rays transmitted by air against 43% transmitted by water, PBS, Hexadecane.

In Figure 6.13, an histogram for the comparison in terms of percentage of losses, in $C5$ and $C6$. A slight deterioration in performance can be observed in the waveguide configuration. As it is possible to see from the histogram, by the simulations it is not possible to perceive a differentiation between the water, PBS and hexadecane fluids, whose percentages of loss are approximately equivalent (around 61%).

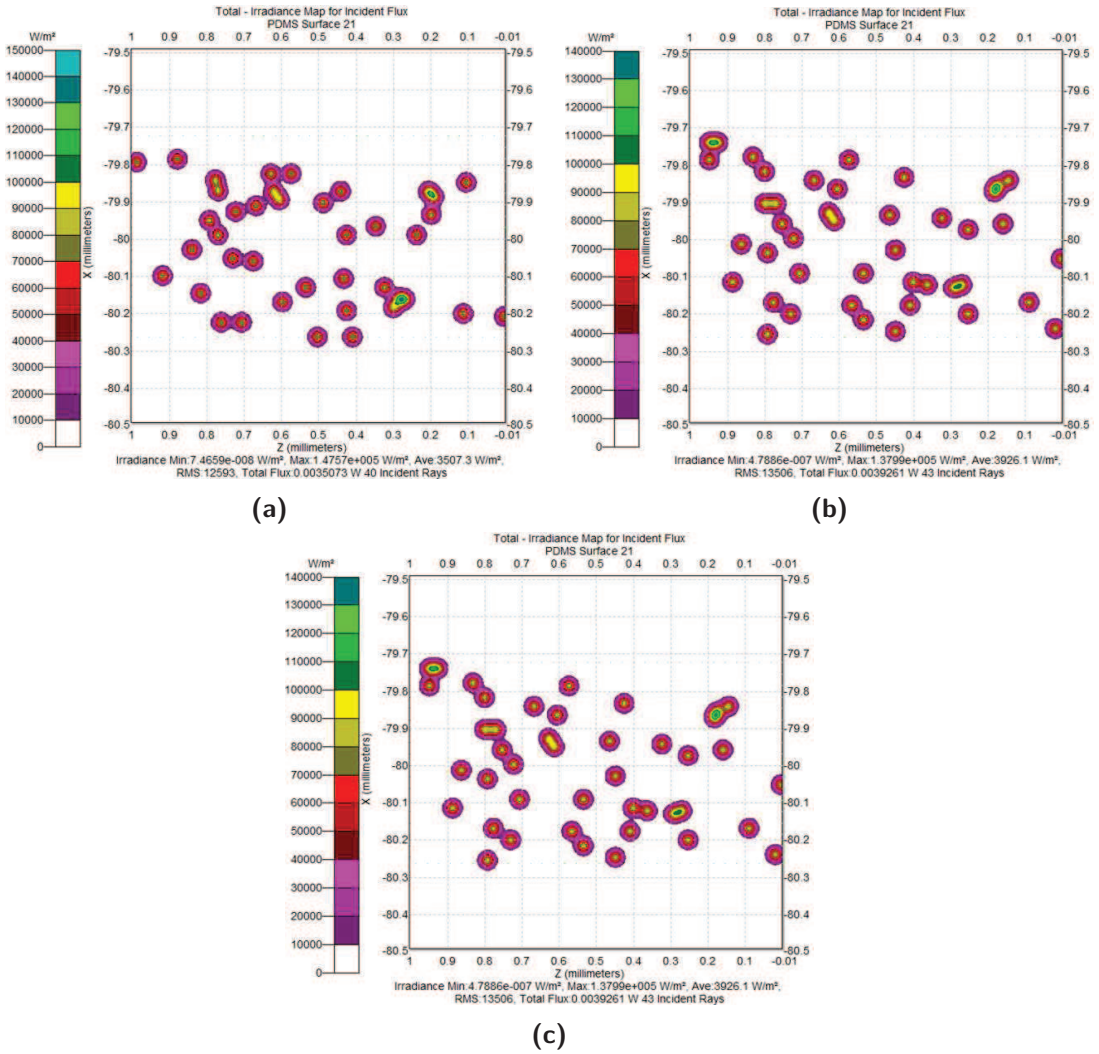

Fig. 6.12. Radiance maps of condition $C6$ with golden covering waveguide (a) air flux; (b) water or PBS flux and; (c) hexadecane flux.

6.4.2 Experimental performance

In order to study the dynamic behavior of the micro-optofluidic device for the characterization of two-phase flows, the setup in Figure 6.14(a) was considered. In Figure 6.14(b) a picture of the device connected to the inlet and outlet tubes and to two optical fibers. A pair of syringe pumps (neNESYS by Cetoni Gmbh) was used to generate a controlled flow into micro-channel. Two multi-mode optical fibers

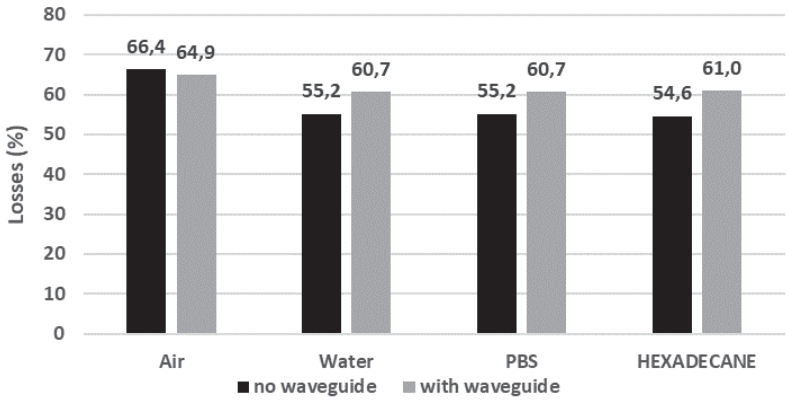

Fig. 6.13. Histogram for the comparison in terms of percentage of losses, without and with waveguide.

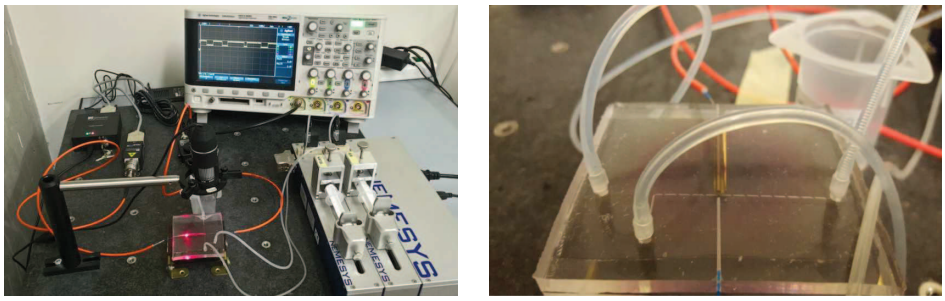

(a) **(b)**

Fig. 6.14. (a) Global experimental setup for the device characterization; (b) The picture of the device connected to the inlet and outlet tubes and to two optical fibers.

with $N.A. = 0.22$ were used (SMA to free end by Thorlabs) with a core diameter of 400 μm. The free end of the optical fibers was clamped onto the device's input fiber insertion while the SMA-end was connected to the laser source (Rgb NovaPro Laser 660-125) with a wavelength of 660 nm. For a visual inspection of the process, a digital USB microscope with direct illumination was placed above the device.
For the three different types of fluid (water, PBS and hexadecane) coupled with air in order to realize three different two-phase flows, various tests were performed by implementing different flow rates and different laser powers.
For the data acquisition the gain of the photodiode (PDA 100A, Thorlabs) was set to 50dB and an oscilloscope (Agilent MSO7054A) with sampling frequency of 500 Hz was used for the signal acquisition.

Tab. 6.3. Experiments and the tests conducted to study the dynamic behavior of the micro-optofluidic device.

	Power (mW)	V_{air} **(ml/min)**	$V_{water/PBS/hexadecane}$ **(ml/min)**
test-1	1 - 5 - 10	0.1	0.2
test-2	1 - 5 - 10	0.15	0.3
test-3	1 - 5- 10	0.2	0.4

By the experimental investigation, the dynamic characterization was conducted studying:

- the amplitude ranges of the electrical signal at the output, depending on the fluids that interfere with the laser;
- the relationship between the flow velocity of the pumped fluids at the inlet of the T junction and the frequency of the two-phase flow generated.

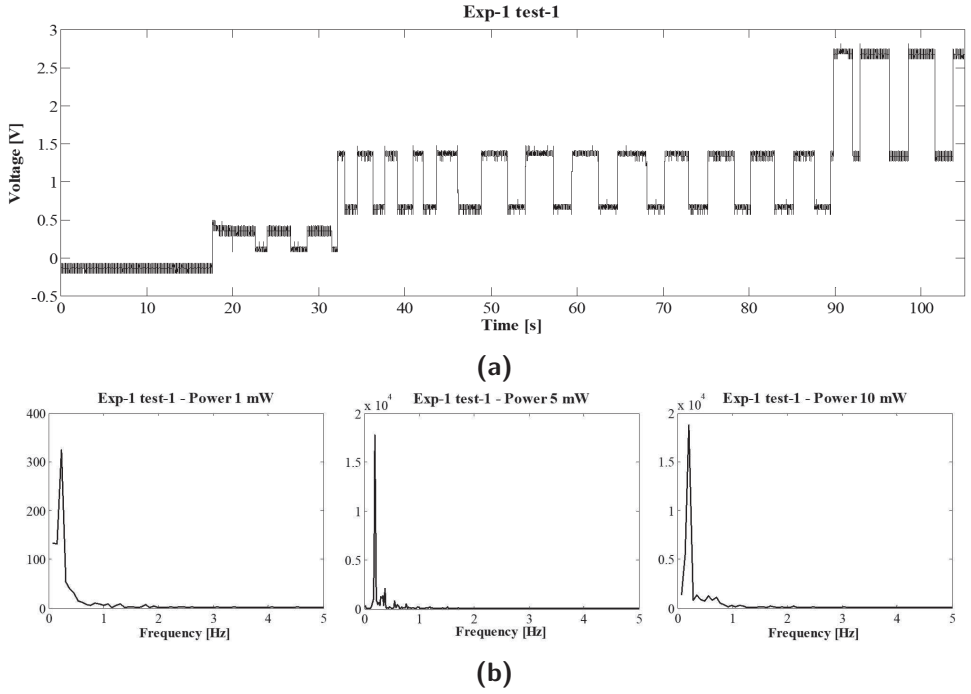

Fig. 6.15. Exp-1 (air-water): test-1 ($V_{air} = 0.1\ ml/min$ and $V_{water} = 0.2\ ml/min$); (a) signal in time; (b) spectra for power $\in \{1, 5, 10\}\ mW$.

In Table 6.3 are summarized the experiments and the tests conducted. The two-phase flows were generated by pumping air and a liquid (water, PBS and hexadecane). The experiments labelled as $Exp-1$ is related to air and water flux, the $Exp-2$ is for air and PBS and in $Exp-3$ the liquid selected was the hexadecane. For each of these experiments, three tests were performed changing the flow rates and considering the flow rate of liquids twice the one of the air. In $test-1$: $V_{air} = 0.1\ ml/min$ and $V_{water/PBS/hex} = 0.2\ ml/min$, in $test-2$: $V_{air} = 0.15\ ml/min$ and $V_{water/PBS/hex} = 0.3\ ml/min$ and $test-3$: $V_{air} = 0.2\ ml/min$ and $V_{water/PBS/hex} = 0.4\ ml/min$. For the hexadecane the $test-3$ was not completed due to problems of chemical incompatibility between hexadecane oil and the material of which the inlet is made. Moreover, in order to detect the dominant frequency, the acquired signals have been appropriately processed to produce the relevant spectral analysis. In Figure 6.15(a) - Figure 6.17(a), the signals detected in the $Exp-1$, respectively, for $test-1$, $test-2$ and $test-3$. It is possible to see an increment of voltage level in the correspondence of power changes. In Figure 6.18 and Figure 6.19 are reported the signals for $test-1$ - $test-3$ ($Exp-2$), and only for $test-1$ and $test-2$ ($Exp-3$).

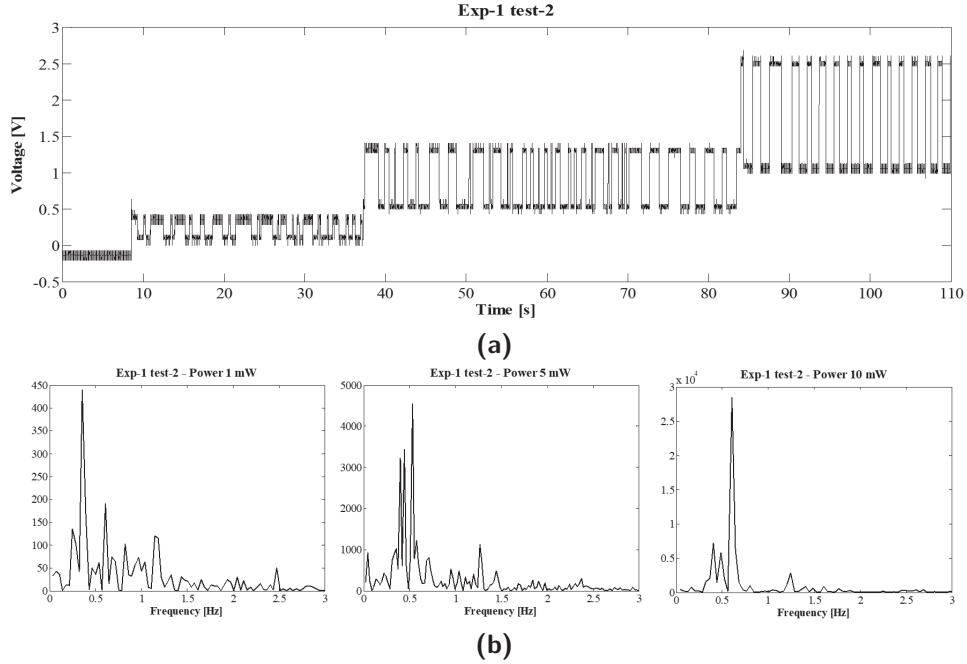

Fig. 6.16. Exp-1 (air-water): test-2 ($V_{air} = 0.15\ ml/min$ and $V_{water} = 0.3\ ml/min$) (a) signal in time; (b) spectra for power $\in \{1, 5, 10\}\ mW$.

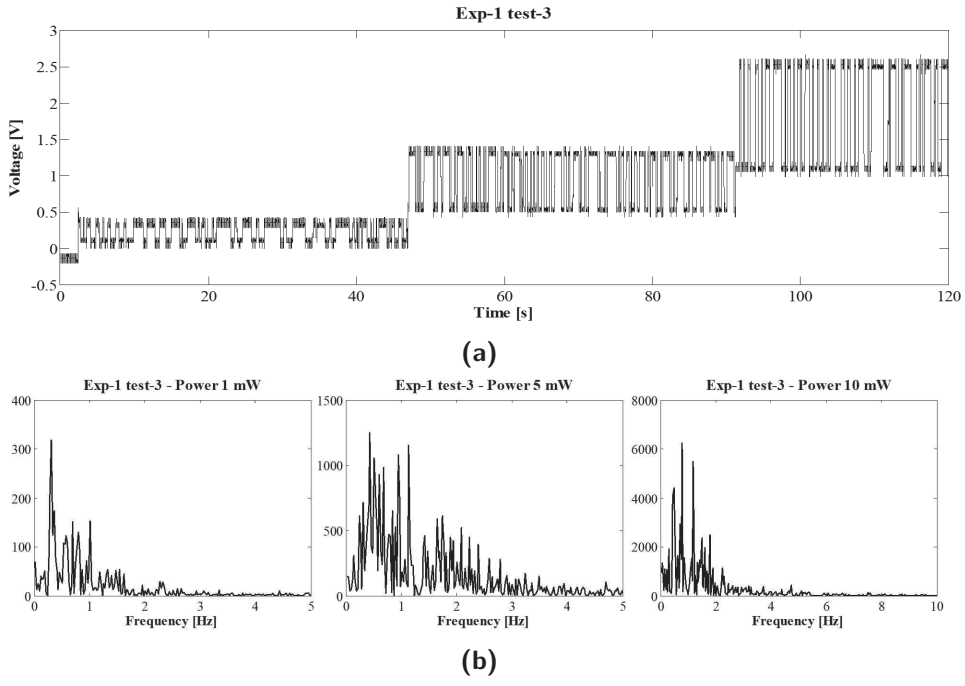

Fig. 6.17. Exp-1 (air-water): test-3 ($V_{air} = 0.2\ ml/min$ and $V_{water} = 0.4\ ml/min$) (a) signal in time; (b) spectra analysis for power $\in \{1, 5, 10\}\ mW$.

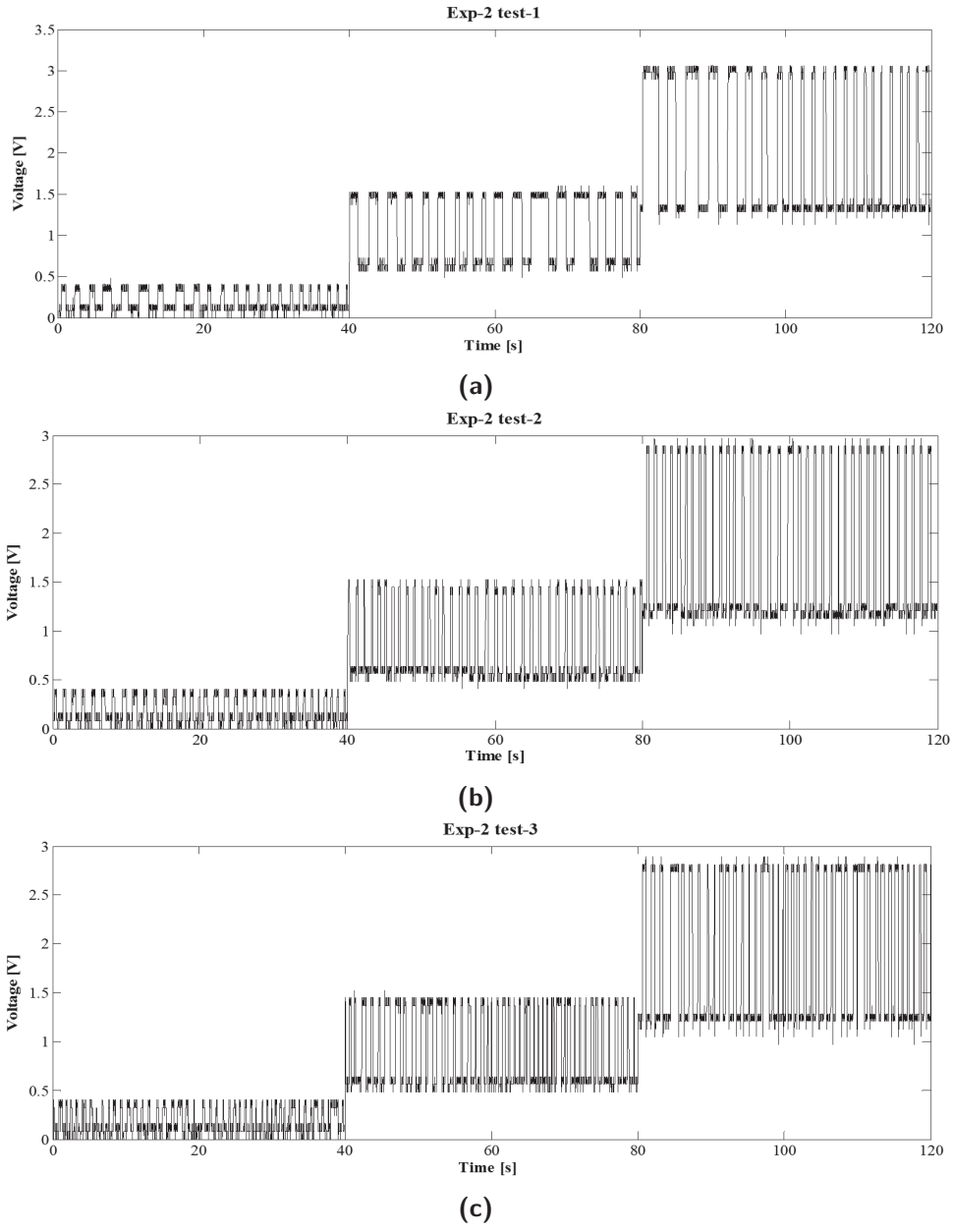

Fig. 6.18. Exp-2 (air-PBS): signal in time for (a) $test-1$ ($V_{air}=0.1\ ml/min$ and $V_{PBS}=0.2\ ml/min$); (b) $test-2$ ($V_{air}=0.15\ ml/min$ and $V_{PBS}=0.3\ ml/min$); (c) $test-3$ ($V_{air}=0.2\ ml/min$ and $V_{PBS}=0.4\ ml/min$).

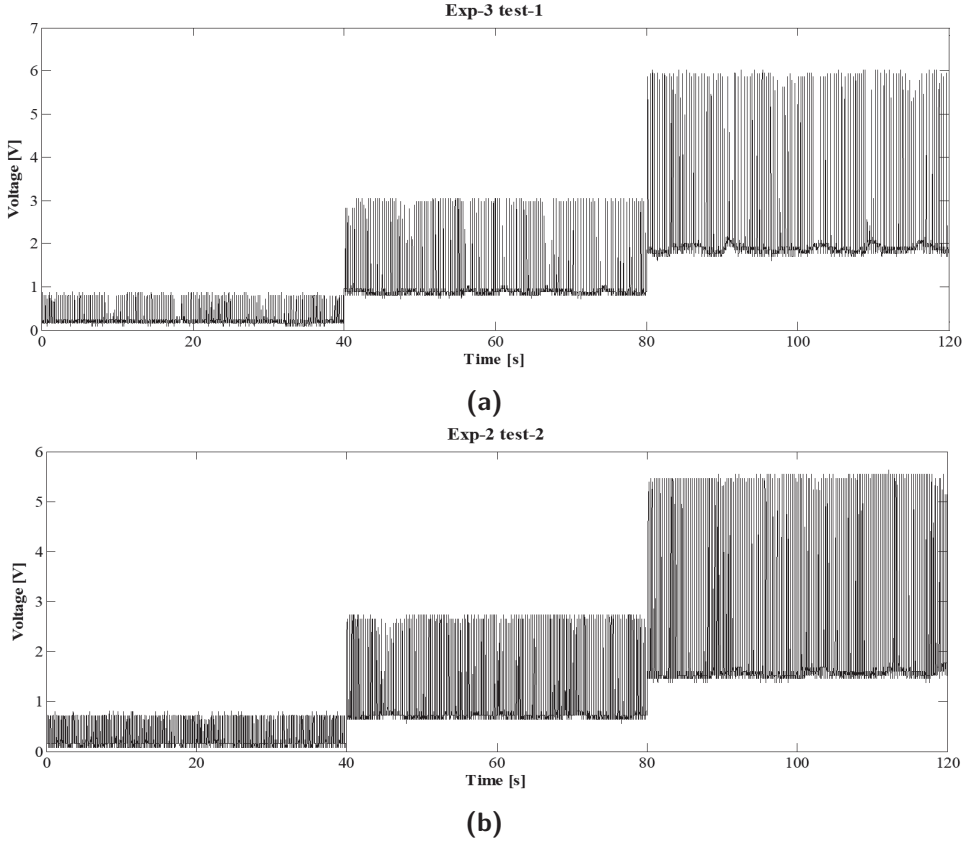

Fig. 6.19. Exp-3 (air-hexadecane): signal in time for (a) $test-1$ ($V_{air} = 0.1\ ml/min$ and $V_{hex} = 0.2\ ml/min$); (b) $test-2$ ($V_{air} = 0.15\ ml/min$ and $V_{hex} = 0.3\ ml/min$)

For each signals related to a specific power level, the spectra were computed and the frequency peaks detected. In Figure 6.15(b) - Figure 6.17(b), for $Exp-1$ as an example, are reported the three spectra analysis for power $\in \{1, 5, 10\}\ mW$. The histogram (Figure 6.20(a)) shows the frequency peaks for each test, in $Exp-1$. Except for $test-1$ in which the trend of frequency peaks detected is constant when the power changes, in the other cases the frequency increases as the flow rate and the power increase. A quite similar trend is shown for $Exp-2$ (Figure 6.20(b)), but in this case for $test-3$ the frequency values are constant. It is possible to notice an opposite behaviour of $Exp-3$, in which the frequency decreases as the flow rate and the power increase.

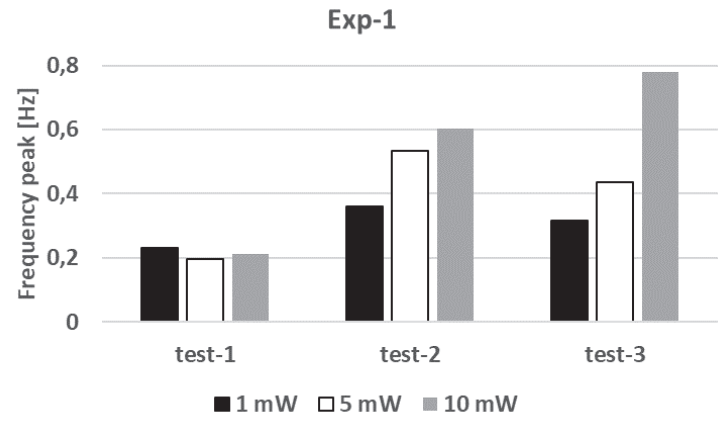

(a)

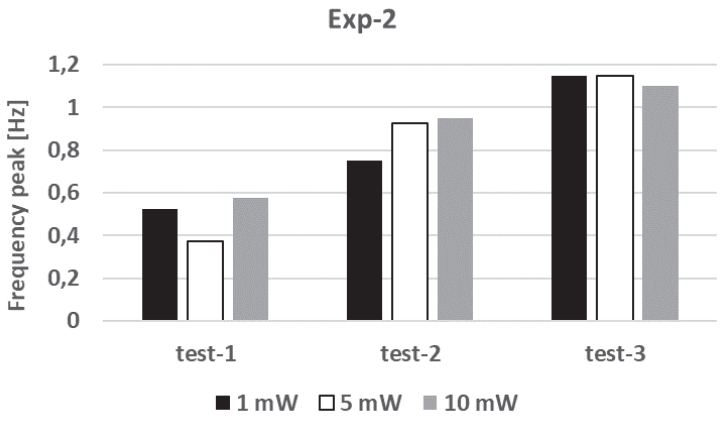

(b)

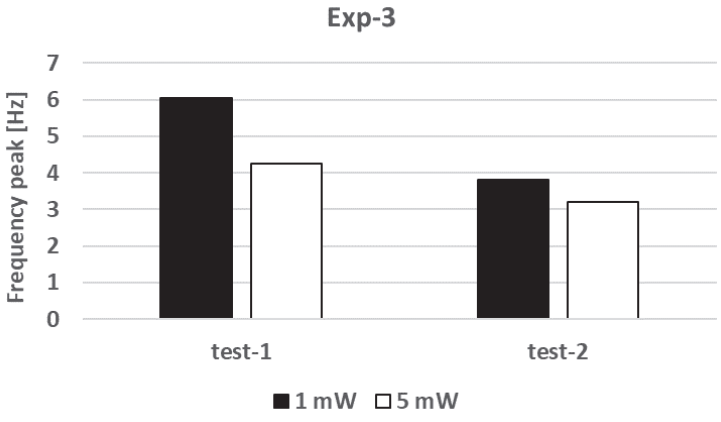

(c)

Fig. 6.20. Histograms of frequency peaks for each test and for each level of power.

This is possibly due to the fact that the laser heats up the haxadecane slug surface increasing laser power and slows down the slugs despite the increased of flow rate; this phenomenon is only visible in the case of hexadecane because it is a more stable liquid than water and PBS.
By a comparison of the results obtained from the analysis of the acquired data, it is possible to notice the different transmission of the fluids used, proven by the different values of the signal amplitude, for each of the three laser power values $\in \{1, 5, 10\}\ mW$. The dynamic characterization is shown in Figure 6.21 (a)-(c), where the different tests and fluids intercepted by the laser are distinguished.
Starting from lower values in the case of air, higher values are observed for PBS, water and hexadecane.
It is possible to compute the voltage ranges as the difference between the voltage level of liquid (water, PBS, hexadecane) and that of air. The Figure 6.22 shows the voltage ranges in the case of air-water, air-PBS and air-hexadecane fluxes, taking into account only the $test - 1$ ($V_{air} = 0.1\ ml/min$ and $V_{water/PBS/hexadecane} = 0.2\ ml/min$). As already seen from the signals acquired by the photodiode, the range for the air-hexadecane is bigger than the others and as the laser power increases, an amplification of the fluid differentiation range is observed.
The most important aspect, however, concerns the dynamic characterization of the device, that is the observation of different voltage ranges of the signals acquired at the passage of the three different fluids, for each of the three laser powers used. From the figures shown it is possible to distinguish different behaviours for air, water, PBS or hexadecane, both in terms of amplitude range of the output signal, and in terms of frequency response of two-phase flows. The micro-optofluidic detector implemented is therefore able to identify the type of fluid flowing in the microchannel.
Finally, a comparative evaluation between the simulations and the experimental data was done.

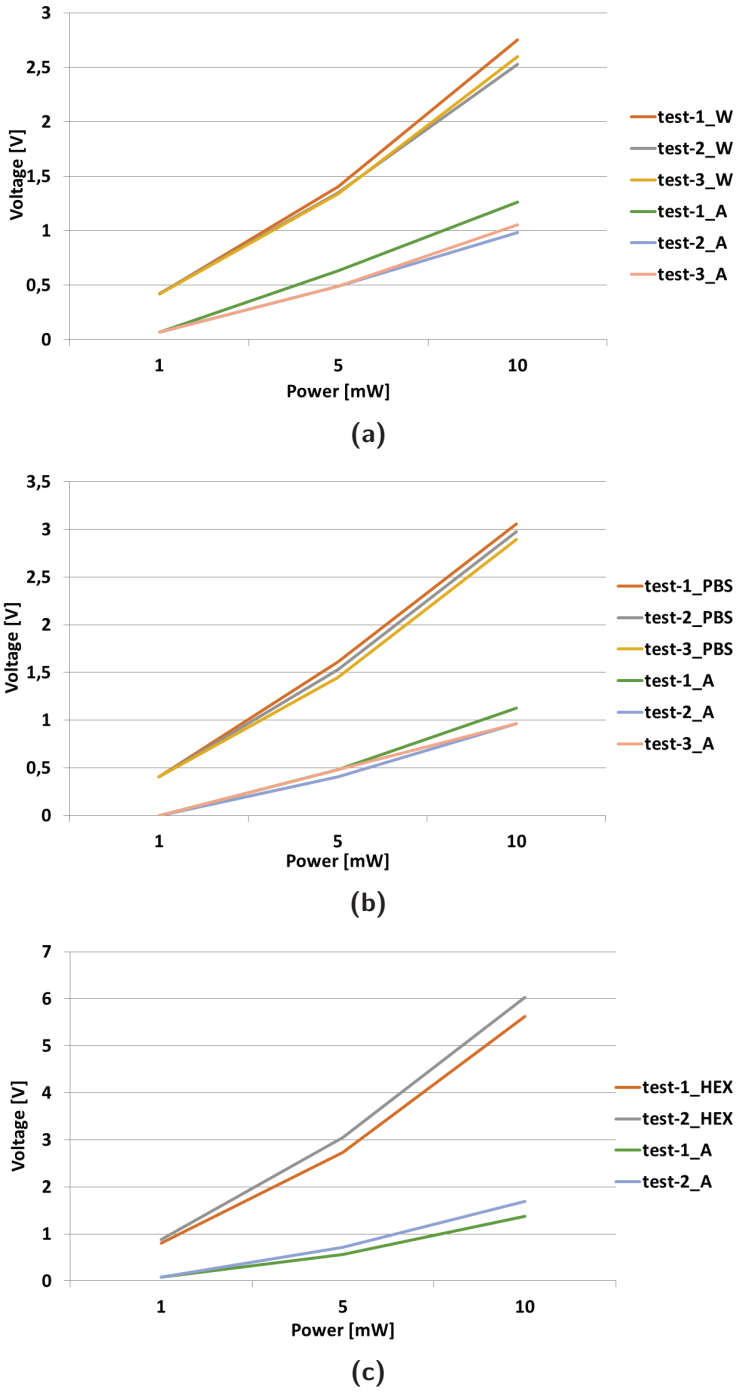

Fig. 6.21. Dynamic characterization of (a) air-water flux ($Exp-1$); (b) air-PBS flux ($Exp-2$) and; (c) air-hexadecane flux ($Exp-3$).

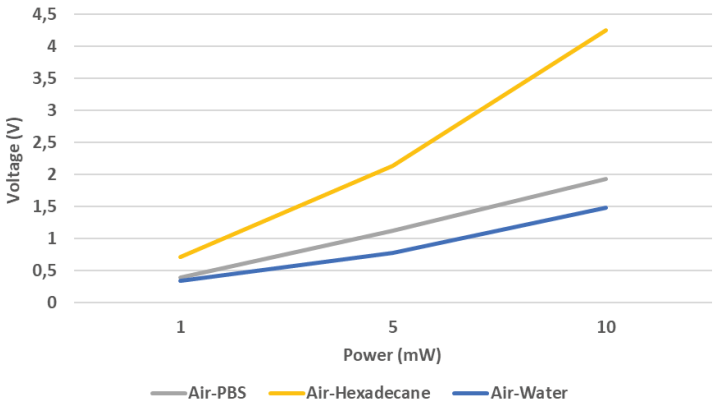

Fig. 6.22. Comparison of amplitude levels of the signals acquired in the $tests - 1$ ($V_{air} = 0.1\ ml/min$ and $V_{water/PBS/hex} = 0.2\ ml/min$).

Tab. 6.4. Transmitted power (mW) and losses (%) for simulation, and transmitted signal (V) and relative losses (%) for the experimentation.

	Simulation		**Experimentation**	
	Power (mW)	**Losses (%)**	**Voltage (V)**	**Losses (%)**
(1)	10.0	0	7.1	0
(2)	7.40	26.01	6.6	7.0
(6)-air	3.51	64.93	1.4	80.28
(6)-water	3.93	60.74	2.7	61.97
(6)-PBS	3.93	60.74	3.0	57.75
(6)-hex	3.90	60.96	5.5	22.54

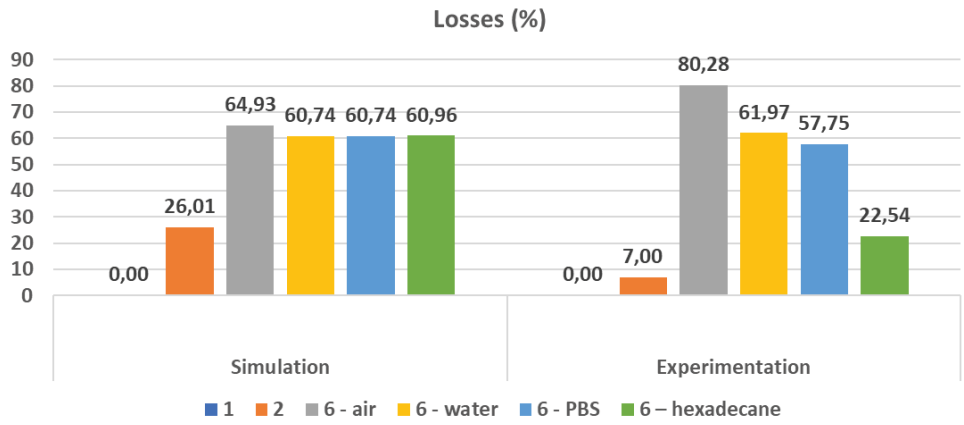

Fig. 6.23. Histogram of percentages of losses for configuration (1), (2) and (6) with the different fluids considered (air, water, PBS and hexadecane).

In Table 6.4 are shown the results in terms of transmitted power (mW) and losses (%) in simulation, instead in the experimental case the data are in volts (V). To make a performance comparison between simulation and experimentation, it is then decided to work with the percentage of losses of the signal for configuration (1), (2) and (6) with the different fluids considered (air, water, PBS and hexadecane).

In Figure 6.23 the histogram of percentages of losses that occur with the various fluids used. It is possible to notice a variability in the experimentation respect to the simulation results, in which the losses are almost constant for the fluids. That mean more instability in the experimental context, due to the changes of properties of the fluids that interact with the power laser, difficult aspect to take in consideration during the simulations. It is important to highlight that, the losses are greater in the case of air and less for the hexadecane, in particular the losses decrease as the refractive index of the fluid increase. So, it is possible to use this device as a slug flow detector analyzing the different transmitted signals.

Conclusions

Microfluidics has become a powerful technique for a wide variety of applications in biotechnology, engineering, physics, and chemistry. By studying processes in channels with typical dimensions of tens to hundreds micrometers, it is possible to control the flux process, for example the reactions while economizing on the consumption of reagents.
In this work the slug-flow have been used to investigate methodologies and technologies that can be easily integrated in a general approach for the real-time control of microfluidc processes on-chip. To do that a methodological path starting from the extraction of parameters for the flows characterization, to their use for the flows modelling and the control schemes development has been discussed and enriched by a wide experimentation.

Aspects investigate have been addressed to develop protocols and design of micro-opto-fluidics systems by using the 3D printing technology. Particularly the prototypes of PDMS micro-optical components (waveguide and mirror) and of a slug flow detector have been shown, underling their performance in the classification of fluids inside micro-channnel dynamically in different operative conditions.

In Chapter 1, an experimental study on the slug flow patterns in micro-channels of $\{320; 640\}$ μm width, where a continuous slug flow was generated by two upstream of water and air, is presented. The attention was focused on three issues: the difference in the slug displacement in straight channel compared with serpentine, the role played by the input flow rates in the slugs flow patterns classification and the flow changes in different channel positions. The photodiode signals acquired were analyze and organized in three experimental sets based on the investigated aspects. A classification of the obtained slugs dynamic in slow and fast flow

patterns was established, in slow patterns the long air intervals are combined with short water intervals (or vice versa), while in fast patterns both intervals are small and similar. The dependence of transition point between the two slugs regimes on the channel geometry and input flow rate was evinced. Technologically, the processes classification obtained by a simple analysis of optical signals, instead of using costly and bulky equipment or invasive process detection systems represents a proof of concept for the integration of both the detection and flow control in a single micro-system.

In Chapter 2, a class of models was defined to identify the displacement of the slugs in microfluidic channel in unknown experimental conditions. The experimental time series acquired from the microfluidic process was assumed as a generic state variable of an unknown master system and this information was used to drive the Chua's slave system, with a known model and undefined parameters. By the genetic algorithm optimization procedure was searched the set of parameters of the Chua's model that can guarantee the two systems synchronization, leading to the time series identification. This result highlights the possibility with a single model to identify a variety of flow regimes generated in two-phase microfluidic processes, independently of how the processes have been generated, no directed relations with the input flow rate used are in the model.

The data-driven modelling was discussed in Chapter 3 to identify the dynamics of fast two-phase flows in microchannels. Two classes of NARX models implemented by neural networks and wavelet networks were investigated. The identification process was applied to the single experiment (*Single-Pattern*) and collecting up to seven experiments together (*Multi-Pattern*). The performance of the identified models were evaluated both in time and in frequency domain by the introduction of parameters for the flow velocity characterization. For the identification of the slug flows velocity, assumed as the mean of the slugs inter-distance, both NN and WN models show satisfactory performance. This result is confirmed in the case of *Single-Pattern* and *Multi-Pattern*, opening to the use of the model also in the case of varying input flow rates. The models used led to the successful identification of the slugs tracking and to quantify the slug's velocity being corre-

lated with the mean of the slug inter-distance.

In Chapter 4, real-time platform for the control of the slugs flow in microchannel was described. A wide experimental campaign was conducted to extract from the optical signals the control parameter, the slug frequency, associated with different flow conditions. By using this parameter, the open loop and closed loop control law was defined and implemented in Labview platform. In particular, the closed loop control strategy allows to have a continuous and stable maintenance of the desired flow conditions, simply by imposing the desired slug frequency. Starting from this result, in the future works, the attention could be focused on the implementation of a more detailed control strategy in order to manage a wide range of dynamics. Moreover, taking into account the complexity of the processes in addition to the linear controller implemented, an integral action could also be considered for the optimal tuning and therefore to reduce the frequency error increasing the performance of the control.

A PDMS $3D$ printing technique for producing waveguides, mirrors and slug flow detector is presented in Chapters 5 and 6. In micro-optofluidic devices, it is important to deliver, as closer as possible, the input light to the fluidic process and then, to collect the output signal, but also to steer the direction of the light beam. To do this, a method is proposed to realize waveguides and mirrors that can be integrated in the devices. Firstly, the components were individually tested to evaluate and compared the simulation and experimental performances. A protocol was established to realize the micro-optofluidic slug flow detector, that integrate the optic components and the fluidic part.
Considering two fluids with quite different indexes flowing in a microfluidic channel and an incident laser beam that interferes with them in a test section, it is possible to obtain a different light transmission based on which fluid is interfering with the laser beam at the moment. The choice of the material to realize the chip and the optic parts, as well as, the choice of fluids for the slug flow played a fundamental role. The polymer selected to realize the whole device and the waveguide was the PDMS, it is important to surround the waveguide with a material whose refractive index is lower than the one of the PDMS. The proposed technique consists in

gilding of the allocation in which then the waveguide is deposed. The slug flow detector was tested considering three different flows: air-water, air-PBS and air-hexadecane. The results highlight that the losses are greater in the case of air and less for the hexadecane, in particular the losses decrease as the refractive index of the fluid increase. So, it is possible to use this device as a slug flow detector analyzing the different transmitted signals.
From the point of view of production technology, the future developments might involve the integration of mirror in the device to steer the direction of the light path and from the microfluidic point of view, in future works the slug flow can be replaced with a two-phase flow, in which a phase is constituted by cells (for example red blood cells).

List of Figures

List of Tables

Bibliography

[1] G. M. Whitesides, "The origins and the future of microfluidics," *Nature*, vol. 442, pp. 368–373, 2006.

[2] D. T. Chiu, A. J. deMello, D. D. Carlo, P. S. Doyle, C. Hansen, R. M. Maceiczyk, and R. C. R. Woottom, "Small but perfectly formed? successes, challenges and opportunities for microfluidics in the chemical and biological sciences," *Chem*, vol. 2, pp. 201–223, 2017.

[3] A. Schober, C. Augspurger, U. Fernekorn, K.-F. Weibezahn, G. Schlingloff, M. Gebinoga, M. Worgull, M. Schneider, C. Hildmann, F. Weise, J. Hampl, L. Silveira, I. Cimalla, and B. LÃ$\frac{1}{4}$bbers, "Microfluidics and biosensors as tools for nanobiosystems research with applications in the "life science"," *Materials Science and Engineering B*, vol. 169, pp. 174–181, 2010.

[4] K. F. Jensen, B. J. Reizman, and S. G. Newman, "Tools for chemical synthesis in microsystems," *Lab on a Chip*, vol. 14, pp. 3206–3212, 2014.

[5] S. Mashaghi, A. Abbaspourrad, D. A. Weitz, and A. M. van Oijen, "Droplet microfluidics: A tool for biology, chemistry and nanotechnology," *Trends in Analytical Chemistry*, vol. 82, pp. 118–125, 2016.

[6] A. Serizawa, Z. Feng, and K. Kawara, "Two-phase flows in microchannels," *Experimental Thermal and Fluid Science*, vol. 26, pp. 703–714, 2002.

[7] L. G. Bleris, P. D. Vouzis, J. G. Garcia, M. G. Arnold, and M. V. Kothare, "Pathways for optimization-based drug delivery," *Control Engineering Practice*, vol. 15, pp. 1280–1291, 2007.

[8] Y. C. Chung, B. J. Wen, and Y. C. Lin, "Optimal fuzzy sliding-mode control for bio-microfluidic manipulation," *Control Engineering Practice*, vol. 15, pp. 1093–1105, 2007.

[9] J. Maddala and R. Rengaswamy, "Droplet digital signal generation in microfluidic networks using model predictive control," *Journal of Process Control*, vol. 23, pp. 132–139, 2013.

[10] L. G. Bleris, J. Garcia, M. V. Kothare, and M. G. Arnold, "Towards embedded model predictive control for system-on-a-chip applications," *Journal of Process Control*, vol. 16, pp. 255–264, 2006.

[11] L. Stern, A. Bakal, M. Tzur, M. Veinguer, N. Mazurski, N. Cohen, and U. Levy, "Doppler-based flow rate sensing in microfluidic channels," *Sensors*, vol. 14, p. 19799, 2014.

[12] F. Yeshaiahu, L. P. Lee, D. Psaltis, and C. Yang, *Optofluidics Fundamentals, Devices, and Application*. McGraw-Hill, 2010.

[13] M. Brammer and T. Mappes, "Modular platforms for optofluidic systems," *Optofluidics*, pp. 1–10, 2010.

[14] V. V. Steijn, M. T. Kreutzer, and C. R. Kleijn, "Piv study of the formation of the segmented flow in microfluidic t-junction," *Chemical Engineering Science*, vol. 62, p. 7505, 2007.

[15] F. Schembri and M. Bucolo, "Periodic input flow tuning nonlinear two-phase dynamics," *Microfluidics and Nanofluidics*, vol. 11, p. 189, 2011.

[16] F. Doyle, L. Jovanovic, D. Seborg, R. S. Parker, B. W. Bequette, A. M. Jeffrey, X. Xia, I. K. Craig, and T. McAvoy, "Tutorial on biomedical process control," *Journal of Process Control*, vol. 17, pp. 571–594, 2007.

[17] A. Tabeling, *Introduction to microfluidics*. Oxford University Press, 2005.

[18] J. D. Tice, H. Song, A. D. Lyon, and R. F. Ismagilov, "Formation of droplets and mixing in multiphase microfluidics at low values of the reynolds and capillary numbers," *Langmuir*, vol. 19, pp. 9127–9133, 2003.

[19] M. R. Bringer, C. J. Gerdts, H. Song, J. D. Tice, and R. F. Ismagilov, "Microfluidic systems for chemical kinetics that rely on chaotic mixing in droplets," *Philos. Trans. Roy. Soc.*, vol. 362, pp. 1087–1104, 2004.

[20] P. Sudarsan and V. M. Ugaz, "Fluid mixing in planar spiral microchannels," *Lab Chip*, vol. 6, pp. 74–82, 2005.

[21] G. Ribatski, L. Wojtan, and J. Thome, "An analysis of experimental data and prediction methods for two-phase frictional pressure drop and flow boiling heat transfer in micro-scale channels," *Exp. Therm. Fluid Sci.*, vol. 31, pp. 1–19, 2006.

[22] G. Gregory and D. Scott, "Correlation of liquid slug velocity and frequency in horizontal cocurrent gas-liquid slug flow," *AIChE J.*, vol. 15, pp. 933–935, 1969.

[23] Y. Taitel and A. E. Dukler, "A model for predicting flow regime horizontal and near horizontal gas-liquid flow," *AIChE J.*, vol. 22(1), pp. 47–55, 1976.

[24] U. Kadri, "A probabilistic approach for predicting average slug frequency in horizontal gas/liquid pipe flow," *Oil Gas Sci. Technol. Rev. IFP Energies Nouvelles*, vol. 69(2), pp. 331–339, 2014.

[25] K. A. Triplett, S. M. Ghiaasiaam, S. I. Abdel-Khalik, and D. L. Sadowski, "Gas liquid two-phase flow in microchannels. part i: Two-phase flow patterns," *Int. J. Multiph. Flow*, vol. 25, pp. 377–394, 1999.

[26] K. A. Triplett, S. M. Ghiaasiaam, S. I. Abdel-Khalik, A. LeMoule, and B. N. McCord, "Gas liquid two-phase flow in microchannels. part ii: Void fraction and pressure drop," *Int. J. Multiph. Flow*, vol. 25, pp. 395–410, 1999.

[27] R. Revellin, V. Dupont, T. Ursenbacher, J. R. Thome, and I. Zun, "Characterization of diabatic two-phase flows in microchannels: flow parameter results for r-134a in a 0.5 mm channel," *Int. J. Multiph. Flow*, vol. 32, pp. 755–774, 2006.

[28] S. Waelchli and P. R. V. Rohor, "Two-phase flow characteristics in gas-liquid microreactors," *Int. J. Multiph. Flow*, vol. 32, pp. 791–806, 2006.

[29] H. M. Letzel, J. Shouten, R. Krishna, and C. van de Bleek, "Characterization of regimes and regime transition in bubble columns by chaos analysis of pressure signals," *Chem. Eng. Sci.*, vol. 52, pp. 4447–4459, 1997.

[30] H. Ding, Z. Y. Huang, Z. H. Song, and Y. Yan, "Hilbert-huang transform based signal analysis for the characterization of gas-liquid two-phase flow," *Flow Meas. Instrum.*, vol. 18(1), pp. 37–46, 2007.

[31] S. Wang, R. Mosdorf, and M. Shoji, "Nonlinear analysis on fluctuation feature of two-phase flow through a t-junction," *Heat Mass Transf.*, vol. 46, pp. 1519–1528, 2003.

[32] V. V. Steijn, M. T. Kreutzer, and C. R. Kleijn, "Velocity fluctuations and segmented flow in microchannels," *Chem. Eng. J.*, vol. 135, pp. S159–S165, 2008.

[33] W. Hong and F. Teng, "The flow pattern and differential pressure fluctuations of transition flow across tube bundles," *Energy Procedia Part B*, vol. 17, pp. 1507–1512, 2012.

[34] F. Trachsel, A. Gunther, S. Khan, and K. Jensen, "Measurement of residence time distribution in microfluidic systems," *Chem. Eng. Sci.*, vol. 60, pp. 5729–5737, 2005.

[35] B. Kuswandi, J. Nuriman, W. Huskens, and W. Verboom, "Optical sensing systems for microfluidic devices: a review," *Anal. Chim. Acta*, vol. 601 (2), pp. 141–155, 2007.

[36] F. Sapuppo, F. Schembri, L. Fortuna, A. Llobera, and M. Bucolo, "A polymeric microoptical system for the spatial monitoring in two-phase microfluidics," *Microfluid. Nanofluid.*, vol. 12 (165), p. 174, 2012.

[37] T. Kraus, A. Gunther, N. de Mas, M. Schmidt, and K. Jensen, "An integrated multiphase flow sensor for microchannels," *Exp. Fluids*, vol. 36, pp. 819–832, 2004.

[38] F. Sapuppo, A. Llobera, F. Schembri, M. Intaglietta, V. Cadarso, and M. Bucolo, "A polymeric micro-optical interface for flow monitoring in biomicrofluidics," *Biomicrofluidics*, vol. 4 (1), pp. 1–13, 2010.

[39] M. Worner, "Numerical modeling of multiphase flows in microfluidics and micro process engineering: a review of methods and applications," *Microfluid. Nanofluidics*, vol. 12, pp. 841–886, 2012.

[40] C. W. Zobel and D. F. Cook, "Evaluation of neural network variable influence measures for process control," *Engineering Applications of Artificial Intelligence*, vol. 24, pp. 803–812, 2011.

[41] A. Pikovsky, M. Rosenblum, and J. Kurths, *Synchronization: A Universal Concept in Nonlinear Sciences*. Cambridge University Press.

[42] L. Ljung, *System Identification-Theory for User*. 2nd edition, Upper Saddle River, N. J. Prentice-Hall, PTR, 1999.

[43] S. A. Billings and H. L. Wei, "A new class of wavelet networks for nonlinear system identification," *IEEE Transactions on neural network*, vol. 16(4), 2005.

[44] Q. Zhang, "Using wavelet network in nonparametric estimation," *IEEE Transactions on Neural Networks*, vol. 8(2), 1997.

[45] R. Caponetto, L. Fortuna, G. Manganaro, and M. Xibilia, "Chaotic system identification via genetic algorithm," *Genetic Algorithms in Eng. Systems*, vol. 414, pp. 170–174, 1995.

[46] R. N. Madan, *Chua's Circuit: A paradigm for Chaos*. World Scientific Series on Nonlinear Science, SERIE B vol. 1.

[47] D. E. Golbert, *Genetic Algorithms in Search, Optimization and Machine Learning*. Addison Wesley.

[48] F. Schembri, F. Sapuppo, and M. Bucolo, "Experimental classification of nonlinear dynamics in microfluidic bubbles' flow," *Nonlinear Dynamics*, vol. 67, pp. 2807–2819, 2012.

[49] M. A. Unger, H. P. Chou, T. Thorsen, A. Scherer, and S. R. Quake, "Monolithic microfabricated valves and pumps by multilayer soft lithography," *Science*, vol. 288, pp. 113–116, 2000.

[50] J. Fahrenberg, W. Bier, D. Maas, W. Menz, R. Ruprecht, and W. Schomburg, "A microvalve system fabricated by thermoplastic molding," *J. Micromech. Microeng*, vol. 5, pp. 169–171, 1995.

[51] K. Hosokawa, T. Fuji, and I. Endo, "Handling of picoliter liquid samples in a poly(dimethylsiloxane)-based microfluidic device," *Anal. Chem.*, vol. 71(20), pp. 4781–4785, 1999.

[52] K. M. Grant, J. W. Hemmert, and H. White, "Magnetic fieldcontrolled microfluidic transport," *J. Am. Chem. Soc.*, vol. 124, pp. 462–467, 2002.

[53] T. Cubaud and C.-M. Ho, "Transport of bubbles in square microchannels," *Physics of Fluids*, vol. 16(12), p. 4575, 2004.

[54] M. Worner, "Numerical modeling of multiphase flows in microfluidics and micro process engineering: a review of methods and applications," *Microfluidics and Nanofluidics*, vol. 12, pp. 841–886, 2012.

[55] H. Bruus, *Theoretical Microfluidics*. Oxford University Press, New York, 2008.

[56] M. Bucolo, L. Fortuna, and F. Sapuppo, "An innovative opto-sensing workbench for bio-microfluidics monitoring and control," *Proceedings of the 29th Int. IEEE Conf. EMBS*, pp. 6314–6317, 2007.

[57] D. Appleyard, K. Vandermeulen, H. Lee, and M. Lang, "Optical trapping for undergraduates," *Am. J. Phys.*, vol. 75, pp. 5–14, 2007.

[58] T. Duncombe and A. Tentori, "Microfluidics: reframing biological enquiry," *Nat. Rev. Mol. Cell Biol.*, vol. 16, pp. 554–567, 2007.

[59] D. D. Carlo, "Inertial microfluidics," *Lab Chip*, vol. 9.

[60] T. O. Haver, "A pragmatic introduction to signal processing with applications in chemical analysis."

[61] H. Kantz and T. Schreiber, *Nonlinear Time Series Analysis*. Cambridge University Press, 2004.

[62] S. Boccaletti, J. Kurths, G. Osipov, D. Vallardes, and C. Zhou, "The synchronization of chaotic systems," *Phys. Rep*, vol. 366, pp. 1–101, 2002.

[63] N. Boccara, *Modeling Complex Systems*. Springer-Verlag, 2004.

[64] M. G. Rosenblum, A. S. Pikovsky, and J. Kurths, "From phase to lag synchronization in coupled chaotic oscillators," *Phys. Rev. Lett.*, vol. 78, pp. 4193–4196, 1997.

[65] J. R. Dormand and P. J. Prince, "A family of embedded runge-kutta formulae," *Journal of Computational and Applied Mathematics*, vol. 6, 1980.

[66] L. Ljung, Q. Zhang, P. Lindskong, A. Iouditski, and R. Singh, "An integrated system identification toolbox for linear and nonlinear models," *Proc 14th IFAC Symposium on System Identification*, 2007.

[67] H. Becker and L. E. Locascio, "Polymer microfluidics devices," *Talanta*, vol. 56, p. 267, 2002.

[68] J. C. McDonald and G. M. Whitesides, "Poly(dimethylsiloxane) as a material for fabricating microfluidic devices," *Accounts of Chemical Research*, vol. 35(7), p. 491, 2002.

[69] J. M. Ng, I. Gitlin, A. D. Stroock, and G. M. Whitesides, "Components for integrated poly (dimethylsiloxane) microfluidic systems," *Electrophoresis*, vol. 23, p. 3461, 2007.

[70] D. A. Chang-Yen, R. K. Eich, and B. K. Gale, "A monolithic pdms waveguide system fabricated using soft-lithography techniques," *J. Lightwave Technol.*, vol. 23, p. 2088, 2005.

[71] A. Llobera, R. Wilke, and S. Buttgenbach, "Enhancement of the response of poly(dimethylsiloxane) hollow prisms through air mirrors for absorbance-based sensing," *Talanta*, vol. 75, p. 473, 2008.

[72] S. Camou, H. Fujita, and T. Fujii, "Pdms 2d optical lens integrated with microfluidic channels: principle and characterization," *Lab Chip*, vol. 3, p. 40, 2003.

[73] H. N. Chan, M. J. A. Tan, and H. Wu, "Point-of-care testing: applications of 3d printing," *Lab Chip*, vol. 17, p. 2713, 2017.

[74] Y. Hwang, O. H. Paydar, and R. N. Candler, "3d printed molds for non-planar pdms microfluidic channels," *Sensors and Actuators A*, vol. 226, p. 137, 2015.

[75] N. P. Macdonald, J. M. Cabot, P. Smejkal, R. M. Guijt, B. Paull, and M. C. Breadmore, "Comparing microfluidic perfomance of three-dimensional (3d) printing platform," *Anal. Chem.*, vol. 89, p. 3858, 2017.

[76] J. M. Maia, V. A. Amorim, D. Alexandre, and P. V. S. Marques, "Real-time optical monitoring of etching reaction of microfluidic channel fabricated by femtosecond laser direct writing," *Journal of Lightwave Technology*, vol. 35(11), p. 2291, 2017.

[77] N. Rossetto and C. Ferrante, "A microfluidic optical beam steerer," *Microfluid Nanofluid*, vol. 16, pp. 47–53, 2014.

[78] E. Weber, F. Keplinger, and M. J. Vellekoop, "Detection of dissolved lactose employing an optofluidic micro-system," *Diagnostics*, vol. 2, pp. 97–106, 2012.

[79] M. I. Lapsley, S. S. Lin, X. Mao, and T. J. Huang, "An in-plane, variable optical attenuator using a fluid-based tunable reflective interface," *Applied Physics*, vol. 95, p. 083507, 2009.

[80] F. Cairone, S. Gagliano, D. C. Carbone, G. Recca, and M. Bucolo, "Micro-optofluidic switch realized by 3d printing technology," *Microfluidics and nanofluidics*, vol. 20, pp. 61 – 71, 2015.

[81] M. Raffel, C. E. Willert, S. Wereley, and J. Kompenhans, *Particle image velocimetry: A practical guide.* Springer, 1998.

[82] C. Poelma, A. Kloosterman, B. P. Hierck, and J. Westerweel, "Accurate blood flow measurements: Are artificial tracers necessary?" *PLoS ONE 2*, vol. 7(9), p. e45247, 2012.

[83] W. Thielicke and E. J. Stamhuis, "Towards user-friendly, affordable and accurate digital particle image velocimetry in matlab," *Journal of Open Research Software*, vol. 2, p. e30, 2014.

[84] http://www.jpiv.vennemann online.de/.